CrystEngComm

Accepted Manuscript

This article can be cited before page numbers have been issued, to do this please use: S. L. Tan and E. R. T. Tiekink, *CrystEngComm*, 2021, DOI: 10.1039/D0CE01810D.

ROYAL SOCIETY OF CHEMISTRY

rsc.li/crystengcomm

View Article Online
DOI: 10.1039/D0CE01810D

Non-covalent interactions involving remote substituents influence the topologies of supramolecular chains featuring hydroxyl-O–H···O(hydroxyl) hydrogen bonding in crystals of $(HOCH_2CH_2)_2NC(=S)N(H)(C_6H_4Y\text{-}4)$ for Y = H, Me, Cl and NO_2

Sang Loon Tan and Edward R. T. Tiekink*

Research Centre for Crystalline Materials, School of Science and Technology, Sunway University, 47500 Bandar Sunway, Selangor Darul Ehsan, Malaysia

E-mail: edwardt@sunway.edu.my

ORCID iD: 0000-0002-5343-3382 (SLT); 0000-0003-1401-1520 (ERTT)

Abstract

Crystallography shows the universal adoption of supramolecular chains featuring by hydroxyl-O–H···O(hydroxyl) hydrogen bonding in crystals of $(HOCH_2CH_2)_2NC(=S)N(H)(C_6H_4Y\text{-}4)$ for Y = H, Me, Cl and NO_2. However, distinct topologies, *i.e.* linear (Y = H), helical (Y = Me and Cl) and zig-zag (Y = NO_2) are noted with major differences in the pitch of the polymer. Geometry-optimisation, MEP and NPA analyses shows a distinct electronic structure for the Y = NO_2 derivative, in particular relating to the activation of the aryl rings. An exhaustive analysis of the molecular packing (point-to-point interactions, crystal structure similarity, Hirshfeld surface analysis, NCI and QTAIM, interaction energies and energy frameworks) point to the importance

View Article Online
DOI: 10.1039/D0CE01810D

of C–H···π(aryl) interactions in stabilising the chains but these have a considerably reduced influence in the crystal with Y = NO_2, where π(aryl)···π(aryl) interactions are important. The more open arrangement for the linear chain in **1** facilitates the formation of C–H···π(aryl) interactions and the more compact arrangements enable the formation of stabilising, intra-chain methylene-C–H···S(thione) interactions. This study highlights the role of second-tier non-covalent interactions exert upon the arrangement of conventional hydrogen bonding interactions.

Footnote

† Electronic supplementary information (ESI) available: Crystallographic data, electrostatic potential charge deviations, NPA charges, HOMO-LUMO plots, PXRD patterns, molecular packing diagram, NCI and QTAIM plots. CCDC 2047050-2047053 contain the supplementary crystallographic data for this paper. For ESI and crystallographic data in CIF or other electronic format see DOI: 10.1039/d0cexxxxxx

View Article Online
DOI: 10.1039/D0CE01810D

Introduction

In the organic solid-state, conventional hydrogen bonding plays a privileged role in arranging molecules into supramolecular assemblies,[1-4] often by design employing the supramolecular synthon approach.[5] This prominent role notwithstanding, other intermolecular contacts come to the fore when conventional hydrogen bonding does not occur in three dimensions or is not present at all. Here, a myriad of alternative interactions come to the fore, such as π···π, C–H···π, lone-pair···π, chalcogen bonding, halogen bonding, *etc*.[6] Along with hydrogen bonding, many of these interactions provide similar energies of stabilisation in their crystals and being inherently weak are therefore, flexible, being subject to moderation by chemical substitution, steric effects, *etc*. The delineation of the role of these different modes of association is highly desirable in order to rationalise more fully the assembly of molecules in crystals as even small changes in molecular packing can influence macroscopic properties relating to, *e.g*. optoelectronic properties,[7] drug discovery[8] and the conformation of molecules.[9] Further, the control of flexible, cooperative supporting intermolecular interactions will lead to the strategic design of higher dimensional aggregation patterns in crystals featuring persistent, structure-directing hydrogen bonding patterns operating in zero-, one- or two-dimensions.

These aforementioned considerations increasingly motivate systematic studies of crystals featuring (i) a common hydrogen bonding aggregation pattern despite the presence of different substituents,[10-14] (ii) multiple hydrogen bonding options and their adoption related to small chemical changes[15-23] and (iii) no conventional hydrogen bonding present with studies conducted in order to ascertain the influence of other non-covalent interactions upon molecular aggregation.[24-27] Herein, an investigation related to scenario (i) is presented. As anticipated from the formula of the molecules investigated herein, *i.e*. $(HOCH_2CH_2)_2NC(=S)N(H)(C_6H_4Y\text{-}4)$ for Y

View Article Online
DOI: 10.1039/D0CE01810D

= H (**1**), Me (**2**), Cl (**3**) and NO_2 (**4**), Fig. 1, hydrogen bonding is prominent and a consistent adoption of supramolecular chains in the respective crystals is apparent, in each case mediated by hydroxyl-O–H···O(hydroxyl) interactions. However, the chains display distinct topologies, *i.e.* linear (**1**), helical (**2** and **3**) and zig-zag (**4**), and of the series, only **2** and **3** are isostructural.

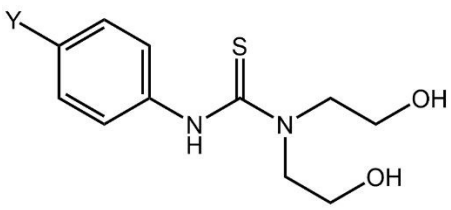

Y = H (**1**), Me (**2**), Cl (**3**) and NO_2 (**4**)

Fig. 1 Chemical diagrams for the $(HOCH_2CH_2)_2NC(=S)N(H)(C_6H_4Y\text{-}4)$ molecules investigated herein.

Compounds **1**-**4** are examples of tri-substituted derivatives of thiourea, a well-known class of compound.[28] While crystal structures are known for derivatives conforming to the general formula $(HOCH_2CH_2)N(R)C(=S)N(H)R$,[29-31] for R = alkyl, aryl, none are known for the di-hydroxyethyl analogues, *i.e.* $(HOCH_2CH_2)_2NC(=S)N(H)R$. Indeed, with the exception of **1**,[32] which was investigated recently for anti-leishmanial activity, compounds **2**-**4** do not appear to have been reported previously. Herein, the synthesis, spectroscopic and crystallographic characterisation of **1**-**4** are described along with a detailed analysis of the molecular packing in their crystals with the aim of ascertaining the role of the Y = H, Me, Cl and NO_2 substituents upon the supramolecular association.

View Article Online
DOI: 10.1039/D0CE01810D

The objectives of the computational studies are three-fold, *i.e*. firstly, to validate whether the experimental structures represent the global minima through a conformational analysis, an analysis which has significant implications for their molecular packing. Secondly, to gain insight into the electronic nature of the molecules through molecular electrostatic potential (MEP) and natural population analysis (NPA) studies in order to ascertain any particular features in the electronic structures of the molecular that may impact upon the molecular packing. Finally, to qualitatively and quantitatively assess the molecular interactions present in each crystal through Hirshfeld surface analysis, interaction energy calculations, energy framework simulations, lattice energy calculation, non-covalent interaction plots as well as quantum theory of atoms in molecules (QTAIM). The aim of these studies is to correlate molecular conformation and electronic structure to determine and explain the main factors that influence the manner in which the thiourea derivatives pack in their crystals.

Experimental

Instrumentation

All chemicals and solvents were used as purchased without purification. The melting points (uncorrected) were measured using a Stuart SMP30 melting point apparatus. The IR spectra were measured on a Bruker Vertex 70v FT-IR spectrophotometer from 4000 to 80 cm^{-1}. ^{1}H and $^{13}C\{^{1}H\}$ NMR spectra were recorded in DMSO-d_6 solutions on a Bruker Ascend 400 MHz NMR spectrometer with chemical shifts relative to tetramethylsilane (TMS). The absorption spectra were measured on 100 μM acetonitrile solutions in the range 180-700 nm on a double-beam Shimadzu UV 3600 Plus UV-Vis spectrophotometer. The CHN elemental analyses were performed on a LECO TruSpec Micro analyser under a helium atmosphere with glycine being the

View Article Online
DOI: 10.1039/D0CE01810D

standard. The room temperature powder X-ray diffraction (PXRD) patterns were measured on a Rigaku MiniFlex 600 X-ray diffractometer with Cu Kα1 radiation (λ = 1.5418 Å) within a 2θ range of 5-70° and a step size of 0.02°. The comparisons between the experimental and calculated (from the respective CIF) PXRD patterns were performed with Rigaku's PDXL2 software (https://www.rigaku.com/en/products/software/pdxl/overview).

Synthesis

A common mode of synthesis was adopted for the preparation of 1,1-bis(2-hydroxyethyl)-3-phenylthiourea (**1**), 1,1-bis(2-hydroxyethyl)-3-(4-tolyl)thiourea (**2**) and 1,1-bis(2-hydroxyethyl)-3-(4-chlorophenyl)thiourea (**3**). Thus, 1 mmol of the corresponding aryl isothiocyanate (phenyl isothiocyanate (0.135 g); 4-tolyl isothiocyanate (0.149 g); 4-chlorophenyl isothiocyanate (0.169 g) all from Sigma) was reacted with an equimolar amount of diethanolamine (Sigma, 0.105 g) in ethanol (30 ml) followed by stirring for 3 h at room temperature. White precipitates were formed upon the addition of dichloromethane (3 ml). The products were filtered and subsequently washed with cold ethanol (2 ml). Recrystallisation in hot ethanol resulted in the formation of colourless blocks after slow evaporation. For 1,1-bis(2-hydroxyethyl)-3-(4-nitrophenyl)thiourea (**4**), the product was obtained by mixing diethanolamine (1 mmol, 0.105 g) in acetone (5 ml) with an equimolar amount of 4-nitrophenyl isothiocyanate (Acros, 0.180 g) which was pre-dissolved in acetone (30 ml). The mixture was then concentrated to half of the initial volume through slow evaporation with stirring at room temperature. Upon the formation of a yellow precipitate, the product was filtered and washed with a mixture of ethanol and ethyl acetate (4 ml, *v*/*v*). Yellow blocks were obtained through recrystallisation of the crude product in absolute ethanol under slow evaporation.

View Article Online
DOI: 10.1039/D0CE01810D

Characterisation

1: Colourless crystals, yield: 0.188 g (78%). M.pt.: 362.2-363.8 K. Calcd. for $C_{11}H_{16}N_2O_2S$: C 54.98, H 6.71, 11.66%. Found: C 55.01, H 6.79, N 11.38%. IR (ATR, cm^{-1}): 3247 (m) ν(O–H), 3145 (m) ν(N–H), 3093 (m) ν(C–H_{aro}), 3066-2845 (w) ν(C–H), 1312 (s) ν(C–N), 1033 (s) ν(C=S). ^{1}H NMR (DMSO-d_6, ppm): δ 9.72 (s, 1H, NH), 7.29 (m, 4H, *ortho*- and *meta*-phenyl-H), 7.08 (m, 1H, *para*-phenyl-H), 5.31 (br, 2H, OH), 3.84 (t, 4H, $^3J_{HH}$ = 5.3 Hz, CH_2–N), 3.73 (dt, 4H, $^3J_{HH}$ = 5.3 Hz, $^3J_{H\text{-}OH}$ = 4.6 Hz, CH_2–O). ^{13}C{^{1}H} NMR (DMSO-d_6, ppm): δ 182.23 (C=S), 141.34 (*ipso*-C), 128.52 (*ortho*-C), 124.71 (*meta*-C), 124.39 (*para*-C), 59.85 (C–O), 54.78 (C–N). UV/Vis (acetonitrile, 100 μM, nm, L mol^{-1} cm^{-1}): λ_{max}: 277 (sh), ε = 10964; 254, ε = 19953; 222 (sh), ε = 14791.

2: Colourless crystals, yield: 0.207 g (82%). M.pt.: 391.8-392.5 K. Calcd. For $C_{12}H_{18}N_2O_2S$: C 56.67, H 7.13, N 11.01%. Found: C 56.65, H 7.21, N 10.86%. IR (ATR, cm^{-1}): 3258 (m) ν(O–H), 3192 (m) ν(N–H), 3131 (m) ν(C–H_{aro}), 3057-2885 (w) ν(C–H), 1291 (s) ν(C–N), 1025 (s) ν(C=S). ^{1}H NMR (DMSO-d_6, ppm): δ 9.60 (s, 1H, NH), 7.18 (d, 2H, $^3J_{HH}$ = 8.36 Hz, *ortho*-aryl-H), 7.09 (d, 2H, $^3J_{HH}$ = 8.2 Hz, *meta*-aryl-H), 5.29 (br, 2H, OH), 3.83 (t, 4H, $^3J_{HH}$ = 5.36 Hz, CH_2–N), 3.72 (dt, 4H, $^3J_{HH}$ = 5.12 Hz, $^3J_{H\text{-}OH}$ = 4.8 Hz, CH_2–O), 3.06 (s, 3H, CH_3). ^{13}C{^{1}H} NMR (DMSO-d_6, ppm): δ 187.04 (C=S), 143.52 (*ipso*-C), 138.33 (*para*-C), 133.72 (*ortho*-C3), 129.70 (*meta*-C), 64.61 (C–O), 59.50 (C–N), 25.72 (methyl-C). UV/Vis (acetonitrile, 100 μM, nm, L mol^{-1} cm^{-1}): λ_{max}: 278 (sh), ε = 8318; 253, ε = 16218; 222 (sh), ε = 12589.

3: Colourless crystals, yield: 0.215 g (78%). M.pt.: 395.5-396.8 K. Calcd. For $C_{11}H_{15}ClN_2O_2S$: C 48.09, H 5.50, N 10.20%. Found: C 48.01, H 5.58, N 10.02%. IR (ATR, cm^{-1}): 3242 (w) ν(O–H),

View Article Online
DOI: 10.1039/D0CE01810D

3187 (w) ν(N–H), 3127 (w) ν(C–H_{aro}), 3042-2935 (w) ν(C–H), 1301 (s) ν(C–N), 1062 (s) ν(C=S), 691 (m) ν(C–Cl). ^{1}H NMR (DMSO-d_6, ppm): δ 9.76 (s, 1H, NH), 7.34 (s, 4H, *ortho*- and *meta*-aryl-H), 5.32 (br, 2H, OH), 3.85 (t, 4H, $^{3}J_{HH}$ = 5.2 Hz, CH_2–N), 3.73 (dt, 4H, $^{3}J_{HH}$ = 5.04 Hz, $^{3}J_{H\text{-}OH}$ = 4.84 Hz, CH_2–O). ^{13}C{^{1}H} NMR (DMSO-d_6, ppm): δ 186.84 (C=S), 145.06 (*ipso*-C), 133.14 (*ortho*-C), 133.01 (*para*-C), 131.07 (*meta*-C), 64.51 (C–O), 59.57 (C–N). UV/Vis (acetonitrile, 100 μM, nm, L mol^{-1} cm^{-1}): λ_{max}: 282 (sh), ε = 12023; 255, ε = 22909; 226 (sh), 13490.

4: Yellow crystals, yield: 0.224 g (79%). M.pt.: 449.4-450.8 K. Calcd. For $C_{11}H_{15}N_3O_4S$: C 46.31, H 5.30, N 14.73%. Found: C 46.34, H 5.36, N 14.44%. IR (ATR, cm^{-1}): 3259 (w) ν(O–H), 3224 (w) ν(N–H), 3075 (w) ν(C–H_{aro}), 3015-2832 (w) ν(C–H), 1505 (s) ν(N=O_{asym}), 1474 (s) ν(N=O_{sym}), 1291 (s) ν(C–N), 1027 (s) ν(C=S). ^{1}H NMR (DMSO-d_6, ppm): δ 10.37 (s, 1H, NH), 8.18 (d, 2H, $^{3}J_{HH}$ = 9.16 Hz, *meta*-aryl-H), 7.64 (d, 2H, $^{3}J_{HH}$ = 9.04 Hz, *ortho*-aryl-H), 5.82 (br, 1H, OH), 5.18 (br, 1H, OH), 3.88 (4H, t, $^{3}J_{HH}$ = 4.92 Hz, CH_2–N), 3.76 (4H, dt, $^{3}J_{HH}$ = 5.04 Hz, $^{3}J_{H\text{-}OH}$ = 5.16 Hz, CH_2–O). ^{13}C{^{1}H} NMR (DMSO-d_6, ppm): δ 181.50 (C=S), 147.87 (*para*-C), 142.38 (*ipso*-C), 124.59 (*meta*-C), 122.37 (*ortho*-C), 59.61 (C–O), 55.00 (C–N). UV/Vis (acetonitrile, 100 μM, nm, L mol^{-1} cm^{-1}): λ_{max}: 349, ε = 15488; 299 (sh), ε = 10715; 240, ε = 16982; 224 (sh), ε = 14454.

X-ray crystallography

The crystallographic and refinement data for **1-4** are given in Table 1. Intensity data were measured at 100 K on an Agilent Technologies SuperNova Dual diffractometer fitted with an Atlas detector. Data processing and Gaussian absorption corrections were accomplished with CrysAlis Pro.[33] Each structure was solved by direct methods[34] and the refinement was by full-matrix least squares on F^2 with anisotropic displacement parameters for all non-hydrogen atoms.[35] The C-

View Article Online
DOI: 10.1039/D0CE01810D

bound hydrogen atoms were placed on stereochemical grounds and refined with fixed geometries. The O-and N-bound hydrogen atoms were refined with O–H = 0.84±0.01 Å and N–H = 0.88±0.01 Å, respectively. A weighting scheme of the form $w = 1/[\sigma^2(F_o^2) + (0.037P)^2 + 1.248P]$, where $P = (F_o^2 + 2F_c^2)/3$, was introduced in each refinement. Owing to poor agreement, reflections, *i.e.* (1 3 0) for **1** and (-1 0 7) for **2**, were omitted from the final cycles of refinement. Finally, **4** was refined as two-component twin with the fraction due to the minor component = 0.142(3). The programs WinGX,[36] ORTEP-3 for Windows,[36] PLATON[37] and DIAMOND[38] were also used in the study.

Table 1 Crystallographic data and refinement details for **1**–**4**

Compound	**1**	**2**	**3**	**4**
Formula	$C_{11}H_{16}N_2O_2S$	$C_{12}H_{18}N_2O_2S$	$C_{11}H_{15}ClN_2O_2S$	$C_{11}H_{15}N_3O_4S$
Molecular weight	240.32	254.34	274.76	285.32
Crystal size/mm^3	0.30 × 0.30 × 0.30	0.05 × 0.05 × 0.15	0.05 × 0.05 × 0.15	0.30 × 0.35 × 0.40
Colour	colourless	colourless	colourless	yellow
Crystal system	monoclinic	monoclinic	monoclinic	triclinic
Space group	$P2_1/n$	$P2_1/n$	$P2_1/n$	$P\bar{1}$
a/Å	13.4885(1)	7.0472(2)	7.1366(2)	10.8235(5)
b/Å	11.1767(1)	10.7489(2)	10.7767(3)	11.2124(5)
c/Å	16.4909(2)	16.9533(4)	16.6259(4)	12.3443(5)
α/°	90	90	90	90.050(3)
β/°	98.544(1)	99.109(2)	100.221(2)	108.737(4)
γ,/°	90	90	90	114.559(4)
V/Å^3	2458.53(4)	1268.01(5)	1258.39(6)	1274.53(11)

Z	8	4	4	4
D_c/g cm^{-3}	1.299	1.332	1.450	1.487
μ/mm^{-1}	2.253	2.213	4.184	0.269
Measured data	9855	5049	4685	5859
Radiation	Cu Kα	Cu Kα	Cu Kα	Mo Kα
θ range/°	4.0 – 75.0	4.9 – 75.0	4.9 – 75.0	2.3 – 27.5
Unique data	4995	2586	2554	5859
Observed data ($I \geq 2.0\sigma(I)$)	4702	2346	2243	4753
No. parameters	307	164	163	362
R, obs. data; all data	0.030; 0.032	0.029; 0.033	0.031; 0.037	0.041; 0.054
a; b in weighting scheme	0.039; 0.851	0.033; 0.456	0.040; 0.220	0.056; 0.615
R_w, obs. data; all data	0.077; 0.078	0.071; 0.074	0.075; 0.080	0.104; 0.114
Range of residual electron density peaks/eÅ^{-3}	-0.30 – 0.29	-0.22 – 0.21	-0.31 – 0.24	-0.30 – 0.82

View Article Online
DOI: 10.1039/D0CE01810D

Computational studies

A conformational search was performed through a Monte Carlo algorithm using the Merck Molecular Force Field (MMFF),[39] as available in Spartan'16,[40,41] with the energy cut-off being set to 9.6 kcal mol^{-1}. To increase the accuracy on the Boltzmann distribution, the generated conformers were subjected to geometry optimisation using the *ab initio* HF/3-21G model[42,43] followed by energy calculations through the long-range corrected wB97XD density functional with Grimme's D2 dispersion model[44] coupled with Pople's 6-31G(*d*) basis set.[45] The long-range corrected hybrid model has been shown to greatly reduce self-interaction errors and give better accuracy in the interaction energies.[46] Upon elimination of redundant structures with minor conformational changes as well as those exceeding the 9.6 kcal mol^{-1} energy window, the remaining conformers were then submitted for further optimisation at the wB97XD/6-311+G(*d*,*p*) level.[47,48] At this stage, a frequency analysis was performed using the same level of theory and basis set to ensure the validity of the ground state structures. Finally, all identified conformers were submitted into Gaussian16[49] for optimisation using wB97XD with Ahlrichs's valence triple-zeta polarization basis sets (wB97XD/def2-TZVP)[50,51] and with the employment of the Polarisable Continuum Model by placing the solute in a cavity within an ethanol solvent reaction field through the integral equation formalism variant of polarisable continuum model (IEFPCM).[52] The Gibbs free energies were obtained through frequency calculations of the optimised structures at the same level of theory and basis set.

The relative population of each conformer was determined through a Boltzmann weighting factor using equation (**1**),[53] with ΔG_i being the Gibbs free energy of species *i* relative to the most stable conformer, *j* is the specific conformer (*j* = 1, 2, 3…), *R* is the gas constant and *T* is absolute temperature set to 298 K.

View Article Online
DOI: 10.1039/D0CE01810D

$$\text{Boltzmann weighting factor, } P_i = \frac{e^{-\Delta G_i/RT}}{\sum_{j=1} e^{-\Delta G_j/RT}} \times 100\% \qquad (1)$$

Several molecular properties were computed in an attempt to correlate the molecular packing in **1**-**4**. Briefly, the atomic charges for the corresponding optimised structures were obtained by natural population analysis (NPA)[54,55] using wB97XD/def2-TZVP. The electrostatic potential (ESP) was mapped onto the electron density iso-surfaces with constant electronic charge of 0.002 electrons/bohr^3 through the cubegen utility as available in GaussView6.[56] Further, a molecular packing analysis was performed using Mercury,[57] with the analysis criteria being set that only molecules within the 20% tolerance for both distances and angles were included in the calculation while molecules with a variation > 20% were discarded. Differences in the molecular structures (*i.e*. the substituents in the 4-position) and molecular inversions were allowed during the calculation.

For the qualitative evaluation on the strength of interactions, a non-covalent interaction (NCI) visualisation index was generated for the respective interacting dimers using *NCIPLOT*[58] through the plotting of the reduced density gradient as a function of the density across the molecules. The computed density derivatives were mapped as iso-surfaces which correspond to any favourable or unfavourable interactions as determined by the sign of the second density Hessian eigenvalue times the density and visualised using VMD Molecular Graphics Viewer.[59]

Hirshfeld surface mapping, the corresponding two-dimensional fingerprint plots as well as pairwise interaction calculation were generated using Crystal Explorer 17 (ref. 60) through an established method as reported previously,[61] with the experimental structures being used as the input with X–H bond lengths adjusted to their neutron-derived values.[62] The interaction energy calculations were performed using the dispersion corrected CE-B3LYP/6-31G(*d*,*p*) model as

View Article Online
DOI: 10.1039/D0CE01810D

available in the program, with the total intermolecular energy being the sum of energies of four main components, comprising electrostatic, polarisation, dispersion and exchange-repulsion with scale factors of 1.057, 0.740, 0.871 and 0.618, respectively.[63] The model was validated against the B3LYP-D2/6-31G(*d*,*p*) counterpoise corrected energy model as well as the benchmark CCSD(T)/ CBS model with considerable accuracy.[64] The energy frameworks for **1**-**4** were computed for a cluster of 2 × 2 × 2 unit cells with the energy cut-off being set to 1.9 kcal mol^{-1}. Finally, the total energy was obtained for a cluster of molecules within a 25 Å radius from a selected reference molecule through the same level of theory and basis set model. The lattice energy for the corresponding crystals were calculated using equation (2),[65] where the second term is the cell dipole energy correction, with ρ_{cell} being the vector sum of the molecular dipole moments, V_{cell} being the volume and Z being the number of formula units in the unit cell, respectively. Typically, the cell dipole energy correction is negligible (< 0.24 kcal/mol) for a unit cell with small dipole moment.[66]

$$E_{\text{lattice}} = \frac{1}{2}\sum_{R_{\text{AB}} < R} E_{\text{total}}^{\text{AB}} - \frac{2\pi\rho_{\text{cell}}^2}{3ZV_{\text{cell}}} \qquad (2)$$

For **1** and **4**, each with $Z' = 2$, the lattice energy was calculated as the average of lattice sums for each molecule in the asymmetric unit.

Results and Discussion

Synthesis and characterisation

The $(HOCH_2CH_2)_2NC(=S)N(H)(C_6H_4Y\text{-}4)$, Y = H (**1**), Me (**2**), Cl (**3**) and NO_2 (**4**), compounds have been prepared in good yield (78-82%) yield as colourless (**1**-**3**) and yellow (**4**) crystals. In

View Article Online
DOI: 10.1039/D0CE01810D

the IR spectra, characteristic bands in the regions 1291-1312 cm^{-1} and 1025-1062 cm^{-1} are assigned to υ(C–N) and υ(C=S), respectively. In the ^{1}H NMR spectra, measured in DMSO-d_6 solution, the expected resonances and integration, including for the N–H and O–H protons, were noted. In the $^{13}C\{^{1}H\}$ NMR spectra, resonances due to the quaternary-C1 atom were seen downfield, in the range 181.50 (**4**) to 187.04 ppm (**2**). In order to assign the transitions in the UV spectra, an analysis on the HOMO-LUMO profile was performed for the lowest energy conformer at the ground state (*vide infra*) for each of **1**-**4**; see ESI† Fig. S1. This revealed the HOMO is located at the C1=S1 chromophore for **1**-**3**, while the LUMO, LUMO(+1) and LUMO(+2) are located at the delocalised C1=N1/C1=N2, C2=C3 and C4=C5/C6=C7 chromophores, respectively, which indicates that the experimental UV absorption bands at approximately 280, 250 and 220 nm can be attributed to n → π*, π → π* and π → π* transitions, respectively. As for **4**, the delocalised chromophore associated with the nitro group contributes to LUMO(+1) and hence, the additional absorption band at approximately 350 nm can be assigned to π → π*. The PXRD pattern measured for each of **1**-**4** closely match the simulated pattern calculated from their single crystal data, confirming the phase similarity between the respective bulk materials (293 K) and experimental structures (100 K); see ESI† Fig. S2.

Experimental molecular structures

Crystal structures were established for **1**-**4**; for each of **1** and **4**, two independent molecules comprise the asymmetric unit, henceforth **1a** & **1b** and **4a** & **4b**, respectively. The molecular structures are shown in Fig. 2 and selected geometric data are collated in Table 2. The first independent molecule of **1**, Fig. 2(a), features a planar C1,N1,N2,S1 chromophore which exhibits a r.m.s. deviation of 0.0038 Å for the fitted atoms. The mono-substituted amine-N1 atom carries

View Article Online
DOI: 10.1039/D0CE01810D

a phenyl ring and the di-substituted amine-N2 atom carries two hydroxyethyl groups. A significant twist in the molecule is apparent with the dihedral angle between the central plane and appended phenyl ring being 59.39(4)°. This observation plus that the two methylene-C atoms bound to the N2 atom suggests there is not extensive delocalisation of π-electron density over the molecule; the C1–N bond lengths are experimentally equivalent. Consistent with the presence of the C1=S1 double bond at the C1 atom, the angles subtended at the N2 atom involving the C1 atom are the widest. However, the widest angle at a nitrogen atom is the C1–N1–C2 angle which reflects the presence of the amine-H atom. A similar distortion in angles is seen about the C1 atom. Rather than being "dangling", the hydroxyl groups are orientated towards the rest of the molecule enabling the formation of intramolecular hydroxyl-O–H···S(thione) and amine-N–H···O(hydroxyl) hydrogen bonds and *S*(7) loops, as detailed in Table 3. As seen from Table 2, the key bond lengths and angle defining the independent molecules of **1**, Fig. 2(b), are generally close with the most significant difference being a wider angle by about 3° for C1–N1–C2 in the second molecule. Greater differences are noted in torsion angles, Table 2. The maximum difference of approximately 20° is noted in the C1–N1–C2–C3 torsion angles followed by approximately 10° for the N2–C8–C9–O1 torsion angles. A difference of approximately 20° is also seen in the CN_2S/aryl torsion angles with reduced splaying between the planes noted in the second molecule of **1**.

Very similar molecular conformations are noted for **2**-**4**, Figs 2(c)-(f) and Table 2, including the formation of the intramolecular hydrogen bonds, Table 3. The most notable differences between **1** and each of **2**-**4** relate to the more planar S1–C1–N1–C2 torsion angles and to the reduced N2–C10–C11–O2 torsion angles, by up to 18°, in **2**-**4**. Two independent molecules comprise the asymmetric unit of **4** but each presents very similar geometric parameters, Table 2.

View Article Online
DOI: 10.1039/D0CE01810D

However, a distinguishing feature of the two molecules comprising **4** and each of **1**-**3** relates to an apparent disparity in the C1–N1 and C1–N2 bond lengths in **4** not seen in the latter; this observation is discussed further below. An overlay diagram of the experimental molecular structures is shown in Fig. 2(g) from which it is plain that significant conformational differences with respect to the relative orientations of both the hydroxyethyl and aryl groups are evident across the series.

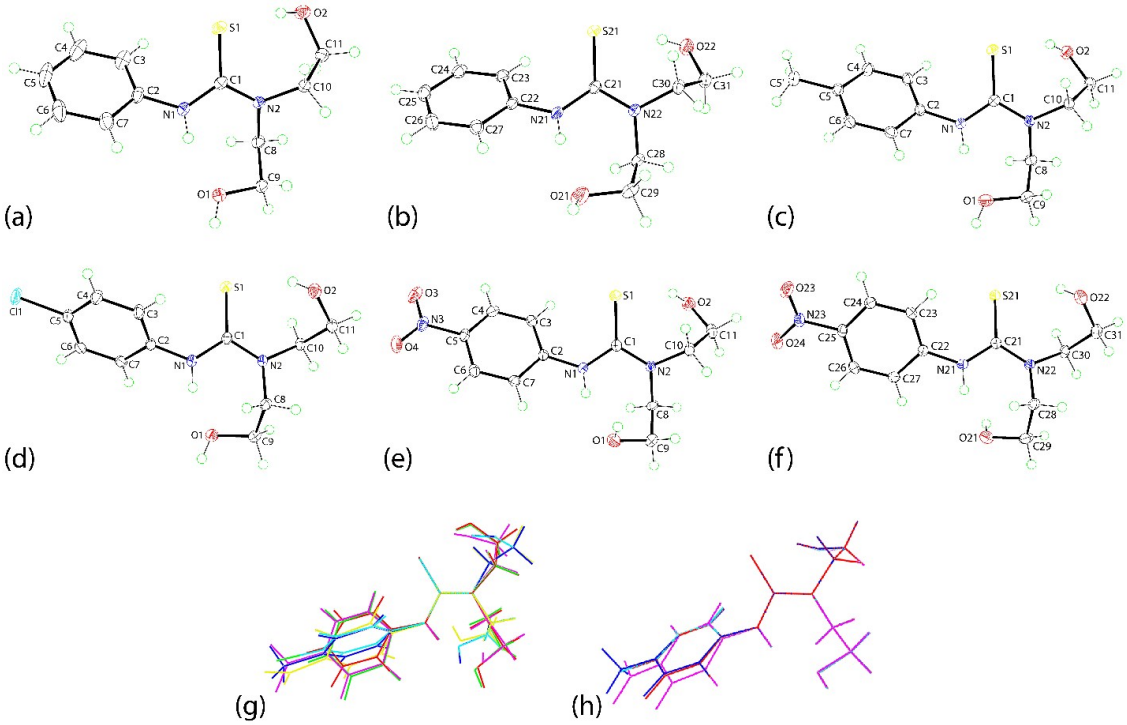

Fig. 2. Molecular structures of (a) **1** (first independent molecule), (b) **1** (second molecule), (c) **2**, (d) **3**, (e) **4** (first independent molecule) and (f) **4** (second independent molecule), all showing atom labelling schemes and displacement ellipsoids at the 50% probability level. Overlap diagrams of the (g) experimental and (h) geometry optimised structures – the molecules have been overlapped so that the central N_2S residues are coincident. Colour code: **1** (first independent molecule), red; **1** (second independent molecule), green; **2** (inverted), blue; **3**, cyan; **4** (first independent molecule), pink; **4** (inverted second independent molecule), yellow.

Table 2 Selected experimental and calculated (in italics) geometric data (Å, º) characterising **1-4**

Parameter	**1a**	**1b**	**2**	**3**	**4a**	**4b**
C1–S1	1.7028(12)	1.6985(12)	1.6986(13)	1.6968(16)	1.6900(18)	1.6893(18)
	1.695		*1.696*	*1.694*	*1.690*	
C1–N1	1.3518(16)	1.3511(15)	1.3573(16)	1.360(2)	1.375(2)	1.374(2)
	1.370		*1.368*	*1.372*	*1.380*	
C1–N2	1.3499(15)	1.3544(15)	1.3539(16)	1.354(2)	1.344(2)	1.345(2)
	1.376		*1.376*	*1.375*	*1.372*	
C1–N1–C2	127.40(11)	130.19(10)	127.08(11)	126.00(14)	128.13(15)	128.95(15)
	128.4		*128.1*	*128.3*	*129.8*	
C1–N2–C8	122.75(10)	122.65(10)	123.22(10)	123.07(13)	123.67(15)	123.44(15)
	122.9		*122.8*	*122.9*	*123.1*	
C1–N2–C10	122.86(10)	122.59(10)	121.49(11)	121.54(13)	121.06(15)	121.47(15)

	120.9		*120.9*	*120.8*	*120.8*	
C8–N2–C10	114.35(9)	114.70(9)	115.29(10)	115.39(12)	115.27(14)	115.08(14)
	115.8		*115.8*	*115.8*	*115.7*	
S1–C1–N1	122.32(9)	123.78(9)	122.78(10)	122.52(12)	122.81(14)	123.14(14)
	123.3		*123.2*	*123.2*	*123.3*	
S1–C1–N2	122.68(9)	121.91(9)	122.69(9)	122.83(12)	123.09(14)	123.10(13)
	122.9		*122.9*	*123.0*	*123.3*	
N1–C1–N2	114.99(10)	114.29(10)	114.52(11)	114.64(14)	114.09(15)	113.74(15)
	113.8		*113.9*	*113.8*	*113.4*	
S1–C1–N1–C2	14.67(18)	13.32(18)	4.79(19)	-5.3(2)	3.9(3)	-5.8(3)
	13.9		*13.2*	*-13.8*	*-19.0*	
C1–N1–C2–C3	51.55(19)	31.80(19)	53.74(19)	-55.6(2)	42.1(3)	-39.5(3)
	44.0		*46.3*	*-43.5*	*-30.8*	
S1–C1–N2–C8	-165.08(9)	-160.46(9)	-166.78(9)	166.73(12)	-166.45(13)	165.12(13)

	-158.3		*-158.1*	*158.6*	*159.8*	
S1–C1–N2–C10	17.34(16)	16.56(16)	13.32(16)	-13.6(2)	13.9(2)	-16.0(2)
	13.1		*13.3*	*-12.8*	*-12.0*	
N2–C8–C9–O1	73.33(12)	82.80(13)	71.13(14)	-71.15(17)	61.7(2)	-63.9(2)
	72.1		*72.3*	*-72.0*		*-71.2*
N2–C10–C11–O2	74.54(13)	73.76(13)	59.47(14)	-58.80(18)	52.5(2)	-55.1(2)
	49.8		*50.0*	*-49.4*	*-48.7*	
r.m.s. deviation CN_2S	0.0038	0.0065	0.0027	0.0036	0.0048	0.0043
CN_2S/aryl	59.39(4)	39.07(4)	54.3(5)	56.98(6)	42.70(7)	41.33(8)
	51.6		*53.2*	*51.0*	*43.4*	

Table 3 Summary of intra- and inter-molecular interactions (A–H···B; Å, º) operating in the crystals of **1-4**

A	H	B	A–H	H···B	A···B	A–H···B	Symmetry operation
1							
N1	H1n	O1	0.873(14)	1.914(14)	2.7514(15)	160.1(15)	*x*, *y*, *z*
O2	H2o	S1	0.841(14)	2.269(15)	3.1009(9)	170.1(13)	*x*, *y*, *z*
N21	H21n	O21	0.872(13)	1.900(14)	2.7624(14)	169.4(13)	*x*, *y*, *z*
O22	H22o	S21	0.838(14)	2.323(15)	3.1470(9)	167.6(14)	*x*, *y*, *z*
O1	H1o	O22	0.839(11)	1.841(11)	2.6753(13)	173.0(17)	*x*, *y*, *z*
O21	H21o	O2	0.842(16)	1.842(16)	2.6825(14)	176.1(15)	*x*, *y*, 1+*z*
C9	H9a	Cg(C22-C27)	0.99	2.68	3.6030(13)	155	1-*x*, 1-*y*, 1-*z*
C9	H9b	Cg(C22-C27)	0.99	2.78	3.6822(13)	151	-½+x, ½-y, - ½+z
C29	H29b	Cg(C2-C7)	0.99	2.95	3.8131(14)	147	1-*x*, 1-*y*, 1-*z*
2							
N1	H1n	O1	0.875(14)	1.906(13)	2.7449(16)	160.1(14)	*x*, *y*, *z*
O2	H2o	S1	0.839(12)	2.367(15)	3.1500(10)	155.4(16)	*x*, *y*, *z*
O1	H1o	O2	0.837(15)	1.882(16)	2.7137(14)	172.0(19)	-½-*x*, -½+*y*, 1½-*z*

C8	H8a	Cg(C2-C7)	0.99	2.89	3.4957(13)	120	-1+*x*, *y*, *z*
C10	H10b	C6	0.99	2.73	3.6263(19)	150	-½+*x*, ½-*y*, -½+*z*
3							
N1	H1n	O1	0.881(18)	1.907(18)	2.7453(19)	158.3(17)	*x*, *y*, *z*
O2	H2o	S1	0.828(13)	2.388(16)	3.1591(13)	155.2(18)	*x*, *y*, *z*
O1	H1o	O2	0.837(17)	1.879(17)	2.7156(18)	178(2)	-½-*x*, ½+*y*, ½-*z*
C8	H8a	Cg(C2-C7)	0.99	2.95	3.5488(17)	120	-1+*x*, *y*, *z*
C10	H10b	Cl1	0.99	2.85	3.6738(14)	141	-1½+*x*, 1½-*y*, -½+*z*
C5	Cl1	Cl1	1.7448(17)	3.4432(6)	–	154.00(6)	2-*x*, 1-*y*, 1-*z*
4							
N1	H1n	O1	0.88(2)	2.03(2)	2.842(2)	153(2)	*x*, *y*, *z*
O2	H2o	S1	0.84(3)	2.40(2)	3.1671(16)	152(3)	*x*, *y*, *z*
N21	H21n	O21	0.88(2)	2.02(2)	2.839(2)	154(2)	*x*, *y*, *z*
O22	H22o	S21	0.839(14)	2.41(2)	3.1767(16)	152(3)	*x*, *y*, *z*
O1	H1o	O22	0.838(19)	1.890(19)	2.723(2)	173(2)	*x*, 1+*y*, *z*
O21	H21o	O2	0.83(2)	1.90(2)	2.732(2)	172.7(19)	*x*, *y*, *z*
C29	H29b	O1	0.99	2.39	3.375(3)	175	-*x*, 1-*y*, 1-*z*

C11	H11b	O3	0.99	2.39	3.360(3)	165	*x*, *y*, 1+*z*
C10	H10b	Cg(C22-C27)	0.99	2.72	3.475(2)	133	1-*x*, 1-*y*, 2-*z*
C9	H9b	Cg(C2-C7)	0.99	2.71	3.483(2)	135	1-*x*, 1-*y*, 1-*z*
Cg(C22-C27)		Cg(C22-C27)	–	–	3.6105(12)	0	-*x*, -*y*, 2-*z*

Molecular packing

The geometric parameters characterising the specific intermolecular contacts operating in the crystals of **1**-**4** are collated in Table 3. The common feature of the supramolecular aggregation is the formation of supramolecular chains mediated by hydroxyl-O–H···O(hydroxyl) hydrogen bonding. However, the topologies of the resultant chains are distinct. In **1**, the two similarly orientated molecules comprising the asymmetric unit are connected by a single hydroxyl-O–H···O(hydroxyl) hydrogen bond and the resultant two-molecule aggregates are connected into a linear supramolecular chain parallel to the *c*-axis in the crystal with monoclinic space group $P2_1/n$. In isostructural **2** and **3**, helical chains are formed, being propagated by 2_1-screw symmetry along the *b*-axis in monoclinic space group $P2_1/n$, in their crystals. In **4**, the independent molecules are connected into a V-shaped aggregate which are connected to translationally related aggregates to form a zig-zag chain along the *b*-axis in the triclinic ($P\bar{1}$) crystal. The side- and end-on views of the supramolecular chains are illustrated for **1**, **2** and **4** in Fig. 3, and for **3** in ESI† Fig. S3. The differences in the topologies is reflected in the distances between translationally related pairs of molecules, *i.e.* 16.49, 10.75, 10.77 and 11.21 Å, respectively, indicating more open arrangements in the sequence **1** > **4** > **3** and **2**.

View Article Online
DOI: 10.1039/D0CE01810D

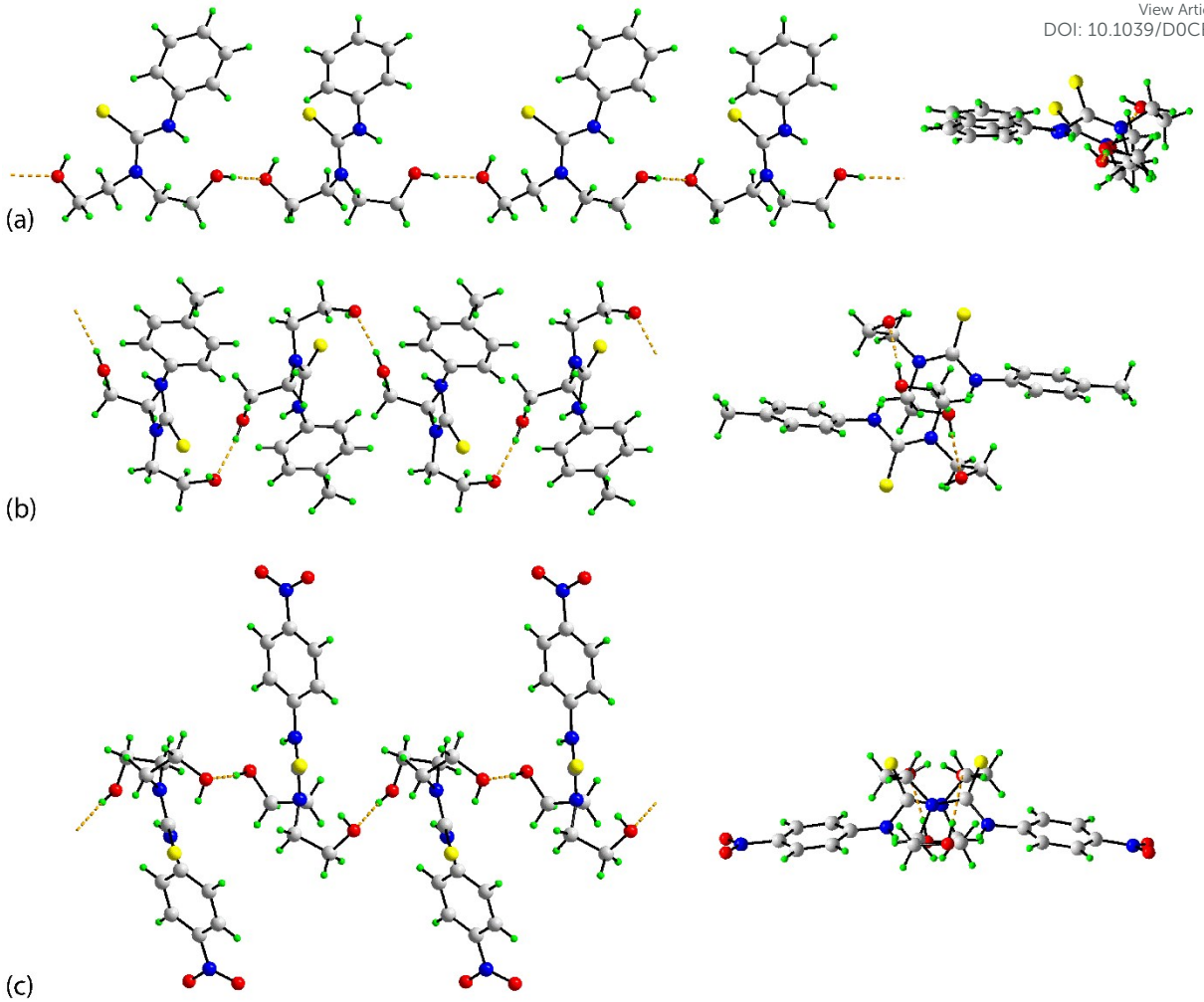

Fig. 3. Side- and end-on views of the supramolecular chains featuring by hydroxyl-O–H···O(hydroxyl) hydrogen bonding, shown as orange dashed lines, in the crystals of (a) **1**, (b) **2** and (c) **4**.

In **1**, the only other identifiable points of contact between the supramolecular chains are methylene-C–H···π(aryl) interactions, with the C22-C27 ring accepting two interactions to either side, and these serve to assemble the chains into a three-dimensional architecture, Fig. 4(a).

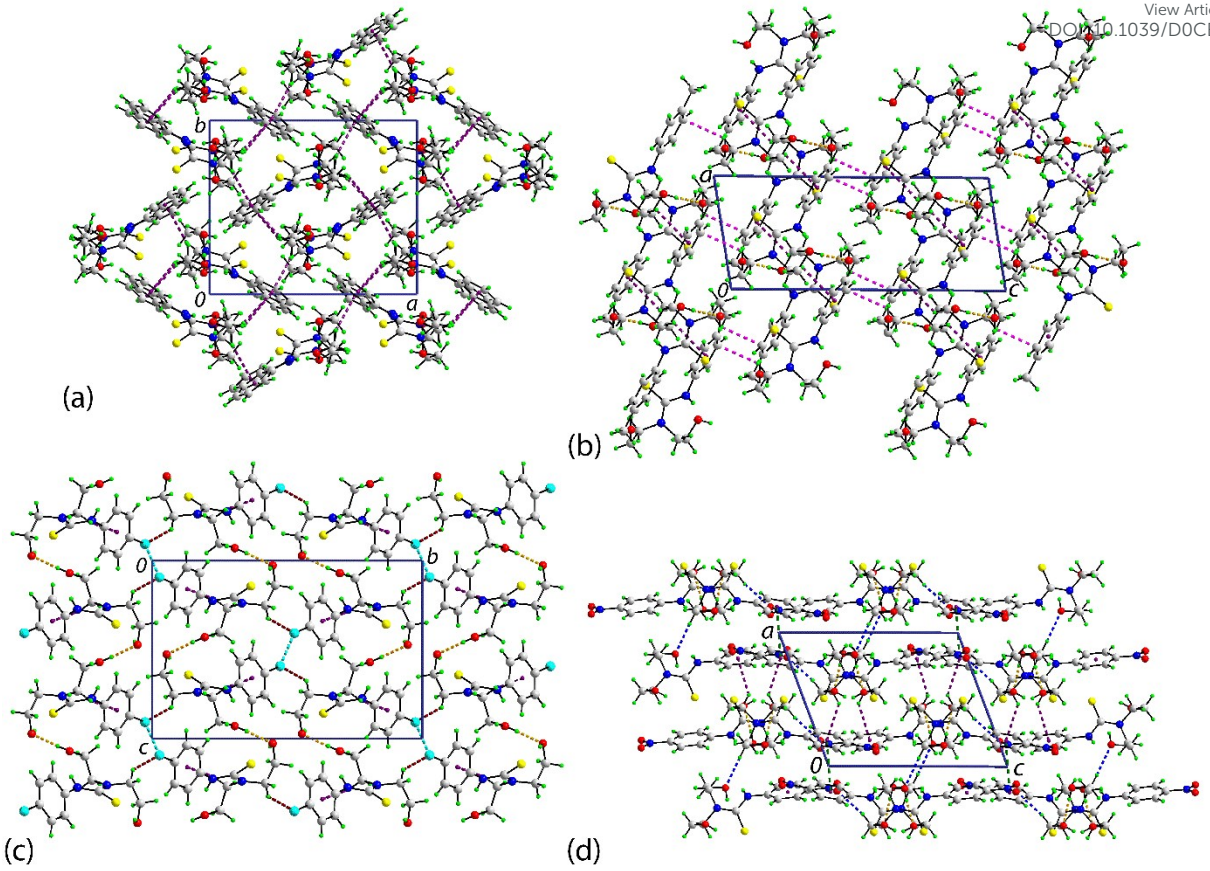

Fig. 4. Unit-cell contents for (a) **1**, viewed down the *c*-axis, (b) **2**, viewed down the *b*-axis, (c) **3**, viewed down the *a*-axis and (d) **4**, viewed down the *b*-axis; the views in (a), (b) and (d) are in projection down the axes of propagation of the chains. The hydroxyl-O–H···O(hydroxyl), methylene-C–H···π(aryl), methylene-C–H···C(aryl), methylene-C–H···Cl, Cl···Cl, methylene-C–H···O(hydroxyl, nitro) and π(aryl)···π(aryl) interactions are shown as orange, purple, pink, dark-red, cyan, blue and dark-green dashed lines, respectively.

In the crystal of **2**, the chains are connected into a two-dimensional array in the *ab*-plane by methylene-C–H···π(C2-C7) interactions. The layers stack along the *c*-axis with the closest interaction between them being a methylene-C–H···C(aryl) contact, Table 3. A view of the unit-cell contents for isostructural **3** is shown in Fig. 4(c). Here, there is evidence for weak inter-layer methylene-C–H···Cl and Cl···Cl contacts, Table 3. A distinct molecular packing is

View Article Online
DOI: 10.1039/D0CE01810D

noted in the crystal of **4** primarily owing to the participation of hydroxyl- and nitro-O atoms along with face-to-face π···π contacts, Table 3. Thus, the methylene-C–H···π(aryl) contacts, present in all crystals connect chains into a centrosymmetric double-layer in the *bc*-plane, within which are supporting methylene-C–H···O(nitro) contacts. The double-layers stack along the *a*-axis with methylene-C–H···O(hydroxyl) and π(aryl)···π(aryl) contacts assembling the layers into a three-dimensional architecture, Fig. 4(d). The π(aryl)···π(aryl) contacts occur between centrosymmetrically related residues and the rings are off-set to optimise the attraction: the inter-plane separation is 3.4128(8) Å and the slippage is 1.18 Å.

Molecular packing similarity analysis

A packing similarity analysis was performed between **1**-**4** to identify any similarities in the molecular arrangements in their crystals.[57] The results show that the packing in **1** is quite distinct to that of **2**, **3** and **4**, with only one molecule out of 15 falling within the 20% tolerance in both distance and angle deviations. The r.m.s. deviation between **1** & **2**, **1** & **3** and **1** & **4** amounts to 0.946, 0.931 and 0.934 Å, respectively. The major deviation arises as in the crystal of **1**, the molecules are mainly connected through hydroxyl-O–H···O(hydroxyl) interactions in a linear arrangement, while in each of **2**-**4**, the molecules are connected by the same interaction but arranged in a helix (**2** and **3**) and a zig-zag chain (**4**), as highlighted in the overlay diagrams for **1** & **2** and **1** & **4** of Figs 5(a) and (b), respectively. For comparison, Fig. 5(c) shows the equivalent image for isostructural **2** and **3** where the r.m.s. deviation is 0.173 Å. An intermediate situation when **2** (and **3**) is compared with **4**, Fig. 5(d), where the r.m.s. deviation is 0.388 Å; the r.m.s. deviation between **3** and **4** is 0.461 Å. A closer inspection of the supramolecular chains of **2** and **4**, Fig. 5(e), shows every second molecule of **2** has an alternate

orientation, reflecting the 2_1-screw symmetry, compared with the molecules having the same relative orientation reflecting the pseudo-mirror symmetry of the zig-zag chain of **4**.

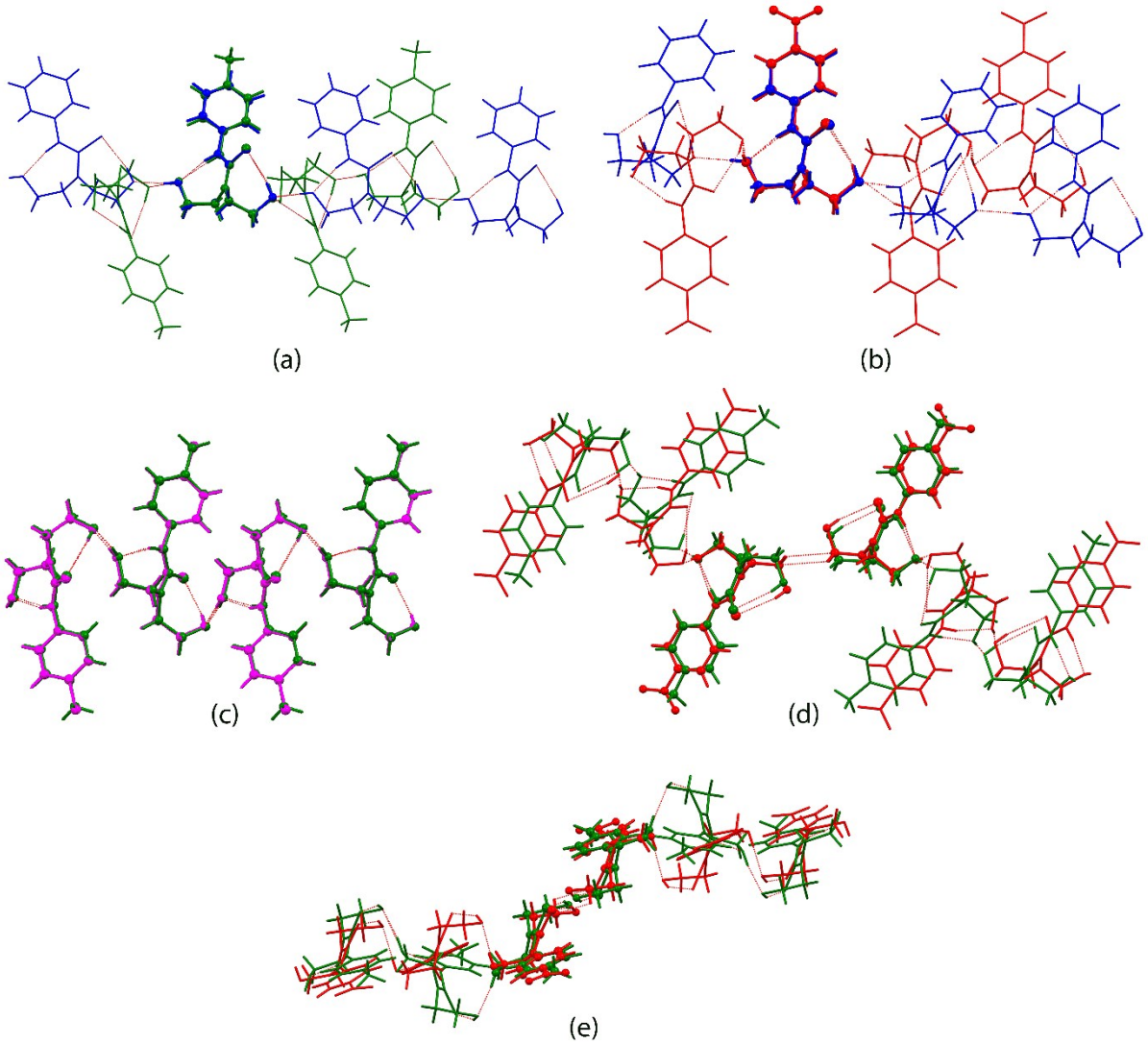

Fig. 5 Comparisons of the molecular packing leading to the supramolecular chains (only four molecules of each are shown) between (a) **1** (blue) and **2** (green), (b) **1** and **4** (red), (c) **2** and **3** (magenta), (d) **2** and **4** and (e) end-on view of **2** and **4** with the differently-orientated hydroxyl-O–H···O(hydroxyl) interactions. In (a)-(e), best-fitting molecules are highlighted in ball and stick representation.

Conformational analysis

Owing to the presence of the hydroxyethyl moieties in **1-4**, which may participate in various intra- and inter-molecular interactions depending on the conformations they adopt, a detailed conformational analysis of a representative molecule, namely **4**, was conducted to assess whether the observed experimental structure represents a conformation at or close to the global minimum on the potential energy surface. A striking feature of the molecular structures of **1-4** was the universal formation of intramolecular hydroxyl-O–H···S(thione) and amine-N–H···O(hydroxyl) hydrogen bonds, Fig. 2 and Table 3. The (any atom)N(H)C(=S)N(CH_2CH_2OH)$_2$ fragment is relatively rare in the crystallographic literature,[67] being restricted to a small number of ArC(=O)N(H)C(=S)N(CH_2CH_2OH)$_2$ molecules[68-71] and a bi-functional analogue.[72] A common feature of the literature precedents is the formation of the intramolecular amine-N–H···O(hydroxyl) hydrogen bonds but no analogous intramolecular hydroxyl-O–H···S(thione) interactions as in **1-4**. Given this observation, it was thought of interest to ascertain whether the orientations of the flexible hydroxyethyl residues in **1-4** corresponded to the global potential energy minima. Accordingly, a conformational analysis through a series of optimisation steps (see *Experimental*) was performed on a representative molecule, namely, **4**. In all, nine conformers with lowest energy were identified upon consecutive elimination of the redundant conformers and those with the relative energy exceeding 9.6 kcal mol^{-1} throughout the series of optimisation steps. As validated through the vibrational analysis with zero imaginary frequency, final optimisation showed that all nine conformers were either true local minima or the global minimum structure on the potential energy surface. The chemical diagrams for the identified conformers together with the energy details are presented in Fig. 6. Clearly, among all possible conformations identified for **4**, conformer **4-1** is the global minimum structure with the lowest Gibbs free energy and is also the most dominant conformer with the highest relative population of about 82%. Two other conformers lie within 2 kcal mol^{-1}, namely **4-2** and **4-3**, with Boltzmann populations of 10.45

and 3.52%, respectively. Clearly, the intramolecular hydrogen bonds play a crucial role in stabilising the observed molecular conformation, by about 1-5 kcal mol^{-1} compared to the conformation without intramolecular hydrogen bonding, *i.e.* **4-9**.

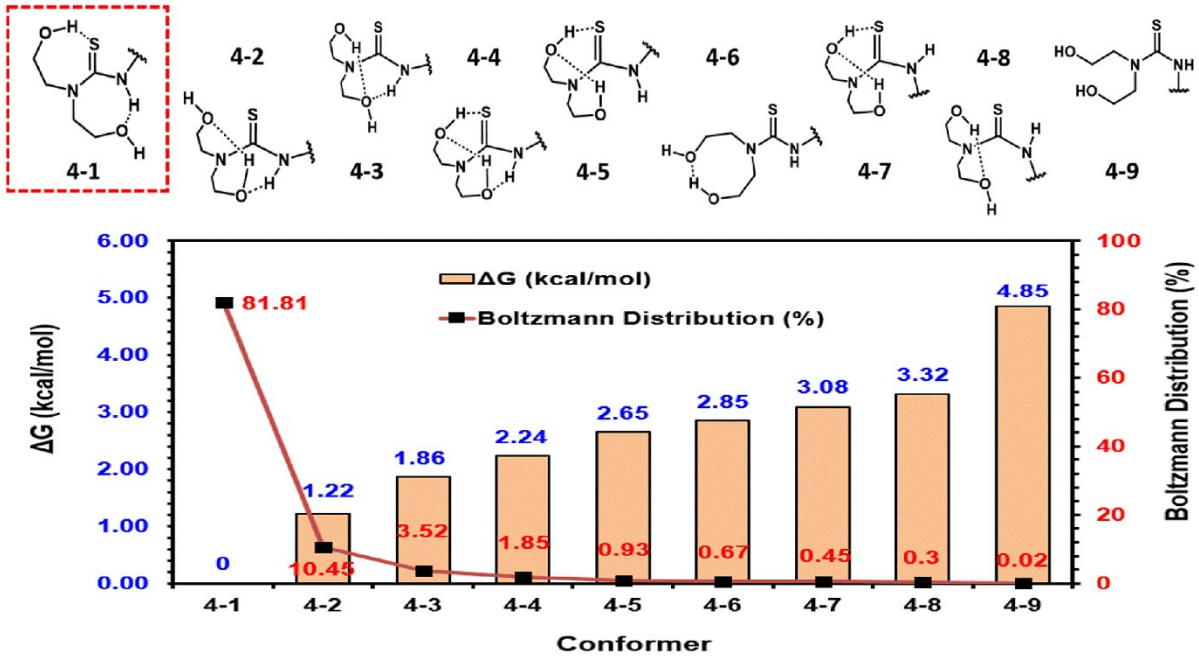

Fig. 6 Chemical diagrams for the nine most stable conformers calculated for **4**, *i.e.* **4-1** to **4-9**, their relative energies and Boltzmann distribution.

Additional structural information was revealed through this analysis. Crucially, the six most stable conformations, **4-1** to **4-6**, have an *anti*-disposition of the thione-S and amine-H atoms, with S1–C1–N1–H1n torsion angles in the range 140.1 to 156.9°, compared *syn*-dispositions in **4-7** to **4-9** (S1–C1–N1–H1n: 19.7 to 20.8°) with the difference in energy between **4-6** and **4-7** being 0.2-0.3 kcal mol^{-1}. The analysis also highlights the importance of the intramolecular amine-N–H···O(hydroxyl) hydrogen bonds compared with the hydroxyl-O–H···S(thione) and putative hydroxyl-O–H···O(hydroxyl) hydrogen bonds, with conformers **4-1** to **4-4** being lower in energy compared with conformers without amine-N–H···O(hydroxyl) hydrogen bonds.

Geometry optimisation calculations for **1-4** were conducted and an overlay diagram for these are shown in Fig. 2(h) from which it can be seen that the disparities in the conformations of the experimentally-determined structures no longer persist, with only minor differences noted in the relative orientations conformations of the aryl groups. Selected geometric parameters for the optimised structures are collated in Table 2. First and foremost, any differences apparent between the independent molecules of **1** and of **4** are no longer apparent. For example, the difference in the C1–N1–C2 angles of approximately 3° in **1** disappears. Concerning the relative dispositions of the aryl groups, Fig. 2(h), it was noted above the S1–C1–N1–C2 angles in experimental **2-4** were closer to planarity compared with **1** but in the optimised molecules, all approximate the conformation seen in experimental and theoretical **1**, yet a range of angles, *i.e.* 13.2° (**2**) to -19.0° (**4**) is still apparent. This along with a range of about 12° for the C1–N1–C2–C3 torsion angles are the exceptional differences with all of the other angles equal within a degree of each other. With respect to bond lengths, in the crystals of **1-3** the C1–N1, N2 bond lengths are equal within experimental error but are distinct for each independent molecule in **4**, Table 2. In the optimised structures, C1–N2 is marginally longer than C1–N1 in **1-3** but, for **4**, there are more significant differences apparent with the C1–N1 bond length being longer than C1–N2. This change is related to the influence of the electronegative nitro substituent in **4**. The above systematic variations in geometric parameters notwithstanding, it is emphasised the differences are small and are unlikely to have a significant influence upon the molecular packing.

Molecular electrostatic potential (MEP) and natural population analysis (NPA)

Compounds **1-4** were subjected to molecular electrostatic potential (MEP) mapping and a natural population analysis (NPA) in order to better comprehend the distribution of electron density over the molecules (the relative polarity) with the view to correlate any systematic

trends with the non-covalent interactions operating in the respective crystals. It is noted that the NPA approach was chosen for the charge calculations for its reliability and for being less sensitive to the choice of basis set functions.[73]

As shown in Fig. 7, the MEP maps were plotted onto the iso-density surfaces (0.0004 a.u., the low value being chosen for the generation of high-quality mapping) for **1**-**4**; a listing of the electrostatic charges is given in ESI† Table S1. The most noteworthy features of the MEP plots are the intense positive (blue) regions centred on the H1o atoms as well as the negative (orange to red) regions around the S1 and O2 atoms with the electrostatic potential charge (V_{ESP}) on the surfaces being in the range of +55.73 to +59.49 kcal mol^{-1} for H1o, -30.37 to -36.09 kcal mol^{-1} for S1, and -39.30 to -42.45 kcal mol^{-1} for the O2 atom. The electrostatic potential charges correspond well with the experimental findings in that electropositive-H1o interacts with electronegative-O2 through charge-complementary, electrostatic attractions that results in systematic hydroxy-O–H···O(hydroxy) hydrogen bond formation in **1**-**4**. While there are some inequivalent distributions of electrostatic potential charge on the H1o and O1 atoms in **1**-**4**, the net charge (ΔV_{ESP}) is approximately the same across the series with the values being 97.74, 98.44, 98.72 and 98.79 kcal mol^{-1}, respectively, indicating similar strengths for these interactions. These net charge values are relatively greater than the electrostatic attraction for putative methylene-C–H···S(thione) interactions in the molecular packing for **1** and **4**, with energies of 65.12 and 66.61 kcal mol^{-1}, respectively and aryl-C–H···S(thione) for **1** with an energy = 41.05 kcal mol^{-1}. However, in **1**, these occur at distances beyond the van der Waals radii so are not indicated in the analysis conducted using *PLATON*[37] but are noted in the Hirshfeld surface analysis (*vide infra*). The identified methylene-C–H···Cl1 and Cl···Cl interactions in **3**, Table 3, have net charge values of 32.40 and -1.88 kcal mol^{-1}, respectively, indicating the latter is diffusive in nature. As well, methylene-C–H···O(nitro) and aryl-C–

View Article Online
DOI: 10.1039/D0CE01810D

H···O(nitro) in **4** have energies equal to 49.43 and 44.72 kcal mol^{-1}, respectively; the latter occur at separations greater than the van der Waals radii.

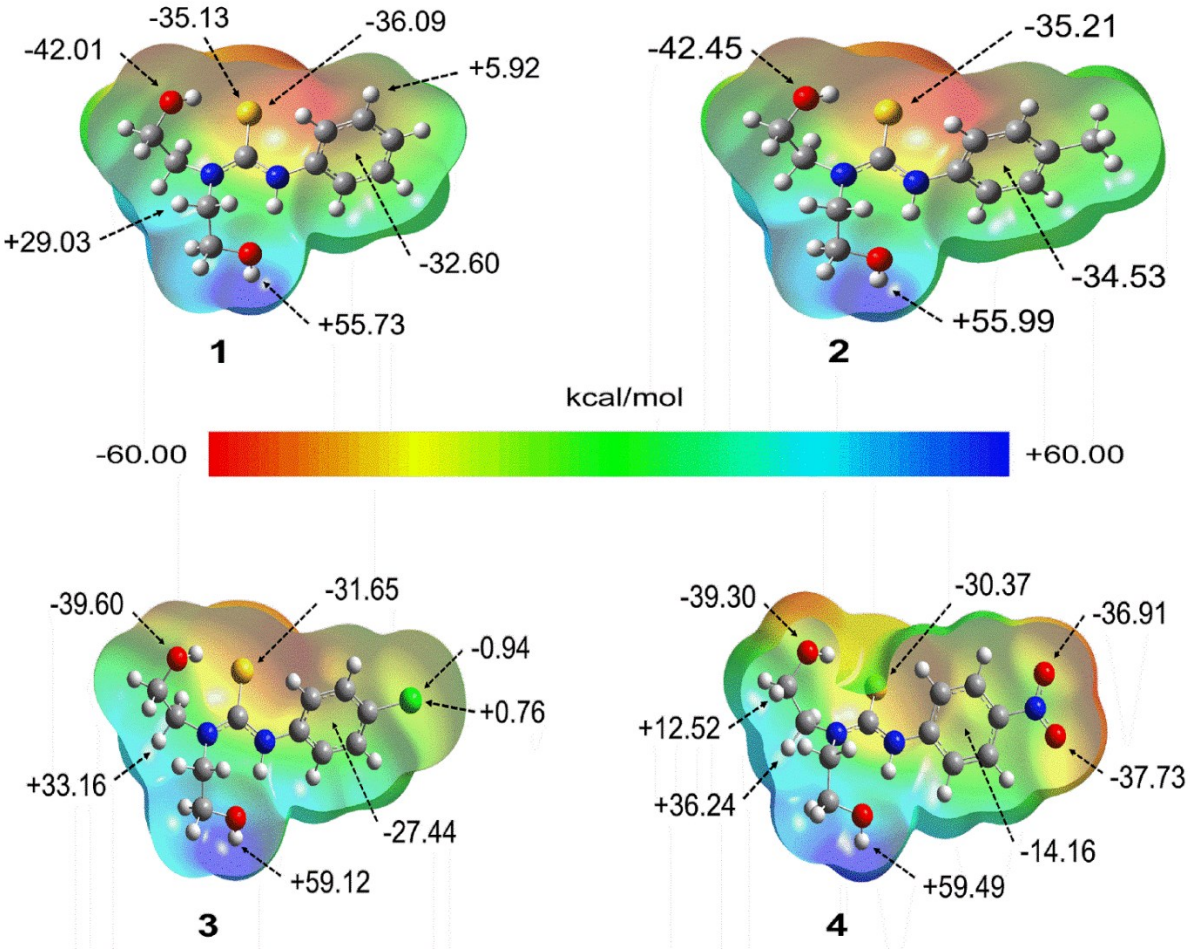

Fig. 7 Electrostatic potentials mapped onto the iso-density surfaces (0.0004 a.u.) for **1**-**4**, in the range -60.00 to +60.00 kcal mol^{-1}.

The effect on the variation of the 4-Y substituent of the aryl rings is evidenced through MEP mapping. Thus, the electrostatic charge on the centroid of the aryl ring becomes more negative from **1** to **2** due to the electron donating nature of the Y = Me substituent in **2**, while the opposite is true for **3** and **4**, as the aryl rings become less negative owing to the electron-withdrawing effects of the Y = Cl and NO_2 substituents.

Similar to the MEP analysis, the NPA study was conducted to seek trends in the charge distribution on specific atoms especially those participating in intermolecular interactions for

correlation with molecular packing. A list of selected NPA values is given in Table 4 and a full listing is given in ESI† Table S2. The NPA charge analysis shows that the most basic sites are located on the hydroxyl-O1 and O2 atoms with the natural charge values in the ranges -0.736 to -0.737 and -0.743 to -0.749, respectively, indicating the O2 atom is marginally more negative. The corresponding H1o and H2o atoms are the most acidic sites with charge values of about 0.50 and 0.48, respectively, in accord with the trends with the hydroxyl-O atoms. Consistent with the MEP study, are the relatively large difference in the natural charges between the hydroxyl-oxygen and -hydrogen atoms and this is the main contributing factor for the formation of the common hydroxy-O–H···O(hydroxy) hydrogen bonded chain formation in **1**-**4**.

Table 4 The natural charges for selected atoms in the optimised molecules of **1**-**4**.

Atom	Natural Charge, |e|			
	1	**2**	**3**	**4**
S1	-0.393	-0.397	-0.387	-0.361
N1	-0.613	-0.611	-0.613	-0.614
N2	-0.396	-0.397	-0.393	-0.384
O1	-0.737	-0.737	-0.737	-0.736
O2	-0.748	-0.749	-0.747	-0.743
C1	0.345	0.346	0.344	0.338
C2	0.141	0.126	0.141	0.195
C3	-0.215	-0.205	-0.197	-0.222
C4	-0.208	-0.212	-0.224	-0.169
C5	-0.226	-0.024	-0.053	-0.010
C6	-0.205	-0.209	-0.222	-0.164
C7	-0.234	-0.224	-0.216	-0.235
H1o	0.496	0.496	0.496	0.498

View Article Online
DOI: 10.1039/D0CE01810D

H2o	0.480	0.480	0.480	0.480
H1n	0.444	0.444	0.445	0.448

It is noted that small but consistent trends in the charges residing on the S1 and N2 atoms are apparent, with respect to **1**, minor increases in **2** and decreases in **3** and **4** correlated with the electronegativity of Y. Variations in the natural charges are also noted in the aryl rings, in particular for the C5 atoms with respect to **1**, observations again related to the Y-substituents. For **2**, the inductive effect of the σ-electron donating methyl group disperses charge around the π-system through the resonance effect.[74] A similar observation is found for the Cl substituent in **3** as it able to donate the lone-pair of electrons to the aryl ring leading to a similar inductive effect as for the methyl substituent despite the chloride atom being known as a weak electron-withdrawing group.[75] The significant differences for all atoms comprising the aryl ring in **4** relates specifically to the electronegative nitro substituent. Overall, the net charge shift[76] for the 4-substituted phenylthiourea fragments compared to the parent molecule, *i.e.* [Σ*q*($SCNHC_6H_4Y$) - Σ*q*($SCNHC_6H_5$)], computes to 0.004, -0.007 and -0.033 e for **2**-**4**, respectively, which correlates to the electron-donating nature of Me and electron-withdrawing characteristics of Cl and NO_2.

Hirshfeld surface analysis

Compounds **1**-**4** were subjected to Hirshfeld surface analysis in order to gain further insight on the nature of interactions present in each crystal, especially those not identified in the conventional analysis of the molecular packing, as well as important surface contacts; the analysis includes the contributions made by the individual components comprising the asymmetric unit of each of **1** and **4**, labelled henceforth **1a** & **1b** and **4a** & **4b**, respectively The mapping of the normalised contact distances (d_{norm}) reveals several red spots on the iso-

density surfaces of the molecules ranging from strong to weak intensity due to the presence of several close contacts with separations shorter than the sum of van der Waals radii.[62] These are categorised into five main types as H···O/O···H (type I), H···C/C···H (type II), H···S/S···H (type III), C···O/O···C (type IV) and H···Cl/Cl···H or Cl···Cl (type V), Fig. 8. A summary of the contacts detected on the Hirshfeld surfaces is provided in ESI† Table S3 where all the X–H bond lengths have been adjusted to their neutron values.

The most intense red spots arise from H···O/O···H interactions due to the hydroxyl-O–H···O(hydroxyl) hydrogen bonds and these are a common feature of all crystals under investigation. The differences between the molecules are observed mainly in the diminutive red spots comprising type II, III, IV and V contacts. For instance, a type IV contact appears only for **1b** due to thiourea-C1···O(hydroxyl) interaction, while type III contacts are observed in **1** and **4** attributed to methylene-/aryl-C–H···S(thione) interactions but no such contact is noted either of **2** and **3**. The inclusion of Cl and NO_2 substituents in the 4-positions of **3** and **4** introduces additional contacts compared with the parent molecule of **1** as evidenced from the presence of red spots, albeit of weak intensity. For **3**, these arise from methylene-C–H···Cl and Cl···Cl interactions in **3**; while the NO_2 substituent in **4** gives rise to methylene-/aryl-C–H···O(nitro) interactions. Almost all of these interactions identified through the Hirshfeld surface analysis can be considered weak contacts which complement those interactions detected *via PLATON*.[37]

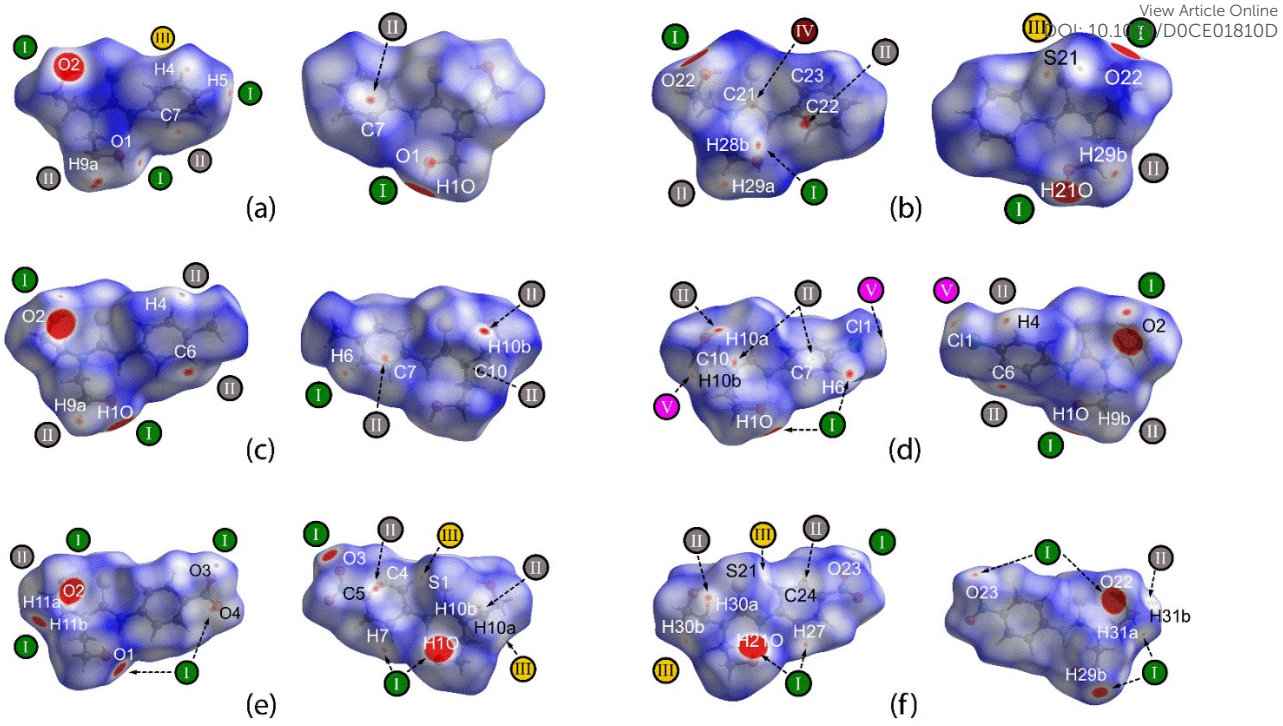

Fig. 8 Complementary views of the Hirshfeld surface mapped over d_{norm} within the range of -0.0788 to 1.0548 arbitrary units, revealing close contacts shorter than the sum of van der Waals radii through red spots on the surfaces which are categorised into H···O/O···H (type I), H···C/C···H (type II), H···S/ S···H (type III), C···O/O···C (type IV) and H···Cl/Cl···H or Cl···Cl (type V) for (a) **1a**, (b) **1b**, (c) **2**, (d) **3**, (e) **4a** and (f) **4b**.

The quantification of the close contacts to the Hirshfeld surface was achieved though the analysis of the two-dimensional fingerprint plots for the respective molecules in **1-4**. In general, the variation of intermolecular interactions owing to the differences in molecular packing is reflected in the fingerprint profiles for the individual molecules, despite these often being subtle, particularly in the diffuse regions of the overall profiles as illustrated in ESI† Fig. S4.

The most prominent features of the fingerprint plots are the pairs of forceps-like spikes tipped at $d_i + d_e$ distances within 1.70-1.76 Å which are much shorter than the sum of van der

Waals radii (vdW) for O···H [$\Sigma(\text{vdW})_{\text{O}\cdots\text{H}}$ = 2.61 Å], *cf.* the d_{norm} contact distances listed in ESI† Table S3. These features arise due to the H···O/O···H hydrogen bonding contacts leading to the supramolecular chains. Also prominent are the pincers-like distributions in the decomposed fingerprint plots for the H···C/C···H contacts with $d_i + d_e$ distances in the range 2.65-2.76 Å which are slightly shorter than $\Sigma(\text{vdW})_{\text{C}\cdots\text{H}}$ of 2.79 Å. The H···S/ S···H contacts are also reflected as pincers-like profile but with $d_i + d_e$ distances in range 2.83 to 2.94 Å for **1** & **4** and 2.90 to 3.03 Å for **2** & **3** compared with the $\Sigma(\text{vdW})_{\text{S}\cdots\text{H}}$ = 2.89 Å. It is for this reason that diminutive red spots were observed in the relevant plots for **1** and **4** but not in those for **2** & **3**; as discussed below, the H…S contacts in **2-4** are intra-chain contacts. Distinctive characteristics are noted in **3** arising from H···Cl/Cl···H as well as Cl···Cl contacts with $d_i + d_e$ of about 2.78 and 3.42 Å which are shorter than $\Sigma(\text{vdW})_{\text{Cl}\cdots\text{H}}$ and $\Sigma(\text{vdW})_{\text{Cl}\cdots\text{Cl}}$ of 2.84 and 3.50 Å, respectively, Fig. 9. Other contacts co-exist on the Hirshfeld surface but are less significant owing to long contact separations.

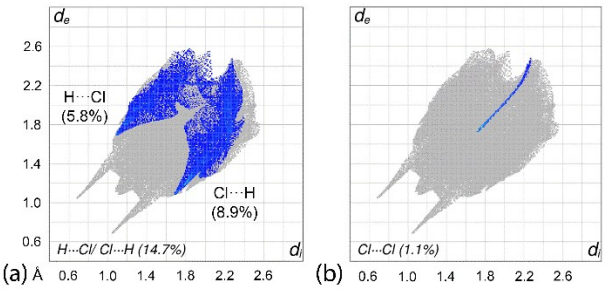

Fig. 9 Decomposed fingerprint plots for **3** delineated into (a) H···Cl/Cl···H and (b) Cl···Cl contacts.

In terms of contact distributions, crystals **1** and **2** are dominated by several major contact contributions to the Hirshfeld surfaces in the order of H···H (*ca* 57.3-59.5%), H···C/C···H (*ca*

View Article Online
DOI: 10.1039/D0CE01810D

17.2-18.7%), H···S/S···H (*ca* 10.6-12.0%) and H···O/O···H (*ca* 8.4-10.8%) followed by other less significant contacts with each contributing less than 1% as shown in Fig. 10. The decomposition of the distribution shows that almost all contacts in **1** and **2** are evenly distributed between the internal (*i.e.* the donor or acceptor atoms internal to the surface) and external (*i.e.* the donor or acceptor atoms external to the surface) interactions except for H···C/C···H and H···S/S···H which are slightly inclined toward (internal)-X···H-(external) rather than (internal)-H···X-(external) (X = C and S) owing to their relatively large exposure surfaces that attract the contact from hydrogen atoms, *e.g.* for C···H, the contact is mainly concentrated within the aryl ring with a large exposure surface.

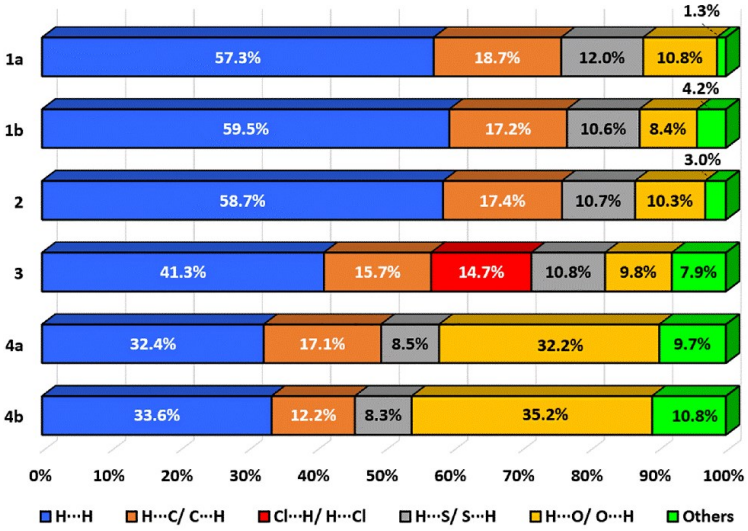

Fig. 10 Relative distribution of different contacts to the Hirshfeld surfaces for individual molecules in **1-4**. Other minor but significant contacts include C···Cl/Cl···C (2.8%), H···N/N···H (2.3%) and Cl···Cl (1.1%) for **3**. For **4a** and **4b**: H···N/N···H (2.5%), O···C/C···O (1.0-2.3%), O···S/ S···O (1.4-1.5%) and O···O (0.1-1.3%), and specifically for 4**b** C···C (3.0%).

View Article Online
DOI: 10.1039/D0CE01810D

Distinctive distributions are noted for each of **3** and **4** owing to the influence of the X = Cl an NO_2 substituents, respectively. Thus for **3**, the contributions are in the order H···H (41.3%), H···C/C···H (15.7%), H···Cl/Cl···H (14.7%), H···S/S···H (10.8%) and H···O/O···H (9.8%) and other minor contacts including the Cl···Cl contact which constitutes only 1.1%. For **4**, the order is H···O/O···H (*ca* 32.2-35.2%), H···H (*ca* 32.4-33.6%), H···C/C···H (*ca* 12.2-17.1%), H···S/ S···H (*ca* 8.5%) followed by other long contacts (*ca* 9.7-10.8%). Similar to **1** and **2**, decomposition of the corresponding contacts exhibits uneven distributions between the internal and external contacts for H···Cl/Cl···H in **3** as well as H···O/O···H in **4** in addition to the H···C/C···H and H···S/S···H contacts in both molecules, for which the interactions are inclined toward (internal)-X···H-(external) (X = Cl, O, C and S) indicating the electronegative nature of those acceptor atoms.

Interaction energies and energy frameworks

An analysis of the interaction energies associated with identified intermolecular contacts was quantitatively assessed in attempt to rank the stabilisation energies provided by specific contacts in **1-4**. The strength of each interaction as identified from the Hirshfeld surface analysis was assessed following the approach as detailed in the experimental section. As noted from Table 5, among all pairwise-interactions between molecules, the hydroxyl-O–H···O(hydroxyl) interactions provide the strongest interactions with the energy, E_{int}, for each pair lying in the range -17.81 to -12.09 kcal mol^{-1}. These strengths are comparable to that of *ca* -18 and -17 kcal mol^{-1} as calculated for the classical amide-N–H···O(amide)[77] and carboxylic-O–H···O(carboxylic acid) interactions,[78] respectively. A close inspection of the data shows that the E_{int}(O–H···O) is the greatest in crystal **2**, and this is followed by **3**, **4** and **1** respectively.

View Article Online
DOI: 10.1039/D0CE01810D

Apart from the O–H···O interactions, crystals **1-4** also feature C–H···O and C–H···π interactions with the E_{int} ranging from -2.27 to -10.56 kcal mol^{-1} and -4.09 to -8.58 kcal mol^{-1}, respectively. Additional C–H···S and C···O interactions found in **1** have relatively strong interaction energies with E_{int}(C–H···S) in the range -2.20 to -7.93 kcal mol^{-1} and E_{int}(C···O) in the range -4.11 to -11.76 kcal mol^{-1}. The C–H···Cl interaction in **3** exhibits a relatively weak E_{int} of -2.01 kcal mol^{-1} and the Cl···Cl interaction is very weak with E_{int} being close to 0 kcal mol^{-1}. The only π···π interactions among the series is only present in **4** and gives rise to a relatively strong E_{int} of -13.53 kcal mol^{-1}.

From the data in Table 5, it is evident the molecular packing of **1-4** is mainly stabilised by electrostatic forces owing to the strong O–H···O interactions which lead to the directional topology aligned along the *c*-axis for **1** and along *b*-axes for **2-4**, Fig. 11. The crystals also feature dispersive forces due to the other complementary contacts. The overall energy framework of **1** has a ladder-like topology in contrast to the zig-zag, sheet-like energy framework for **4**, while crystals **2** and **3** exhibit a similar, rack-shape topology consistent with their isostructural relationship. It is noteworthy some smaller repulsive forces are observed within the rack-shaped topology of **2** and **3** owing to the close proximity of the main electrostatic force resulting from the O–H···O interactions, the magnitude of which is inversely proportional to the distance of the point charges in accord with Coulomb's law.[79] Equivalent repulsive forces are not observed in **1** and **4**.

Table 5 Corrected interaction energies (kcal mol^{-1}) for all intermolecular close contacts present in **1** to **4**, with scale factors of 1.057, 0.740, 0.871 and 0.618 being applied for $E_{electrostatic}$, $E_{polarization}$, $E_{dispersion}$ and $E_{repulsion}$, respectively, as obtained from the CE-B3LYP/6-31G(*d*,*p*) model.[63]

Contact	$E_{electrostatic}$	$E_{polarization}$	$E_{dispersion}$	$E_{repulsion}$	E_{total}	Symmetry operation
1						
O1–H1o···O22	-16.27	-3.11	-2.04	9.34	-12.09	*x*, *y*, *z*
O21–H21o···O2	-17.36	-3.41	-3.73	9.85	-14.65	*x*, *y*, 1+*z*
C28–H28b···O1/ C9–H9a···π(C22–C27)/ C29–H29a···π(C2–C7)	-4.93	-1.15	-9.76	5.29	-10.56	1-*x*, 1-*y*, 1-*z*
C5–H5···O1	-1.59	-0.35	-3.56	1.40	-4.11	1½-*x*, ½+*y*, ½-*z*
C29–H29b··· π(C2–C7)	-4.85	-1.38	-6.08	4.56	-7.74	-½+*x*, ½-*y*, ½+*z*
C4–H4···S21	-1.67	-0.28	-1.73	1.46	-2.20	1½-*x*, ½+*y*, ½-*z*
C8–H8a···S21/ C10–H10a··· π(C22–C27)	-5.03	-0.94	-4.73	2.76	-7.93	-½+*x*, ½-*y*, -½+*z*

C21···O22	-5.48	-2.12	-8.97	4.80	-11.76	1-*x*, 1-*y*, 1-*z*
2						
O1–H1o···O2	-17.89	-3.71	-6.43	10.22	-17.81	-½-*x*, -½+*y*, 1½-*z*
C6–H6···O2/						
C4–H4···C10	-2.75	-0.90	-7.85	4.02	-7.48	½-*x*, -½+*y*, 1½-*z*
C10–H10b···π(C2–C7)	-2.73	-0.64	-4.91	3.31	-4.95	-½+*x*, ½-*y*, -½+*z*
C9–H9a···π(C2–C7)/						
C8–H8b···π(C2–C7)	-4.37	-1.49	-7.41	4.70	-8.58	-1+x, y, z
3						
O1–H1o···O2	-17.13	-3.91	-6.45	10.43	-17.09	-½-*x*, ½+*y*, ½-*z*

C6–H6···O2/						
C4–H4···C10	-4.95	-0.81	-7.97	4.67	-9.08	½-*x*, ½+*y*, ½-*z*
C10–H10a···π(C2–C7)	-1.52	-0.62	-4.98	3.03	-4.09	-½+*x*, 1½-*y*, -½+*z*
C9–H9b···π(C2–C7)/						
C8–H8a···π(C2–C7)	-2.85	-1.22	-6.85	3.97	-6.69	-1+*x*, *y*, *z*
C10–H10b···Cl1	-1.29	-0.16	-1.85	1.29	-2.01	-1½+*x*, 1½-*y*, -½+*z*
Cl1···Cl1	-0.13	-0.02	-0.73	0.83	-0.05	2-*x*, 1-*y*, 1-*z*
4						
O1–H1o···O22	-14.83	-4.00	-7.02	9.70	-16.13	*x*, 1+*y*, *z*
O21–H21o···O2	-14.45	-4.10	-7.22	9.59	-16.18	*x*, *y*, *z*
C29–H29b···O1	-0.43	-0.48	-3.98	2.60	-2.27	-*x*, 1-*y*, 1-*z*
C11–H11b···O3	-4.85	-0.78	-2.41	2.42	-5.62	*x*, *y*, 1+*z*

C7–H7···O23	-2.58	-0.46	-2.98	1.67	-4.35	*x*, 1+*y*, -1+*z*
C27–H27···O3	-2.78	-0.46	-3.02	1.67	-4.59	*x*, *y*, 1+*z*
C30–H30a··· π(C2–C7)/ C30–H30b···S1	-4.14	-0.88	-7.49	5.29	-7.24	1-*x*, 1-*y*, 1-*z*
C10–H10b··· π(C22–C27)/ C10–H10a···S21	-3.79	-0.83	-7.20	4.77	-7.07	1-*x*, 1-*y*, 2-*z*
C31–H31a···O23	-3.87	-0.62	-2.17	1.20	-5.47	*x*, *y*, -1+*z*
π(C22–C27)···π(C22–C27)	-6.24	-0.87	-10.89	4.46	-13.53	-*x*, -*y*, 2-*z*

View Article Online
DOI: 10.1039/D0CE01810D

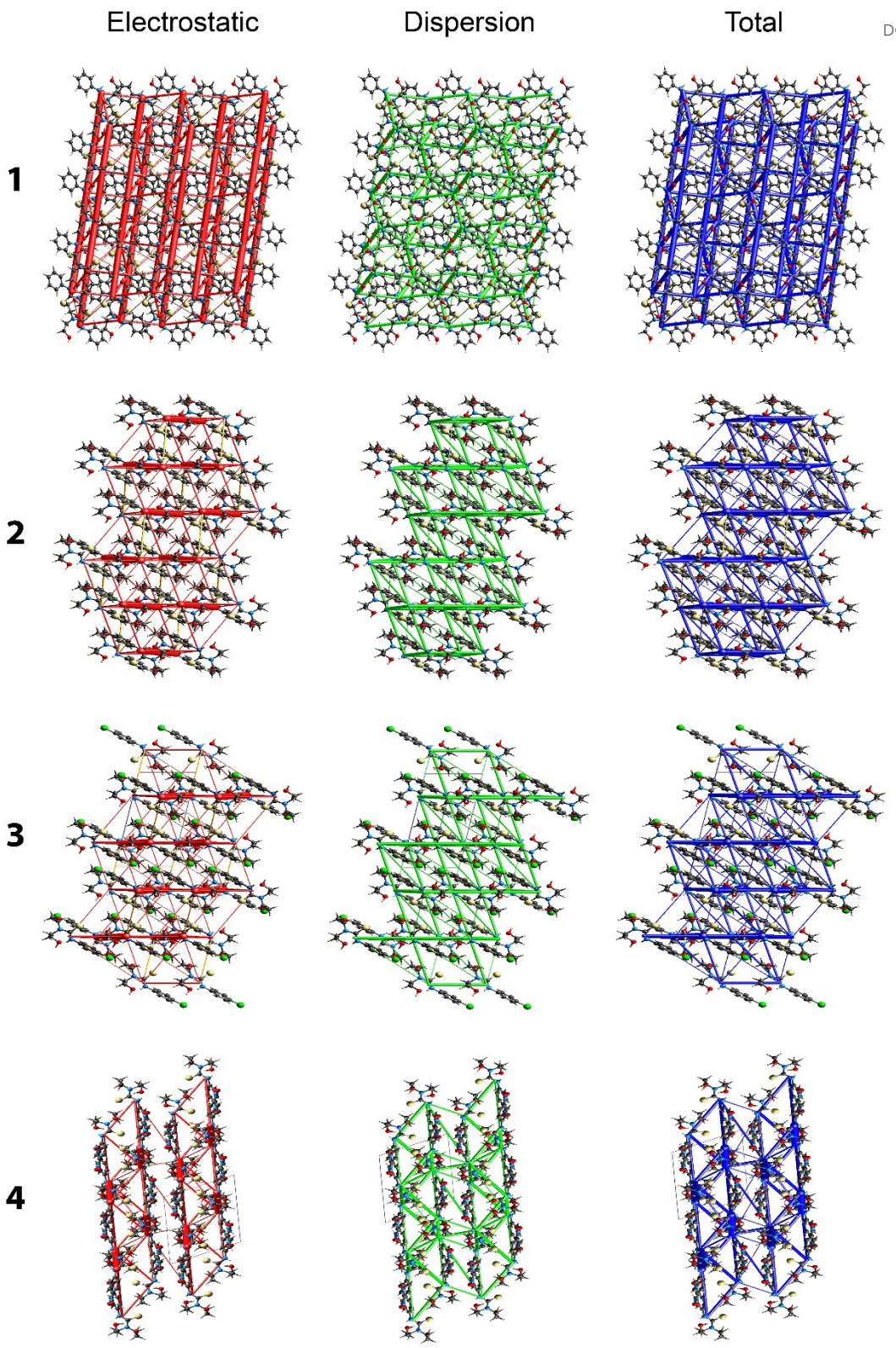

Fig. 11 Perspective views of the energy frameworks of **1**-**4** showing the (a) electrostatic force, (b) dispersion force and (c) total energy diagram. The cylindrical radius is proportional to the

View Article Online
DOI: 10.1039/D0CE01810D

relative strengths of the corresponding energies and were adjusted to the same scale factor of 100 with a cut-off value of 1.91 kcal mol^{-1} within 2 × 2 × 2 unit-cells.

Data in Table 6 indicate the calculated lattice energies follow the order of **2** (-25.70 kcal mol^{-1}) > **1** > **3** > **4** (-23.78 kcal mol^{-1}) with the range being about 2 kcal mol^{-1}. The order of the lattice energies correlates nicely with the relative greater contributions to the energies of stabilisation provided by the C–H···π(aryl) interactions through enhanced contributions which follow the same order. Further, the identified methylene-C–H···Cl(chloride) and aryl-C–H···O(nitro) interactions in **3** and **4**, respectively, exert little influence upon the lattice energies due to their weak nature. By contrast, the energy contribution from the π(aryl)···π(aryl) contact is **4** is significant.

Table 6 The lattice energy ($E_{lattice}$) in kcal mol^{-1} and the corresponding energy components ($E_{electrostatic}$, $E_{polarization}$, $E_{dispersion}$ and $E_{repulsion}$) calculated for a cluster of molecules within 25 Å from a reference molecule through the CE-B3LYP/6-31G(*d*,*p*) model.

Crystal	$E_{electrostatic}$	$E_{polarization}$	$E_{dispersion}$	$E_{repulsion}$	$E_{lattice}$
1	-16.19	-4.23	-16.70	12.29	-24.83
2	-14.72	-4.33	-19.30	12.65	-25.70
3	-14.77	-4.29	-18.62	13.06	-24.62
4	-15.01	-3.98	-16.82	12.03	-23.78

Non-covalent interaction (NCI) plots

Non-covalent interaction plots[58] were calculated for selected interactions identified in the crystals of **1-4** to verify the attractive nature of the interactions through visualisation a red-blue-green colour scheme on the iso-surface; red is indicative of a strong repulsive interaction, blue is indicative of a strong attractive interaction while green is indicative of a weak interaction.[80] The images of Fig. 12 reveal that the intermolecular hydroxyl-O–H···O(hydroxyl) interaction, common in all crystals, along with the intramolecular amide-N–H···O(hydroxyl) and hydroxyl-O–H···S(thione) contacts, are strong and attractive in nature with the low density, low reduced gradient trough for those interactions lying at the negative region at about -0.20 to -0.35 a.u. in the respective two-dimensional NCI plots.

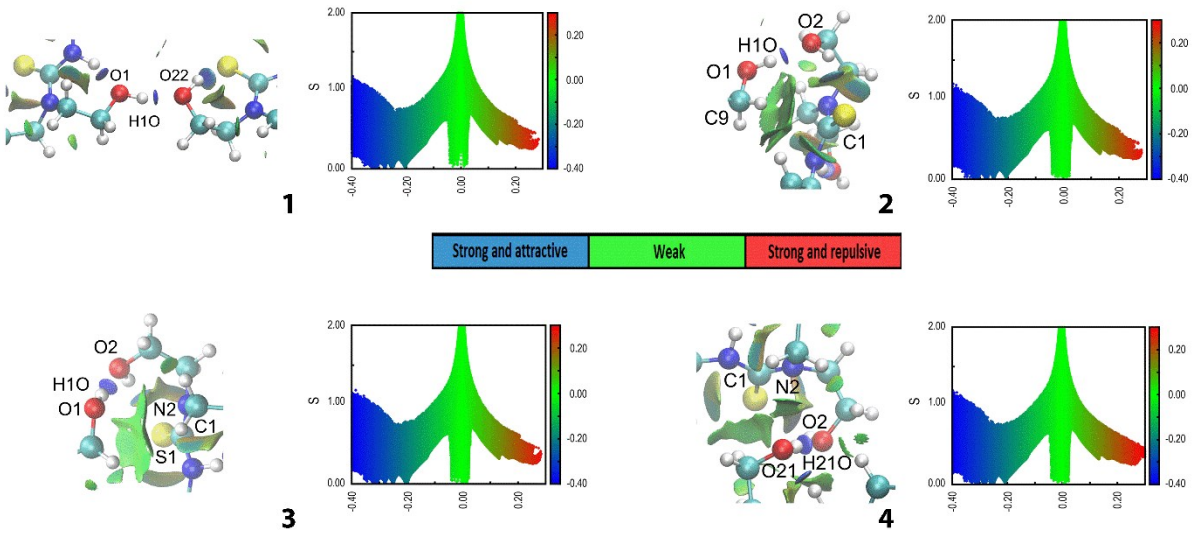

Fig. 12 NCI plots along with the two-dimensional plots of reduced density gradient (RDG) versus sign(λ^2)ρ(r) for the molecular dimers of **1-4** connected by hydroxyl-O–H···O(hydroxyl) hydrogen bonds and highlighting the intramolecular amide-N–H···O(hydroxyl) and hydroxyl-O–H···S(thione) hydrogen bonds. The gradient cut-off is set at 0.4 and the colour scale is -0.04 < ρ < 0.04 a.u. Non-essential atoms are truncated for clarity.

Interestingly, for pairs of molecules connected by hydroxyl-O–H···O(hydroxyl) hydrogen bonds in **2**-**4**, there are relatively large, diffuse green domains between the hydroxyethyl-H-and thione-S atoms (see ESI† Fig. S5) that serve to complement the hydrogen bonds; this confirmed in the corresponding QTAIM analysis[80] (see ESI† Fig. S6). The attractive interactions further strengthen the interactions leading to the supramolecular chains and are likely contributors to the reduction in their pitch.

In line with the Hirshfeld surface analysis, additional contacts are detected in **3**, *i.e.* methylene-C–H···Cl(aryl) and Cl···Cl, and **4**, *i.e.* methylene-C–H···O(nitro) and aryl-C–H···O(nitro), necessarily absent in **1** and **2**. As indicated from the light-green domains in the respective NCI plots of Fig. 13, these correspond to weak interactions. Other common interactions involving the aryl rings and methylene chains are considered weak and are evidenced through the high-density localised domains in the NCI plots of ESI† Fig. S5.

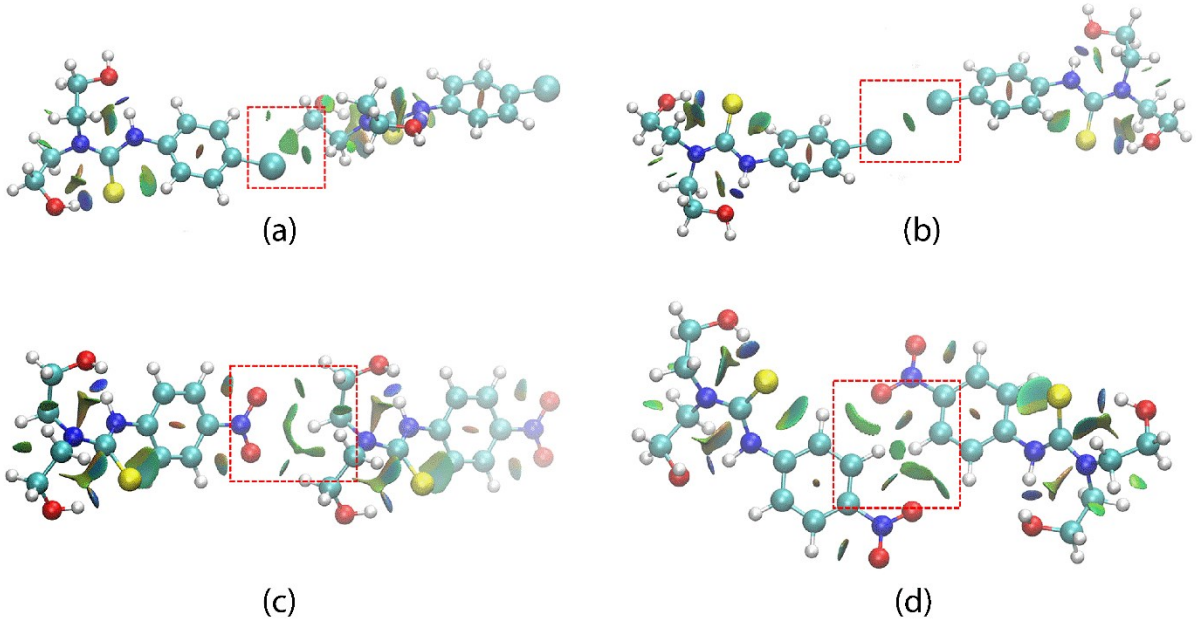

Fig. 13 NCI plots for the molecular dimers highlighting weak contacts in **3**: (a) methylene-C–H···Cl(aryl) and (b) Cl···Cl and **4**: (c) methylene-C–H···O(nitro) and (d) aryl-C–H···O(nitro).

Overview

Crystals of **1** comprise two independent molecules which associate to form a linear, supramolecular chain sustained, in part, by hydroxyl-O–H···O(hydroxyl) hydrogen bonds. In common with isostructural **2** and **3**, the space group of **1** is monoclinic, $P2_1/n$. There is a simple relationship between the crystals in that the unit-cell edge *a* in **2** and **3** is about half that of **1**, Table 1. Quite distinct crystal symmetry is noted for **4**, i.e. triclinic, $P\bar{1}$ with Z' = 2. Despite these differences, supramolecular chains featuring by hydroxyl-O–H···O(hydroxyl) hydrogen bonds are prominent in the crystals of **1**-**4**. However, unlike **1**, in the isostructural crystals of **2** and **3**, the chains have a helical topology. In **4**, zig-zag chains are apparent. In short, the topology of the supramolecular chains in **1**-**4** are syntactic with the crystalline environment in which they exist.[84]

Isostructural relationships are not uncommon for molecules differing in a chloro/methyl substituent, which have similar volumes, *i.e.* 19 Å^3 for chloride and 24 Å^3 for methyl.[82] Such cases of structural mimicry are commonly known as the chloro/methyl exchange,[83] but this concept can be expanded to include other substituents.[10] A chloro/methyl exchange in isostructural crystals implies similar influences upon the molecular packing by these substituents. This suggests the methylene-C–H···Cl(aryl) and Cl···Cl contacts noted in **3**, which occur in the inter-layer region, are not structure-directing even if weakly attractive. The methyl groups in **2**, which are also directed towards the inter-layer region, do not engage in directional interactions.

In terms of directional interactions, C–H···π(aryl) contacts feature in each crystal of **1**-**4**, and in **1**, lead to a three-dimensional architecture, in **2** and **3**, to a two-dimensional array and in **4**, to a double-layer. Further directional interactions are largely absent in **2** and **3**. By contrast, methylene-C–H···O(hydroxyl) and π(aryl)···π(aryl) interactions assemble the

double-layers in **4** (also stabilised by intra-layer methylene-C–H···O(nitro) contacts) into a three-dimensional arrangement.

At this stage it is salient to recall the results of the geometry optimisation calculations which indicate no significant influence is exerted by the methyl and chloro substituents in **2** and **3** but significant activation of the aryl ring owing to the electronegative nitro group in **4**. This latter observation correlates with the formation of the off-set π(aryl)···π(aryl) interactions observed in **4** but not in **1**-**3**.

An evaluation of the relative contributions of the different interaction energies to the overall energies of identified interactions reveals interesting trends. Thus, the energies (relative contributions) contributed by the hydroxyl-O–H···O(hydroxyl) hydrogen bonds are approximately -14.72 and -14.77 kcal mol^{-1} (46%) for **2** and **3**, -15.01 kcal mol^{-1} (40%) for **4** and -16.19 kcal mol^{-1} (38%) for **1**. This correlates with the repeat distances of the supramolecular chains with the greater energy contribution by hydroxyl-O–H···O(hydroxyl) hydrogen bonds to the overall energy of packing being associated with the chains with shortest repeat distances, *i.e*. **2** and **3** (10.77 Å) < **4** (11.21 Å) < **1** (16.47 Å).

While an exhaustive literature survey of this phenomenon is not feasible, as mentioned in the *Introduction*, a number of systematic studies have been described whereby the influence of small chemical changes upon supramolecular aggregation patterns investigated.[10-27] Except for an isostructural series[10] and universal adoption of the carboxylic dimer synthon in another series,[17] variations in the topology of the aggregate/chain/layer are the norm as small chemical changes are made to molecular formulae, even when comparable hydrogen bonds are evident. Such an observation confirms that in order to design a crystal let alone an aggregate within a crystal,[85] all supramolecular associations need to be taken in account.

Finally, it should be mentioned that during the course of these studies conducted over a period of well over five years in two different Institutions, involving repeated synthesis and crystallisations, no evidence for polymorphs or solvates was found. This is not to suggest that different crystalline forms are waiting to be discovered, in accord with the McCrone axiom.[86] However, it is stressed the experimental conformations in the crystals isolated in this study closely match the gas-phase optimised geometries suggesting the obtained crystals were the thermodynamic forms.

Conclusions

The crystal structure analyses along with detailed analyses of the supramolecular association in the crystals isolated for **1**-**4** show the formation of pervasive, hydrogen bonded chains that differ in topology: linear (**1**), helical (**2** and **3**) and zig-zag (**4**); no evidence for different crystalline forms was found in this study. In consideration of the (i) persistence of the hydroxyl-O–H···O(hydroxyl) hydrogen bonds leading to one-dimensional chains, (ii) the closeness of the calculated lattice energies, (iii) the relative importance of C–H···π(aryl) contacts operating normal to the chains and (iv) the, on average, more C–H···π(aryl) contacts formed per molecule in **1**, compared with **2**-**4**, it is concluded the different topologies of the supramolecular chains are related primarily to the influence of directional C–H···π(aryl) contacts. In **1**, where no other directional interactions are apparent, a more open, linear arrangement facilitates the formation of inter-chain C–H···π(aryl) interactions, by definition occupying a larger volume of space. In **2** and **3**, where C–H···π(aryl) interactions are less dominant, an observation traced to the Y = Me and Y = Cl substituents, helical chains are apparent. In **4**, where calculations indicate the aryl rings are activated, π(aryl)···π(aryl) interactions come to the fore and zig-zag chains are now apparent. Even if remote substituents

do not alter significantly the overall electronic structure of the molecules, their influence in participating in "second-tier" supramolecular association can direct the predominant mode of association between molecules leading to specific architectures.

In summary, the situation may be envisaged whereby the molecules precipitate from solution and align to form supramolecular chains *via* the predominant hydroxyl-O–H···O(hydroxyl) hydrogen bonds and the adopted topology is dictated by the need to optimise the supramolecular association between chains which, in turn, is moderated by the specific requirements of the remote substituents.

Author contributions

Sang Loon Tan: Data curation; Formal Analysis; Writing – original draft; Writing – review & editing

Edward R. T. Tiekink: Conceptualisation; Data curation; Formal Analysis; Funding acquisition; Writing – original draft; Writing – review & editing

Conflicts of interest

There are no conflicts to declare.

Acknowledgements

Nabihah Al Muna Mohd Nor is thanked for some preliminary experiments. The authors gratefully acknowledge Sunway University Sdn Bhd (Grant no. STR-RCTR-RCCM-001-2019) for support of crystallographic studies.

References

1. M. C. Etter, *Acc. Chem. Res*., 1990, **23**, 120–126.
2. G.A. Jeffrey, An Introduction to Hydrogen Bonding; Oxford University Press: New York, NY, USA, 1997.
3. T. Steiner, *Angew. Chem. Int. Ed.*, 2002, **41**, 48–76.
4. S. Scheiner, *Struct. Chem*., 2019, **30**, 1119–1128.
5. G. R. Desiraju, *Angew. Chem. Int. Ed. Engl.*, 1995, **34**, 2311–2317.
6. S. Scheiner, *J. Chem. Phys*., 2000, **153**, article no. 140901.
7. Q. Li and Z. Li, *Acc. Chem. Res*., 2020, **53**, 962–973.
8. A. P. Voronin, T. V. Volkova, A. B. Ilyukhin, A. N. Proshin and G. L. Perlovich, *CrystEngComm*, 2020, **22**, 349–360.
9. M. Kulułka, M. Srebo-Hooper and M. P. Mitoraj, *J. Phys. Chem. A*, 2020, **124**, 63–73.
10. A. Deya and G. R. Desiraju, *CrystEngComm*, 2004, **6**, 642–646.
11. D. Das and G. R. Desiraju, *CrystEngComm*, 2006, **8**, 674–679.
12. A. K. Jordaõ, V. F. Ferreira, A. C. Cunha, J. L. Wardell, S. M. S. V. Wardell and E. R. T. Tiekink, *CrystEngComm*, 2012, **14**, 6534–6539.
13. S. K. Seth, V. S. Lee, J. Yana, S. M. Zain, A. C. Cunha, V. F. Ferreira, A. K. Jordão, M. C. B. V. de Souza, S. M. S. V. Wardell, J. L. Wardell and E. R. T. Tiekink, *CrystEngComm*, 2015, **17**, 2255–2266.
14. L. Chęcińska, A. Jóźwiak, M. Ciechańska, C. Paulmann, J. J. Holstein, B. Dittrich and M. Małecka, *Z. Kristallogr. – Cryst. Mater.,* 2018, **233**, 675–687.
15. S. Y. Ho, R. P. A. Bettens, D. Dakternieks, A. Duthie and E. R. T. Tiekink, *CrystEngComm*, 2005, **7**, 682–689.
16. C. R. Kaiser, K. C. Pais, M. V. N. de Souza, J. L. Wardell, S. M. S. V. Wardell, and E. R. T. Tiekink, *CrystEngComm*, 2009, **11**, 1133–1140.

17. A. C. Cunha, V. F. Ferreira, A. K. Jordão, M. C. B. V. de Souza, S. M. S. V. Wardell, J. L. Wardell, P. A. Tan, R. P. A. Bettens, S. K. Seth and E. R. T. Tiekink, *CrystEngComm*, 2013, **15**, 4917–4929.

18. A. P. Voronin, T. V. Volkova, A. B. Ilyukhin, T. P. Trofimova and G. L. Perlovich, *CrystEngComm*, 2018, **20**, 3476–3489.

19. H. Andleeb, I. Khan, A. Franconetti, M. N. Tahir, J. Simpson, S. Hameed and A. Frontera, *CrystEngComm*, 2019, **21**, 1780–1793.

20. P. Mocilac and J. F. Gallagher, *CrystEngComm*, 2019, **21**, 4048–4062.

21. B. P. A. Gabriele, C. J. Williams, M. E. Lauer, B. Derby and A. J. Cruz-Cabeza, *Cryst. Growth Des*., 2020, **20**, 7516−7525.

22. C. Weck, E. Nauha and T. Gruber, *Cryst. Growth Des*., 2019, **19**, 2899–2911.

23. S. J. Pike, A. Heliot and C. C. Seaton, *CrystEngComm*, 2020, **22**, 5040–5048.

24. A. Dey, R. K. R. Jetti, R. Boese and G. R. Desiraju, *CrystEngComm*, 2003, **5**, 248–252.

25. M. D. L. Tonin, S. J. Garden, M. M. Jotani, J. L. Wardell and E. R. T. Tiekink, *Z. Kristallogr. – Cryst. Mater.,* 2019, **234**, 183–200.

26. F. Chen, Y. Wang, W. Zhang, T. Tian, B. Bai, H. Wang, F.-Q. Bai and M. Li, *Cryst. Growth Des*., 2019, **19**, 6100–6113.

27. H. Chung, S. Chen, B. Patel, G. Garbay, Y. H. Geerts and Y. Diao, *Cryst. Growth Des*., 2020, **20**, 1646–1654.

28. D. C. Schroeder, *Chem Rev*., 1955, **55**, 181–228.

29. J.-P. Griffiths, B. Maliha, M. G. Moloney, A. L. Thompson and I. Hussain, *Langmuir*, 2010, **26**, 14142–14153.

30. M. Banerjee, R. Karri, A. Chalana, R. Das, R. K. Rai, K. S. Rawat, B. Pathak and G. Roy, *Chem. – Eur. J*., 2017, **23**, 5696–5707.

31. S. M. Lee, A. H. S. Azizan and E. R. T. Tiekink, *Molbank*, 2018, **2018**, article no. M1035.

32. G. M. Viana, D. C. Soares, M. V. Santana, L. Henriques do Amaral, P. W. Meireles, R. P. Nunes, L. C. R. Pereira da Silva, L. C. de S. Aguiar, C. R. Rodrigues, V. Pereira de Sousa, H. C. Castro, P. A. Abreu, P. C. Sathler, E. M. Saraiva and L. M. Cabral, *Chem. Pharm. Bull*., 2017, **65**, 911–919.

33. Agilent Technologies, CrysAlisPro, Santa Clara, CA, USA, 2013.

34. G. M. Sheldrick, *Acta Crystallogr., Sect. A: Found. Crystallogr*., 2008, **64**, 112–122.

35. G. M. Sheldrick, *Acta Crystallogr*., *Sect. C: Struct. Chem*., 2015, **71**, 3–8.

36. L. J. Farrugia, *J. Appl. Crystallogr*., 2012, **45**, 849–854.

37. A. L. Spek, *Acta Crystallogr. Sect. E: Crystallogr. Commun*., 2020, **76**, 1–11.

38. K. Brandenburg, DIAMOND, Crystal Impact GbR, Bonn, Germany, 2006.

39. T. A. Halgren, *J. Comput. Chem*., 1996, **17**, 490–519.

40. Spartan'16, Wavefunction, Inc. Irvine, CA.

41. Y. Shao, L. F. Molnar, Y. Jung, J. Kussmann, C. Ochsenfeld, S. T. Brown, A. T. B. Gilbert, L. V. Slipchenko, S. V. Levchenko, D. P. O'Neill, R. A. DiStasio Jr., R. C. Lochan, T. Wang, G. J. O. Beran, N. A. Besley, J. M. Herbert, C. Y. Lin, T. Van Voorhis, S. H. Chien, A. Sodt, R. P. Steele, V. A. Rassolov, P. E. Maslen, P. P. Korambath, R. D. Adamson, B. Austin, J. Baker, E. F. C. Byrd, H. Dachsel, R. J. Doerksen, A. Dreuw, B. D. Dunietz, A. D. Dutoi, T. R. Furlani, S. R. Gwaltney, A. Heyden, S. Hirata, C.-P. Hsu, G. Kedziora, R. Z. Khalliulin, P. Klunzinger, A. M. Lee, M. S. Lee, W. Z. Liang, I. Lotan, N. Nair, B. Peters, E. I. Proynov, P. A. Pieniazek, Y. M. Rhee, J. Ritchie, E. Rosta, C. D. Sherrill, A. C. Simmonett, J. E. Subotnik, H. L. Woodcock III, W. Zhang, A. T. Bell, A. K. Chakraborty, D. M. Chipman, F. J. Keil, A.

Warshel, W. J. Hehre, H. F. Schaefer, J. Kong, A. I. Krylov, P. M. W. Gill and M. Head-Gordon, Phys. *Chem. Chem. Phys*., 2006, **8**, 3172–3191.

42. C. C. J. Roothaan, *Rev. Mod. Phys*., 1951, **23**, 69–89.
43. W. J. Pietro, M. M. Francl, W. J. Hehre, D. J. DeFrees, J. A. Pople and J. S. Binkley, *J. Am. Chem. Soc*., 1982, **104**, 5039–5048.
44. J. D. Chai and M. Head-Gordon, *Phys. Chem. Chem. Phys*., 2008, **10**, 6615–6620.
45. G. A. Petersson, A. Bennett, T. G. Tensfeldt, M. A. Al-Laham and W. A. Shirley, *J. Chem. Phys*., 1988, **89**, 2193–2218.
46. C. L. Andersen, C. S. Jensen, K. Mackeprang, L. Du, S. Jørgensen and H. G. Kjaergaard, *J. Phys. Chem. A*, 2014, **118**, 11074–11082.
47. A. D. McLean and G. S. Chandler, *J. Chem. Phys*., 1980, **72**, 5639–5648.
48. R. Krishnan, J. S. Binkley, R. Seeger and J. A. Pople, *J. Chem. Phys*., 1980, **72**, 650–654.
49. M. J. Frisch, G. W. Trucks, H. B. Schlegel, G. E. Scuseria, M. A. Robb, J. R. Cheeseman, G. Scalmani, V. Barone, B. Mennucci, G. A. Petersson, H. Nakatsuji, M. Caricato, X. Li, H. P. Hratchian, A. F. Izmaylov, J. Bloino, G. Zheng, J. L. Sonnenberg, M. Hada, M. Ehara, K. Toyota, R. Fukuda, J. Hasegawa, M. Ishida, T. Nakaji-ma, Y. Honda, O. Kitao, H. Nakai, T. Vreven, J. A. Montgomery, Jr., J. E. Peralta, F. Ogliaro, M. Bearpark, J. J. Heyd, E. Brothers, K. N. Kudin, V. N. Staroverov, R.Kobayashi, J. Normand, K. Raghavachari, A. Rendell, J. C. Burant, S. S. Iyengar, J. Tomasi, M. Cossi, N. Rega, J. M. Millam, M. Klene, J. E. Knox, J. B. Cross, V. Bakken, C. Adamo, J. Jaramillo, R. Gomperts, R. E. Stratmann, O. Yazyev, A. J. Austin, R. Cammi, C. Pomelli, J. W. Ochterski, R. L. Martin, K. Morokuma, V. G. Zakrzewski, G. A. Voth, P. Salvador, J. J. Dannenberg, S. Dapprich, A. D. Daniels, Ö. Farkas, J. B. Foresman, J.

V. Ortiz, J. Cioslowski and D. J. Fox, Gaussian 16, Gaussian, Inc., Wallingford CT, 2016.

50. F. Weigend and R. Ahlrichs, *Phys. Chem. Chem. Phys*., 2005, **7**, 3297–3305.
51. F. Weigend, *Phys. Chem. Chem. Phys*., 2006, **8**, 1057–1065.
52. J. L. Pascual-Ahuir, E. Silla and I. Tuñón, *J. Comp. Chem*., 1994, **15**, 1127-1138.
53. L. Li, T. Cai, Z. Wang, Z. Zhou, Y. Geng and T. Sun, *Spectrochim, Acta A Mol. Biomol. Spectrosc*., 2014, **120**, 106–118.
54. E. D. Glendening, A. E. Reed, J. E. Carpenter and F. Weinhold, NBO Version 3.1.
55. A. E. Reed, L. A. Curtiss and F. Weinhold, *Chem. Rev*., 1988, **88**, 899–926.
56. R. Dennington, T. A. Keith and J. M. Millam, GaussView, Version 6, Semichem Inc., Shawnee Mission, KS, 2016.
57. C. F. Macrae, I. Sovago, S. J. Cottrell, P. T. A. Galek, P. McCabe, E. Pidcock, M. Platings, G. P. Shields, J. S. Stevens, M. Towler and P. A. Wood, *J. Appl. Crystallogr.*, 2020, **53**, 226–235.
58. E. R. Johnson, S. Keinan, P. Mori-Sánchez, J. Contreras-García, A. J. Cohn and W. Yang, *J. Am. Chem. Soc*., 2010, **132**, 6498–6506.
59. W. Humphrey, A. Dalke and K. Schulten, *J. Mol. Graph*., 1996, **14**, 33–38.
60. S. K. Wolff, D. J. Grimwood, J. J. McKinnon, M. J. Turner, D. Jayatilaka and M. A. Spackman, *Crystal Explorer (Version 17)*, University of Western Australia, 2012.
61. S. L. Tan, M. M. Jotani and E. R. T. Tiekink, *Acta Crystallogr. Sect. E: Crystallogr. Commun*., 2019, **75**, 308–318.
62. M. A. Spackman and D. Jayatilaka, *CrystEngComm*, 2009, **11**, 19–32.
63. C. F. Mackenzie, P. R. Spackman, D. Jayatilaka and M. A. Spackman, *IUCrJ*, 2017, **4**, 575–587.

64. M. J. Turner, S. Grabowsky, D. Jayatilaka and M. A. Spackman, *J. Phys. Chem. Lett.*, 2014, **5**, 4249–4255.

65. S. P. Thomas, P. R. Spackman, D. Jayatilaka and M. A. Spackman, *J. Chem. Theory Comput*., 2018, **14**, 1614–1623.

66. L. Maschio, B. Civalleri, P. Ugliengo and A. Gavezzotti, *J. Phys. Chem. A*, 2011, **115**, 11179–11186.

67. I. J. Bruno, J. C. Cole, P. R. Edgington, M. Kessler, C. F. Macrae, P. McCabe, J. Pearson and R. Taylor, *Acta Crystallogr., Sect. B: Struct. Sci., Cryst. Eng. Mater*., 2002, **58**, 389–397.

68. K. R. Koch, C. Sacht and S. Bourne, *Inorg. Chim. Acta*, 1995, **232**, 109–115.

69. L. Hennig, K. Ayala-Leon, J. Angulo-Cornejo, R. Richter and L. Beyer, *J. Fluorine Chem*., 2009, **130**, 453–460.

70. S. L.Tan, A. H. S. Azizan, M. M. Jotani and E. R. T. Tiekink, *Acta Crystallogr., Sect. E: Cryst. Commun*., 2019, **75**, 1472–1478.

71. S. L.Tan, M. M. Jotani and E. R. T. Tiekink, *Acta Crystallogr., Sect. E: Cryst. Commun*., 2020, **76**, 155–161.

72. S. A. Bourne, O. Hallale and K. R. Koch, *Cryst. Growth Des*., 2005, **5**, 307–312.

73. P. Matczak, *Computation*, 2016, **4**, article no. 3.

74. L. Salvatella, *Educ. Quimica*, 2017, **28**, 232–237.

75. A. Torrisi, C. Mellot-Draznieks and R. G. Bell, *J. Chem. Phys*., 2009, **130**, article no. 194703.

76. V. Nikolova, D. Cheshmedzhieva, S. Ilieva and B. Galabov, *J. Org. Chem.*, 2019, **84**, 1908–1915.

77. S. L. Tan and E. R. T. Tiekink, *Acta Crystallogr., Sect. E: Cryst. Commun*., 2020, **76**, 102–110.

78. S. L. Tan and E. R. T. Tiekink, *Acta Crystallogr., Sect. E: Cryst. Commun.*, 2019, **75**, 1–7.

79. T. Heddle, in *Calculations in Fundamental Physics: Electricity and Magnetism*, eds R. Robinson and N. Hiller, Elsevier, Amsterdam, Vol. 2, 1971, 167–186.

80. J. Contreras-García, E. R. Johnson, S. Keinan, R. Chaudret, J-P. Piquemal, D. N. Beratan and W. Yang, *J. Chem. Theory Comput.,* 2011, **7**, 625–632.

80. T. Lu and F. Chen, *J. Comput. Chem*., 2011, **33**, 580–592.

82. G. R. Desiraju and J. A. R. P. Sarma, *Proc. Ind. Acad. Sci. (Chem. Sci.)*, 1986, **96**, 599–605.

83. M. R. Edwards, W. Jones, W. D. S. Motherwell and G. P. Shields, *Mol. Cryst. Liq. Cryst*. 2001, **356**, 337–353.

84. D. R. Smyth, B. R. Vincent and E. R. T. Tiekink, *Cryst. Growth Des*., 2001, **1**, 113–117.

85. E. R. T. Tiekink, *Chem. Commun*., 2014, **50**, 11079–11082.

86. J. Haleblian and W. McCrone, *J. Pharm. Sci*., 1969, **58**, 911–929.

View Article Online
DOI: 10.1039/D0CE01810D

Non-covalent interactions involving remote substituents influence the topologies of supramolecular chains featuring hydroxyl-O–H···O(hydroxyl) hydrogen bonding in crystals of $(HOCH_2CH_2)_2NC(=S)N(H)(C_6H_4Y\text{-}4)$ for Y = H, Me, Cl and NO_2

Sang Loon Tan and Edward R. T. Tiekink*

Research Centre for Crystalline Materials, School of Science and Technology, Sunway University, 47500 Bandar Sunway, Selangor Darul Ehsan, Malaysia

E-mail: edwardt@sunway.edu.my

ORCID iD: 0000-0002-5343-3382 (SLT); 0000-0003-1401-1520 (ERTT)

Abstract

Crystallography shows the universal adoption of supramolecular chains featuring by hydroxyl-O–H···O(hydroxyl) hydrogen bonding in crystals of $(HOCH_2CH_2)_2NC(=S)N(H)(C_6H_4Y\text{-}4)$ for Y = H, Me, Cl and NO_2. However, distinct topologies, *i.e*. linear (Y = H), helical (Y = Me and Cl) and zig-zag (Y = NO_2) are noted with major differences in the pitch of the polymer. Geometry-optimisation, MEP and NPA analyses shows a distinct electronic structure for the Y = NO_2 derivative, in particular relating to the activation of the aryl rings. An exhaustive analysis of the molecular packing (point-to-point interactions, crystal structure similarity, Hirshfeld surface analysis, NCI and QTAIM, interaction energies and energy frameworks) point to the importance

View Article Online
DOI: 10.1039/D0CE01810D

of C–H···π(aryl) interactions in stabilising the chains but these have a considerably reduced influence in the crystal with Y = NO_2, where π(aryl)···π(aryl) interactions are important. The more open arrangement for the linear chain in **1** facilitates the formation of C–H···π(aryl) interactions and the more compact arrangements enable the formation of stabilising, intra-chain methylene-C–H···S(thione) interactions. This study highlights the role of second-tier non-covalent interactions exert upon the arrangement of conventional hydrogen bonding interactions.

Footnote

† Electronic supplementary information (ESI) available: Crystallographic data, electrostatic potential charge deviations, NPA charges, HOMO-LUMO plots, PXRD patterns, molecular packing diagram, NCI and QTAIM plots. CCDC 2047050-2047053 contain the supplementary crystallographic data for this paper. For ESI and crystallographic data in CIF or other electronic format see DOI: 10.1039/d0cexxxxxx

View Article Online
DOI: 10.1039/D0CE01810D

Introduction

In the organic solid-state, conventional hydrogen bonding plays a privileged role in arranging molecules into supramolecular assemblies,[1-4] often by design employing the supramolecular synthon approach.[5] This prominent role notwithstanding, other intermolecular contacts come to the fore when conventional hydrogen bonding does not occur in three dimensions or is not present at all. Here, a myriad of alternative interactions come to the fore, such as π···π, C–H···π, lone-pair···π, chalcogen bonding, halogen bonding, *etc*.[6] Along with hydrogen bonding, many of these interactions provide similar energies of stabilisation in their crystals and being inherently weak are therefore, flexible, being subject to moderation by chemical substitution, steric effects, *etc*. The delineation of the role of these different modes of association is highly desirable in order to rationalise more fully the assembly of molecules in crystals as even small changes in molecular packing can influence macroscopic properties relating to, *e.g*. optoelectronic properties,[7] drug discovery[8] and the conformation of molecules.[9] Further, the control of flexible, cooperative supporting intermolecular interactions will lead to the strategic design of higher dimensional aggregation patterns in crystals featuring persistent, structure-directing hydrogen bonding patterns operating in zero-, one- or two-dimensions.

These aforementioned considerations increasingly motivate systematic studies of crystals featuring (i) a common hydrogen bonding aggregation pattern despite the presence of different substituents,[10-14] (ii) multiple hydrogen bonding options and their adoption related to small chemical changes[15-23] and (iii) no conventional hydrogen bonding present with studies conducted in order to ascertain the influence of other non-covalent interactions upon molecular aggregation.[24-27] Herein, an investigation related to scenario (i) is presented. As anticipated from the formula of the molecules investigated herein, *i.e*. $(HOCH_2CH_2)_2NC(=S)N(H)(C_6H_4Y\text{-}4)$ for Y

View Article Online
DOI: 10.1039/D0CE01810D

= H (**1**), Me (**2**), Cl (**3**) and NO_2 (**4**), Fig. 1, hydrogen bonding is prominent and a consistent adoption of supramolecular chains in the respective crystals is apparent, in each case mediated by hydroxyl-O–H···O(hydroxyl) interactions. However, the chains display distinct topologies, *i.e.* linear (**1**), helical (**2** and **3**) and zig-zag (**4**), and of the series, only **2** and **3** are isostructural.

Fig. 1 Chemical diagrams for the $(HOCH_2CH_2)_2NC(=S)N(H)(C_6H_4Y\text{-}4)$ molecules investigated herein.

Compounds **1**-**4** are examples of tri-substituted derivatives of thiourea, a well-known class of compound.[28] While crystal structures are known for derivatives conforming to the general formula $(HOCH_2CH_2)N(R)C(=S)N(H)R$,[29-31] for R = alkyl, aryl, none are known for the di-hydroxyethyl analogues, *i.e.* $(HOCH_2CH_2)_2NC(=S)N(H)R$. Indeed, with the exception of **1**,[32] which was investigated recently for anti-leishmanial activity, compounds **2**-**4** do not appear to have been reported previously. Herein, the synthesis, spectroscopic and crystallographic characterisation of **1**-**4** are described along with a detailed analysis of the molecular packing in their crystals with the aim of ascertaining the role of the Y = H, Me, Cl and NO_2 substituents upon the supramolecular association.

View Article Online
DOI: 10.1039/D0CE01810D

The objectives of the computational studies are three-fold, *i.e*. firstly, to validate whether the experimental structures represent the global minima through a conformational analysis, an analysis which has significant implications for their molecular packing. Secondly, to gain insight into the electronic nature of the molecules through molecular electrostatic potential (MEP) and natural population analysis (NPA) studies in order to ascertain any particular features in the electronic structures of the molecular that may impact upon the molecular packing. Finally, to qualitatively and quantitatively assess the molecular interactions present in each crystal through Hirshfeld surface analysis, interaction energy calculations, energy framework simulations, lattice energy calculation, non-covalent interaction plots as well as quantum theory of atoms in molecules (QTAIM). The aim of these studies is to correlate molecular conformation and electronic structure to determine and explain the main factors that influence the manner in which the thiourea derivatives pack in their crystals.

Experimental

Instrumentation

All chemicals and solvents were used as purchased without purification. The melting points (uncorrected) were measured using a Stuart SMP30 melting point apparatus. The IR spectra were measured on a Bruker Vertex 70v FT-IR spectrophotometer from 4000 to 80 cm^{-1}. ^{1}H and $^{13}C\{^{1}H\}$ NMR spectra were recorded in DMSO-d_6 solutions on a Bruker Ascend 400 MHz NMR spectrometer with chemical shifts relative to tetramethylsilane (TMS). The absorption spectra were measured on 100 μM acetonitrile solutions in the range 180-700 nm on a double-beam Shimadzu UV 3600 Plus UV-Vis spectrophotometer. The CHN elemental analyses were performed on a LECO TruSpec Micro analyser under a helium atmosphere with glycine being the

View Article Online
DOI: 10.1039/D0CE01810D

standard. The room temperature powder X-ray diffraction (PXRD) patterns were measured on a Rigaku MiniFlex 600 X-ray diffractometer with Cu Kα1 radiation (λ = 1.5418 Å) within a 2θ range of 5-70° and a step size of 0.02°. The comparisons between the experimental and calculated (from the respective CIF) PXRD patterns were performed with Rigaku's PDXL2 software (https://www.rigaku.com/en/products/software/pdxl/overview).

Synthesis

A common mode of synthesis was adopted for the preparation of 1,1-bis(2-hydroxyethyl)-3-phenylthiourea (**1**), 1,1-bis(2-hydroxyethyl)-3-(4-tolyl)thiourea (**2**) and 1,1-bis(2-hydroxyethyl)-3-(4-chlorophenyl)thiourea (**3**). Thus, 1 mmol of the corresponding aryl isothiocyanate (phenyl isothiocyanate (0.135 g); 4-tolyl isothiocyanate (0.149 g); 4-chlorophenyl isothiocyanate (0.169 g) all from Sigma) was reacted with an equimolar amount of diethanolamine (Sigma, 0.105 g) in ethanol (30 ml) followed by stirring for 3 h at room temperature. White precipitates were formed upon the addition of dichloromethane (3 ml). The products were filtered and subsequently washed with cold ethanol (2 ml). Recrystallisation in hot ethanol resulted in the formation of colourless blocks after slow evaporation. For 1,1-bis(2-hydroxyethyl)-3-(4-nitrophenyl)thiourea (**4**), the product was obtained by mixing diethanolamine (1 mmol, 0.105 g) in acetone (5 ml) with an equimolar amount of 4-nitrophenyl isothiocyanate (Acros, 0.180 g) which was pre-dissolved in acetone (30 ml). The mixture was then concentrated to half of the initial volume through slow evaporation with stirring at room temperature. Upon the formation of a yellow precipitate, the product was filtered and washed with a mixture of ethanol and ethyl acetate (4 ml, *v*/*v*). Yellow blocks were obtained through recrystallisation of the crude product in absolute ethanol under slow evaporation.

View Article Online
DOI: 10.1039/D0CE01810D

Characterisation

1: Colourless crystals, yield: 0.188 g (78%). M.pt.: 362.2-363.8 K. Calcd. for $C_{11}H_{16}N_2O_2S$: C 54.98, H 6.71, 11.66%. Found: C 55.01, H 6.79, N 11.38%. IR (ATR, cm^{-1}): 3247 (m) ν(O–H), 3145 (m) ν(N–H), 3093 (m) ν(C–H_{aro}), 3066-2845 (w) ν(C–H), 1312 (s) ν(C–N), 1033 (s) ν(C=S). ^{1}H NMR (DMSO-d_6, ppm): δ 9.72 (s, 1H, NH), 7.29 (m, 4H, *ortho*- and *meta*-phenyl-H), 7.08 (m, 1H, *para*-phenyl-H), 5.31 (br, 2H, OH), 3.84 (t, 4H, $^3J_{HH}$ = 5.3 Hz, CH_2–N), 3.73 (dt, 4H, $^3J_{HH}$ = 5.3 Hz, $^3J_{H\text{-}OH}$ = 4.6 Hz, CH_2–O). ^{13}C{^{1}H} NMR (DMSO-d_6, ppm): δ 182.23 (C=S), 141.34 (*ipso*-C), 128.52 (*ortho*-C), 124.71 (*meta*-C), 124.39 (*para*-C), 59.85 (C–O), 54.78 (C–N). UV/Vis (acetonitrile, 100 μM, nm, L mol^{-1} cm^{-1}): λ_{max}: 277 (sh), ε = 10964; 254, ε = 19953; 222 (sh), ε = 14791.

2: Colourless crystals, yield: 0.207 g (82%). M.pt.: 391.8-392.5 K. Calcd. For $C_{12}H_{18}N_2O_2S$: C 56.67, H 7.13, N 11.01%. Found: C 56.65, H 7.21, N 10.86%. IR (ATR, cm^{-1}): 3258 (m) ν(O–H), 3192 (m) ν(N–H), 3131 (m) ν(C–H_{aro}), 3057-2885 (w) ν(C–H), 1291 (s) ν(C–N), 1025 (s) ν(C=S). ^{1}H NMR (DMSO-d_6, ppm): δ 9.60 (s, 1H, NH), 7.18 (d, 2H, $^3J_{HH}$ = 8.36 Hz, *ortho*-aryl-H), 7.09 (d, 2H, $^3J_{HH}$ = 8.2 Hz, *meta*-aryl-H), 5.29 (br, 2H, OH), 3.83 (t, 4H, $^3J_{HH}$ = 5.36 Hz, CH_2–N), 3.72 (dt, 4H, $^3J_{HH}$ = 5.12 Hz, $^3J_{H\text{-}OH}$ = 4.8 Hz, CH_2–O), 3.06 (s, 3H, CH_3). ^{13}C{^{1}H} NMR (DMSO-d_6, ppm): δ 187.04 (C=S), 143.52 (*ipso*-C), 138.33 (*para*-C), 133.72 (*ortho*-C3), 129.70 (*meta*-C), 64.61 (C–O), 59.50 (C–N), 25.72 (methyl-C). UV/Vis (acetonitrile, 100 μM, nm, L mol^{-1} cm^{-1}): λ_{max}: 278 (sh), ε = 8318; 253, ε = 16218; 222 (sh), ε = 12589.

3: Colourless crystals, yield: 0.215 g (78%). M.pt.: 395.5-396.8 K. Calcd. For $C_{11}H_{15}ClN_2O_2S$: C 48.09, H 5.50, N 10.20%. Found: C 48.01, H 5.58, N 10.02%. IR (ATR, cm^{-1}): 3242 (w) ν(O–H),

View Article Online
DOI: 10.1039/D0CE01810D

3187 (w) ν(N–H), 3127 (w) ν(C–H_{aro}), 3042-2935 (w) ν(C–H), 1301 (s) ν(C–N), 1062 (s) ν(C=S), 691 (m) ν(C–Cl). ^{1}H NMR (DMSO-d_6, ppm): δ 9.76 (s, 1H, NH), 7.34 (s, 4H, *ortho*- and *meta*-aryl-H), 5.32 (br, 2H, OH), 3.85 (t, 4H, $^{3}J_{HH}$ = 5.2 Hz, CH_2–N), 3.73 (dt, 4H, $^{3}J_{HH}$ = 5.04 Hz, $^{3}J_{H\text{-}OH}$ = 4.84 Hz, CH_2–O). ^{13}C{^{1}H} NMR (DMSO-d_6, ppm): δ 186.84 (C=S), 145.06 (*ipso*-C), 133.14 (*ortho*-C), 133.01 (*para*-C), 131.07 (*meta*-C), 64.51 (C–O), 59.57 (C–N). UV/Vis (acetonitrile, 100 μM, nm, L mol^{-1} cm^{-1}): λ_{max}: 282 (sh), ε = 12023; 255, ε = 22909; 226 (sh), 13490.

4: Yellow crystals, yield: 0.224 g (79%). M.pt.: 449.4-450.8 K. Calcd. For $C_{11}H_{15}N_3O_4S$: C 46.31, H 5.30, N 14.73%. Found: C 46.34, H 5.36, N 14.44%. IR (ATR, cm^{-1}): 3259 (w) ν(O–H), 3224 (w) ν(N–H), 3075 (w) ν(C–H_{aro}), 3015-2832 (w) ν(C–H), 1505 (s) ν(N=O_{asym}), 1474 (s) ν(N=O_{sym}), 1291 (s) ν(C–N), 1027 (s) ν(C=S). ^{1}H NMR (DMSO-d_6, ppm): δ 10.37 (s, 1H, NH), 8.18 (d, 2H, $^{3}J_{HH}$ = 9.16 Hz, *meta*-aryl-H), 7.64 (d, 2H, $^{3}J_{HH}$ = 9.04 Hz, *ortho*-aryl-H), 5.82 (br, 1H, OH), 5.18 (br, 1H, OH), 3.88 (4H, t, $^{3}J_{HH}$ = 4.92 Hz, CH_2–N), 3.76 (4H, dt, $^{3}J_{HH}$ = 5.04 Hz, $^{3}J_{H\text{-}OH}$ = 5.16 Hz, CH_2–O). ^{13}C{^{1}H} NMR (DMSO-d_6, ppm): δ 181.50 (C=S), 147.87 (*para*-C), 142.38 (*ipso*-C), 124.59 (*meta*-C), 122.37 (*ortho*-C), 59.61 (C–O), 55.00 (C–N). UV/Vis (acetonitrile, 100 μM, nm, L mol^{-1} cm^{-1}): λ_{max}: 349, ε = 15488; 299 (sh), ε = 10715; 240, ε = 16982; 224 (sh), ε = 14454.

X-ray crystallography

The crystallographic and refinement data for **1-4** are given in Table 1. Intensity data were measured at 100 K on an Agilent Technologies SuperNova Dual diffractometer fitted with an Atlas detector. Data processing and Gaussian absorption corrections were accomplished with CrysAlis Pro.[33] Each structure was solved by direct methods[34] and the refinement was by full-matrix least squares on F^2 with anisotropic displacement parameters for all non-hydrogen atoms.[35] The C-

View Article Online
DOI: 10.1039/D0CE01810D

bound hydrogen atoms were placed on stereochemical grounds and refined with fixed geometries. The O-and N-bound hydrogen atoms were refined with O–H = 0.84±0.01 Å and N–H = 0.88±0.01 Å, respectively. A weighting scheme of the form $w = 1/[\sigma^2(F_o^2) + (0.037P)^2 + 1.248P]$, where $P = (F_o^2 + 2F_c^2)/3$, was introduced in each refinement. Owing to poor agreement, reflections, *i.e.* (1 3 0) for **1** and (-1 0 7) for **2**, were omitted from the final cycles of refinement. Finally, **4** was refined as two-component twin with the fraction due to the minor component = 0.142(3). The programs WinGX,[36] ORTEP-3 for Windows,[36] PLATON[37] and DIAMOND[38] were also used in the study.

Table 1 Crystallographic data and refinement details for **1**–**4**

Compound	**1**	**2**	**3**	**4**
Formula	$C_{11}H_{16}N_2O_2S$	$C_{12}H_{18}N_2O_2S$	$C_{11}H_{15}ClN_2O_2S$	$C_{11}H_{15}N_3O_4S$
Molecular weight	240.32	254.34	274.76	285.32
Crystal size/mm^3	0.30 × 0.30 × 0.30	0.05 × 0.05 × 0.15	0.05 × 0.05 × 0.15	0.30 × 0.35 × 0.40
Colour	colourless	colourless	colourless	yellow
Crystal system	monoclinic	monoclinic	monoclinic	triclinic
Space group	$P2_1/n$	$P2_1/n$	$P2_1/n$	$P\bar{1}$
a/Å	13.4885(1)	7.0472(2)	7.1366(2)	10.8235(5)
b/Å	11.1767(1)	10.7489(2)	10.7767(3)	11.2124(5)
c/Å	16.4909(2)	16.9533(4)	16.6259(4)	12.3443(5)
α/°	90	90	90	90.050(3)
β/°	98.544(1)	99.109(2)	100.221(2)	108.737(4)
γ,/°	90	90	90	114.559(4)
V/Å^3	2458.53(4)	1268.01(5)	1258.39(6)	1274.53(11)

Z	8	4	4	4
D_c/g cm^{-3}	1.299	1.332	1.450	1.487
μ/mm^{-1}	2.253	2.213	4.184	0.269
Measured data	9855	5049	4685	5859
Radiation	Cu Kα	Cu Kα	Cu Kα	Mo Kα
θ range/°	4.0 – 75.0	4.9 – 75.0	4.9 – 75.0	2.3 – 27.5
Unique data	4995	2586	2554	5859
Observed data ($I \geq 2.0\sigma(I)$)	4702	2346	2243	4753
No. parameters	307	164	163	362
R, obs. data; all data	0.030; 0.032	0.029; 0.033	0.031; 0.037	0.041; 0.054
a; b in weighting scheme	0.039; 0.851	0.033; 0.456	0.040; 0.220	0.056; 0.615
R_w, obs. data; all data	0.077; 0.078	0.071; 0.074	0.075; 0.080	0.104; 0.114
Range of residual electron density peaks/eÅ^{-3}	-0.30 – 0.29	-0.22 – 0.21	-0.31 – 0.24	-0.30 – 0.82

View Article Online
DOI: 10.1039/D0CE01810D

Computational studies

A conformational search was performed through a Monte Carlo algorithm using the Merck Molecular Force Field (MMFF),[39] as available in Spartan'16,[40,41] with the energy cut-off being set to 9.6 kcal mol^{-1}. To increase the accuracy on the Boltzmann distribution, the generated conformers were subjected to geometry optimisation using the *ab initio* HF/3-21G model[42,43] followed by energy calculations through the long-range corrected wB97XD density functional with Grimme's D2 dispersion model[44] coupled with Pople's 6-31G(*d*) basis set.[45] The long-range corrected hybrid model has been shown to greatly reduce self-interaction errors and give better accuracy in the interaction energies.[46] Upon elimination of redundant structures with minor conformational changes as well as those exceeding the 9.6 kcal mol^{-1} energy window, the remaining conformers were then submitted for further optimisation at the wB97XD/6-311+G(*d*,*p*) level.[47,48] At this stage, a frequency analysis was performed using the same level of theory and basis set to ensure the validity of the ground state structures. Finally, all identified conformers were submitted into Gaussian16[49] for optimisation using wB97XD with Ahlrichs's valence triple-zeta polarization basis sets (wB97XD/def2-TZVP)[50,51] and with the employment of the Polarisable Continuum Model by placing the solute in a cavity within an ethanol solvent reaction field through the integral equation formalism variant of polarisable continuum model (IEFPCM).[52] The Gibbs free energies were obtained through frequency calculations of the optimised structures at the same level of theory and basis set.

The relative population of each conformer was determined through a Boltzmann weighting factor using equation (**1**),[53] with ΔG_i being the Gibbs free energy of species *i* relative to the most stable conformer, *j* is the specific conformer (*j* = 1, 2, 3…), *R* is the gas constant and *T* is absolute temperature set to 298 K.

View Article Online
DOI: 10.1039/D0CE01810D

$$\text{Boltzmann weighting factor, } P_i = \frac{e^{-\Delta G_i/RT}}{\sum_{j=1} e^{-\Delta G_j/RT}} \times 100\% \qquad (1)$$

Several molecular properties were computed in an attempt to correlate the molecular packing in **1**-**4**. Briefly, the atomic charges for the corresponding optimised structures were obtained by natural population analysis (NPA)[54,55] using wB97XD/def2-TZVP. The electrostatic potential (ESP) was mapped onto the electron density iso-surfaces with constant electronic charge of 0.002 electrons/bohr^3 through the cubegen utility as available in GaussView6.[56] Further, a molecular packing analysis was performed using Mercury,[57] with the analysis criteria being set that only molecules within the 20% tolerance for both distances and angles were included in the calculation while molecules with a variation > 20% were discarded. Differences in the molecular structures (*i.e*. the substituents in the 4-position) and molecular inversions were allowed during the calculation.

For the qualitative evaluation on the strength of interactions, a non-covalent interaction (NCI) visualisation index was generated for the respective interacting dimers using *NCIPLOT*[58] through the plotting of the reduced density gradient as a function of the density across the molecules. The computed density derivatives were mapped as iso-surfaces which correspond to any favourable or unfavourable interactions as determined by the sign of the second density Hessian eigenvalue times the density and visualised using VMD Molecular Graphics Viewer.[59]

Hirshfeld surface mapping, the corresponding two-dimensional fingerprint plots as well as pairwise interaction calculation were generated using Crystal Explorer 17 (ref. 60) through an established method as reported previously,[61] with the experimental structures being used as the input with X–H bond lengths adjusted to their neutron-derived values.[62] The interaction energy calculations were performed using the dispersion corrected CE-B3LYP/6-31G(*d*,*p*) model as

View Article Online
DOI: 10.1039/D0CE01810D

available in the program, with the total intermolecular energy being the sum of energies of four main components, comprising electrostatic, polarisation, dispersion and exchange-repulsion with scale factors of 1.057, 0.740, 0.871 and 0.618, respectively.[63] The model was validated against the B3LYP-D2/6-31G(*d*,*p*) counterpoise corrected energy model as well as the benchmark CCSD(T)/ CBS model with considerable accuracy.[64] The energy frameworks for **1**-**4** were computed for a cluster of 2 × 2 × 2 unit cells with the energy cut-off being set to 1.9 kcal mol^{-1}. Finally, the total energy was obtained for a cluster of molecules within a 25 Å radius from a selected reference molecule through the same level of theory and basis set model. The lattice energy for the corresponding crystals were calculated using equation (2),[65] where the second term is the cell dipole energy correction, with ρ_{cell} being the vector sum of the molecular dipole moments, V_{cell} being the volume and Z being the number of formula units in the unit cell, respectively. Typically, the cell dipole energy correction is negligible (< 0.24 kcal/mol) for a unit cell with small dipole moment.[66]

$$E_{\text{lattice}} = \frac{1}{2}\sum_{R_{\text{AB}} < R} E_{\text{total}}^{\text{AB}} - \frac{2\pi\rho_{\text{cell}}^2}{3ZV_{\text{cell}}} \qquad (2)$$

For **1** and **4**, each with $Z' = 2$, the lattice energy was calculated as the average of lattice sums for each molecule in the asymmetric unit.

Results and Discussion

Synthesis and characterisation

The $(HOCH_2CH_2)_2NC(=S)N(H)(C_6H_4Y\text{-}4)$, Y = H (**1**), Me (**2**), Cl (**3**) and NO_2 (**4**), compounds have been prepared in good yield (78-82%) yield as colourless (**1**-**3**) and yellow (**4**) crystals. In

View Article Online
DOI: 10.1039/D0CE01810D

the IR spectra, characteristic bands in the regions 1291-1312 cm^{-1} and 1025-1062 cm^{-1} are assigned to υ(C–N) and υ(C=S), respectively. In the ^{1}H NMR spectra, measured in DMSO-d_6 solution, the expected resonances and integration, including for the N–H and O–H protons, were noted. In the $^{13}C\{^{1}H\}$ NMR spectra, resonances due to the quaternary-C1 atom were seen downfield, in the range 181.50 (**4**) to 187.04 ppm (**2**). In order to assign the transitions in the UV spectra, an analysis on the HOMO-LUMO profile was performed for the lowest energy conformer at the ground state (*vide infra*) for each of **1**-**4**; see ESI† Fig. S1. This revealed the HOMO is located at the C1=S1 chromophore for **1**-**3**, while the LUMO, LUMO(+1) and LUMO(+2) are located at the delocalised C1=N1/C1=N2, C2=C3 and C4=C5/C6=C7 chromophores, respectively, which indicates that the experimental UV absorption bands at approximately 280, 250 and 220 nm can be attributed to n → π*, π → π* and π → π* transitions, respectively. As for **4**, the delocalised chromophore associated with the nitro group contributes to LUMO(+1) and hence, the additional absorption band at approximately 350 nm can be assigned to π → π*. The PXRD pattern measured for each of **1**-**4** closely match the simulated pattern calculated from their single crystal data, confirming the phase similarity between the respective bulk materials (293 K) and experimental structures (100 K); see ESI† Fig. S2.

Experimental molecular structures

Crystal structures were established for **1**-**4**; for each of **1** and **4**, two independent molecules comprise the asymmetric unit, henceforth **1a** & **1b** and **4a** & **4b**, respectively. The molecular structures are shown in Fig. 2 and selected geometric data are collated in Table 2. The first independent molecule of **1**, Fig. 2(a), features a planar C1,N1,N2,S1 chromophore which exhibits a r.m.s. deviation of 0.0038 Å for the fitted atoms. The mono-substituted amine-N1 atom carries

View Article Online
DOI: 10.1039/D0CE01810D

a phenyl ring and the di-substituted amine-N2 atom carries two hydroxyethyl groups. A significant twist in the molecule is apparent with the dihedral angle between the central plane and appended phenyl ring being 59.39(4)°. This observation plus that the two methylene-C atoms bound to the N2 atom suggests there is not extensive delocalisation of π-electron density over the molecule; the C1–N bond lengths are experimentally equivalent. Consistent with the presence of the C1=S1 double bond at the C1 atom, the angles subtended at the N2 atom involving the C1 atom are the widest. However, the widest angle at a nitrogen atom is the C1–N1–C2 angle which reflects the presence of the amine-H atom. A similar distortion in angles is seen about the C1 atom. Rather than being "dangling", the hydroxyl groups are orientated towards the rest of the molecule enabling the formation of intramolecular hydroxyl-O–H···S(thione) and amine-N–H···O(hydroxyl) hydrogen bonds and *S*(7) loops, as detailed in Table 3. As seen from Table 2, the key bond lengths and angle defining the independent molecules of **1**, Fig. 2(b), are generally close with the most significant difference being a wider angle by about 3° for C1–N1–C2 in the second molecule. Greater differences are noted in torsion angles, Table 2. The maximum difference of approximately 20° is noted in the C1–N1–C2–C3 torsion angles followed by approximately 10° for the N2–C8–C9–O1 torsion angles. A difference of approximately 20° is also seen in the CN_2S/aryl torsion angles with reduced splaying between the planes noted in the second molecule of **1**.

Very similar molecular conformations are noted for **2**-**4**, Figs 2(c)-(f) and Table 2, including the formation of the intramolecular hydrogen bonds, Table 3. The most notable differences between **1** and each of **2**-**4** relate to the more planar S1–C1–N1–C2 torsion angles and to the reduced N2–C10–C11–O2 torsion angles, by up to 18°, in **2**-**4**. Two independent molecules comprise the asymmetric unit of **4** but each presents very similar geometric parameters, Table 2.

View Article Online
DOI: 10.1039/D0CE01810D

However, a distinguishing feature of the two molecules comprising **4** and each of **1**-**3** relates to an apparent disparity in the C1–N1 and C1–N2 bond lengths in **4** not seen in the latter; this observation is discussed further below. An overlay diagram of the experimental molecular structures is shown in Fig. 2(g) from which it is plain that significant conformational differences with respect to the relative orientations of both the hydroxyethyl and aryl groups are evident across the series.

Fig. 2. Molecular structures of (a) **1** (first independent molecule), (b) **1** (second molecule), (c) **2**, (d) **3**, (e) **4** (first independent molecule) and (f) **4** (second independent molecule), all showing atom labelling schemes and displacement ellipsoids at the 50% probability level. Overlap diagrams of the (g) experimental and (h) geometry optimised structures – the molecules have been overlapped so that the central N_2S residues are coincident. Colour code: **1** (first independent molecule), red; **1** (second independent molecule), green; **2** (inverted), blue; **3**, cyan; **4** (first independent molecule), pink; **4** (inverted second independent molecule), yellow.

Table 2 Selected experimental and calculated (in italics) geometric data (Å, º) characterising **1-4**

Parameter	**1a**	**1b**	**2**	**3**	**4a**	**4b**
C1–S1	1.7028(12)	1.6985(12)	1.6986(13)	1.6968(16)	1.6900(18)	1.6893(18)
	1.695		*1.696*	*1.694*	*1.690*	
C1–N1	1.3518(16)	1.3511(15)	1.3573(16)	1.360(2)	1.375(2)	1.374(2)
	1.370		*1.368*	*1.372*	*1.380*	
C1–N2	1.3499(15)	1.3544(15)	1.3539(16)	1.354(2)	1.344(2)	1.345(2)
	1.376		*1.376*	*1.375*	*1.372*	
C1–N1–C2	127.40(11)	130.19(10)	127.08(11)	126.00(14)	128.13(15)	128.95(15)
	128.4		*128.1*	*128.3*	*129.8*	
C1–N2–C8	122.75(10)	122.65(10)	123.22(10)	123.07(13)	123.67(15)	123.44(15)
	122.9		*122.8*	*122.9*	*123.1*	
C1–N2–C10	122.86(10)	122.59(10)	121.49(11)	121.54(13)	121.06(15)	121.47(15)

	120.9		*120.9*	*120.8*	*120.8*	
C8–N2–C10	114.35(9)	114.70(9)	115.29(10)	115.39(12)	115.27(14)	115.08(14)
	115.8		*115.8*	*115.8*	*115.7*	
S1–C1–N1	122.32(9)	123.78(9)	122.78(10)	122.52(12)	122.81(14)	123.14(14)
	123.3		*123.2*	*123.2*	*123.3*	
S1–C1–N2	122.68(9)	121.91(9)	122.69(9)	122.83(12)	123.09(14)	123.10(13)
	122.9		*122.9*	*123.0*	*123.3*	
N1–C1–N2	114.99(10)	114.29(10)	114.52(11)	114.64(14)	114.09(15)	113.74(15)
	113.8		*113.9*	*113.8*	*113.4*	
S1–C1–N1–C2	14.67(18)	13.32(18)	4.79(19)	-5.3(2)	3.9(3)	-5.8(3)
	13.9		*13.2*	*-13.8*	*-19.0*	
C1–N1–C2–C3	51.55(19)	31.80(19)	53.74(19)	-55.6(2)	42.1(3)	-39.5(3)
	44.0		*46.3*	*-43.5*	*-30.8*	
S1–C1–N2–C8	-165.08(9)	-160.46(9)	-166.78(9)	166.73(12)	-166.45(13)	165.12(13)

	-158.3		*-158.1*	*158.6*	*159.8*	
S1–C1–N2–C10	17.34(16)	16.56(16)	13.32(16)	-13.6(2)	13.9(2)	-16.0(2)
	13.1		*13.3*	*-12.8*	*-12.0*	
N2–C8–C9–O1	73.33(12)	82.80(13)	71.13(14)	-71.15(17)	61.7(2)	-63.9(2)
	72.1		*72.3*	*-72.0*		*-71.2*
N2–C10–C11–O2	74.54(13)	73.76(13)	59.47(14)	-58.80(18)	52.5(2)	-55.1(2)
	49.8		*50.0*	*-49.4*	*-48.7*	
r.m.s. deviation CN_2S	0.0038	0.0065	0.0027	0.0036	0.0048	0.0043
CN_2S/aryl	59.39(4)	39.07(4)	54.3(5)	56.98(6)	42.70(7)	41.33(8)
	51.6		*53.2*	*51.0*	*43.4*	

Table 3 Summary of intra- and inter-molecular interactions (A–H···B; Å, º) operating in the crystals of **1-4**

A	H	B	A–H	H···B	A···B	A–H···B	Symmetry operation
1							
N1	H1n	O1	0.873(14)	1.914(14)	2.7514(15)	160.1(15)	*x*, *y*, *z*
O2	H2o	S1	0.841(14)	2.269(15)	3.1009(9)	170.1(13)	*x*, *y*, *z*
N21	H21n	O21	0.872(13)	1.900(14)	2.7624(14)	169.4(13)	*x*, *y*, *z*
O22	H22o	S21	0.838(14)	2.323(15)	3.1470(9)	167.6(14)	*x*, *y*, *z*
O1	H1o	O22	0.839(11)	1.841(11)	2.6753(13)	173.0(17)	*x*, *y*, *z*
O21	H21o	O2	0.842(16)	1.842(16)	2.6825(14)	176.1(15)	*x*, *y*, 1+*z*
C9	H9a	Cg(C22-C27)	0.99	2.68	3.6030(13)	155	1-*x*, 1-*y*, 1-*z*
C9	H9b	Cg(C22-C27)	0.99	2.78	3.6822(13)	151	-½+x, ½-y, - ½+z
C29	H29b	Cg(C2-C7)	0.99	2.95	3.8131(14)	147	1-*x*, 1-*y*, 1-*z*
2							
N1	H1n	O1	0.875(14)	1.906(13)	2.7449(16)	160.1(14)	*x*, *y*, *z*
O2	H2o	S1	0.839(12)	2.367(15)	3.1500(10)	155.4(16)	*x*, *y*, *z*
O1	H1o	O2	0.837(15)	1.882(16)	2.7137(14)	172.0(19)	-½-*x*, -½+*y*, 1½-*z*

C8	H8a	Cg(C2-C7)	0.99	2.89	3.4957(13)	120	-1+*x*, *y*, *z*
C10	H10b	C6	0.99	2.73	3.6263(19)	150	-½+*x*, ½-*y*, -½+*z*
3							
N1	H1n	O1	0.881(18)	1.907(18)	2.7453(19)	158.3(17)	*x*, *y*, *z*
O2	H2o	S1	0.828(13)	2.388(16)	3.1591(13)	155.2(18)	*x*, *y*, *z*
O1	H1o	O2	0.837(17)	1.879(17)	2.7156(18)	178(2)	-½-*x*, ½+*y*, ½-*z*
C8	H8a	Cg(C2-C7)	0.99	2.95	3.5488(17)	120	-1+*x*, *y*, *z*
C10	H10b	Cl1	0.99	2.85	3.6738(14)	141	-1½+*x*, 1½-*y*, -½+*z*
C5	Cl1	Cl1	1.7448(17)	3.4432(6)	–	154.00(6)	2-*x*, 1-*y*, 1-*z*
4							
N1	H1n	O1	0.88(2)	2.03(2)	2.842(2)	153(2)	*x*, *y*, *z*
O2	H2o	S1	0.84(3)	2.40(2)	3.1671(16)	152(3)	*x*, *y*, *z*
N21	H21n	O21	0.88(2)	2.02(2)	2.839(2)	154(2)	*x*, *y*, *z*
O22	H22o	S21	0.839(14)	2.41(2)	3.1767(16)	152(3)	*x*, *y*, *z*
O1	H1o	O22	0.838(19)	1.890(19)	2.723(2)	173(2)	*x*, 1+*y*, *z*
O21	H21o	O2	0.83(2)	1.90(2)	2.732(2)	172.7(19)	*x*, *y*, *z*
C29	H29b	O1	0.99	2.39	3.375(3)	175	-*x*, 1-*y*, 1-*z*

C11	H11b	O3	0.99	2.39	3.360(3)	165	*x*, *y*, 1+*z*
C10	H10b	Cg(C22-C27)	0.99	2.72	3.475(2)	133	1-*x*, 1-*y*, 2-*z*
C9	H9b	Cg(C2-C7)	0.99	2.71	3.483(2)	135	1-*x*, 1-*y*, 1-*z*
Cg(C22-C27)		Cg(C22-C27)	–	–	3.6105(12)	0	-*x*, -*y*, 2-*z*

Molecular packing

The geometric parameters characterising the specific intermolecular contacts operating in the crystals of **1**-**4** are collated in Table 3. The common feature of the supramolecular aggregation is the formation of supramolecular chains mediated by hydroxyl-O–H···O(hydroxyl) hydrogen bonding. However, the topologies of the resultant chains are distinct. In **1**, the two similarly orientated molecules comprising the asymmetric unit are connected by a single hydroxyl-O–H···O(hydroxyl) hydrogen bond and the resultant two-molecule aggregates are connected into a linear supramolecular chain parallel to the *c*-axis in the crystal with monoclinic space group $P2_1/n$. In isostructural **2** and **3**, helical chains are formed, being propagated by 2_1-screw symmetry along the *b*-axis in monoclinic space group $P2_1/n$, in their crystals. In **4**, the independent molecules are connected into a V-shaped aggregate which are connected to translationally related aggregates to form a zig-zag chain along the *b*-axis in the triclinic ($P\bar{1}$) crystal. The side- and end-on views of the supramolecular chains are illustrated for **1**, **2** and **4** in Fig. 3, and for **3** in ESI† Fig. S3. The differences in the topologies is reflected in the distances between translationally related pairs of molecules, *i.e.* 16.49, 10.75, 10.77 and 11.21 Å, respectively, indicating more open arrangements in the sequence **1** > **4** > **3** and **2**.

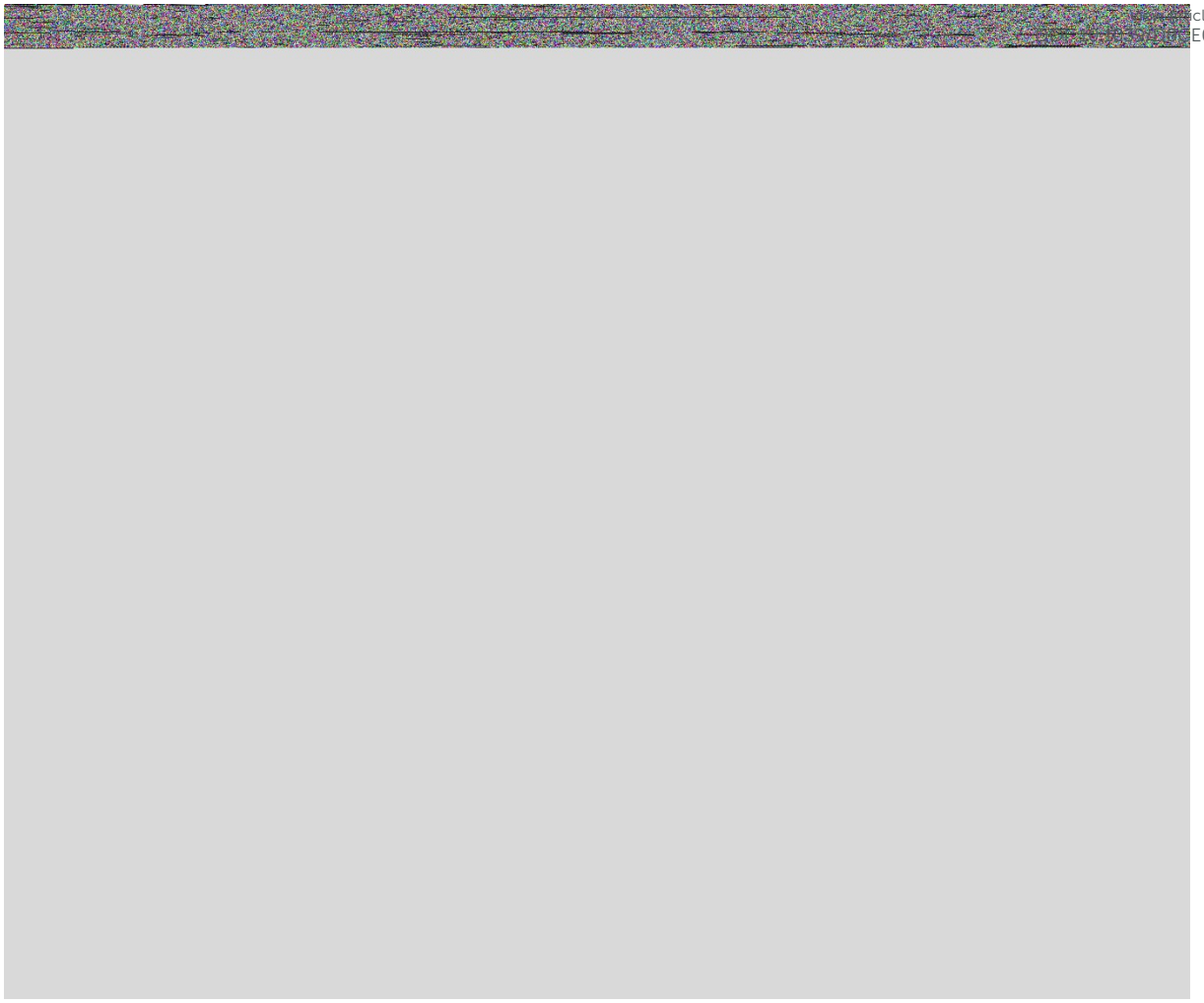

Fig. 3. Side- and end-on views of the supramolecular chains featuring by hydroxyl-O–H···O(hydroxyl) hydrogen bonding, shown as orange dashed lines, in the crystals of (a) **1**, (b) **2** and (c) **4**.

In **1**, the only other identifiable points of contact between the supramolecular chains are methylene-C–H···π(aryl) interactions, with the C22-C27 ring accepting two interactions to either side, and these serve to assemble the chains into a three-dimensional architecture, Fig. 4(a).

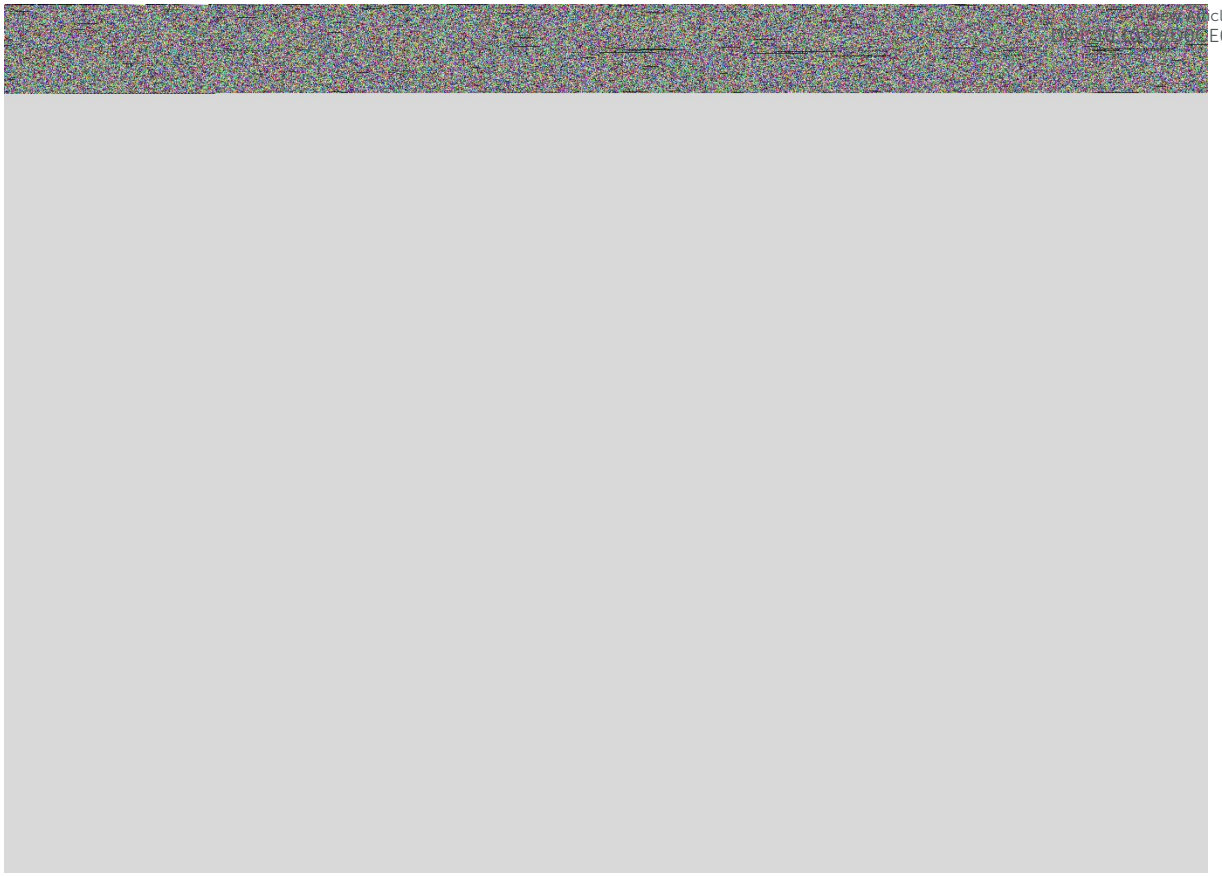

Fig. 4. Unit-cell contents for (a) **1**, viewed down the *c*-axis, (b) **2**, viewed down the *b*-axis, (c) **3**, viewed down the *a*-axis and (d) **4**, viewed down the *b*-axis; the views in (a), (b) and (d) are in projection down the axes of propagation of the chains. The hydroxyl-O–H···O(hydroxyl), methylene-C–H···π(aryl), methylene-C–H···C(aryl), methylene-C–H···Cl, Cl···Cl, methylene-C–H···O(hydroxyl, nitro) and π(aryl)···π(aryl) interactions are shown as orange, purple, pink, dark-red, cyan, blue and dark-green dashed lines, respectively.

In the crystal of **2**, the chains are connected into a two-dimensional array in the *ab*-plane by methylene-C–H···π(C2-C7) interactions. The layers stack along the *c*-axis with the closest interaction between them being a methylene-C–H···C(aryl) contact, Table 3. A view of the unit-cell contents for isostructural **3** is shown in Fig. 4(c). Here, there is evidence for weak inter-layer methylene-C–H···Cl and Cl···Cl contacts, Table 3. A distinct molecular packing is

View Article Online
DOI: 10.1039/D0CE01810D

noted in the crystal of **4** primarily owing to the participation of hydroxyl- and nitro-O atoms along with face-to-face π···π contacts, Table 3. Thus, the methylene-C–H···π(aryl) contacts, present in all crystals connect chains into a centrosymmetric double-layer in the *bc*-plane, within which are supporting methylene-C–H···O(nitro) contacts. The double-layers stack along the *a*-axis with methylene-C–H···O(hydroxyl) and π(aryl)···π(aryl) contacts assembling the layers into a three-dimensional architecture, Fig. 4(d). The π(aryl)···π(aryl) contacts occur between centrosymmetrically related residues and the rings are off-set to optimise the attraction: the inter-plane separation is 3.4128(8) Å and the slippage is 1.18 Å.

Molecular packing similarity analysis

A packing similarity analysis was performed between **1**-**4** to identify any similarities in the molecular arrangements in their crystals.[57] The results show that the packing in **1** is quite distinct to that of **2**, **3** and **4**, with only one molecule out of 15 falling within the 20% tolerance in both distance and angle deviations. The r.m.s. deviation between **1** & **2**, **1** & **3** and **1** & **4** amounts to 0.946, 0.931 and 0.934 Å, respectively. The major deviation arises as in the crystal of **1**, the molecules are mainly connected through hydroxyl-O–H···O(hydroxyl) interactions in a linear arrangement, while in each of **2**-**4**, the molecules are connected by the same interaction but arranged in a helix (**2** and **3**) and a zig-zag chain (**4**), as highlighted in the overlay diagrams for **1** & **2** and **1** & **4** of Figs 5(a) and (b), respectively. For comparison, Fig. 5(c) shows the equivalent image for isostructural **2** and **3** where the r.m.s. deviation is 0.173 Å. An intermediate situation when **2** (and **3**) is compared with **4**, Fig. 5(d), where the r.m.s. deviation is 0.388 Å; the r.m.s. deviation between **3** and **4** is 0.461 Å. A closer inspection of the supramolecular chains of **2** and **4**, Fig. 5(e), shows every second molecule of **2** has an alternate

orientation, reflecting the 2_1-screw symmetry, compared with the molecules having the same relative orientation reflecting the pseudo-mirror symmetry of the zig-zag chain of **4**.

Fig. 5 Comparisons of the molecular packing leading to the supramolecular chains (only four molecules of each are shown) between (a) **1** (blue) and **2** (green), (b) **1** and **4** (red), (c) **2** and **3** (magenta), (d) **2** and **4** and (e) end-on view of **2** and **4** with the differently-orientated hydroxyl-O–H···O(hydroxyl) interactions. In (a)-(e), best-fitting molecules are highlighted in ball and stick representation.

Conformational analysis

Owing to the presence of the hydroxyethyl moieties in **1-4**, which may participate in various intra- and inter-molecular interactions depending on the conformations they adopt, a detailed conformational analysis of a representative molecule, namely **4**, was conducted to assess whether the observed experimental structure represents a conformation at or close to the global minimum on the potential energy surface. A striking feature of the molecular structures of **1-4** was the universal formation of intramolecular hydroxyl-O–H···S(thione) and amine-N–H···O(hydroxyl) hydrogen bonds, Fig. 2 and Table 3. The (any atom)N(H)C(=S)N($CH_2CH_2OH)_2$ fragment is relatively rare in the crystallographic literature,[67] being restricted to a small number of ArC(=O)N(H)C(=S)N($CH_2CH_2OH)_2$ molecules[68-71] and a bi-functional analogue.[72] A common feature of the literature precedents is the formation of the intramolecular amine-N–H···O(hydroxyl) hydrogen bonds but no analogous intramolecular hydroxyl-O–H···S(thione) interactions as in **1-4**. Given this observation, it was thought of interest to ascertain whether the orientations of the flexible hydroxyethyl residues in **1-4** corresponded to the global potential energy minima. Accordingly, a conformational analysis through a series of optimisation steps (see *Experimental*) was performed on a representative molecule, namely, **4**. In all, nine conformers with lowest energy were identified upon consecutive elimination of the redundant conformers and those with the relative energy exceeding 9.6 kcal mol^{-1} throughout the series of optimisation steps. As validated through the vibrational analysis with zero imaginary frequency, final optimisation showed that all nine conformers were either true local minima or the global minimum structure on the potential energy surface. The chemical diagrams for the identified conformers together with the energy details are presented in Fig. 6. Clearly, among all possible conformations identified for **4**, conformer **4-1** is the global minimum structure with the lowest Gibbs free energy and is also the most dominant conformer with the highest relative population of about 82%. Two other conformers lie within 2 kcal mol^{-1}, namely **4-2** and **4-3**, with Boltzmann populations of 10.45

and 3.52%, respectively. Clearly, the intramolecular hydrogen bonds play a crucial role in stabilising the observed molecular conformation, by about 1-5 kcal mol^{-1} compared to the conformation without intramolecular hydrogen bonding, *i.e.* **4-9**.

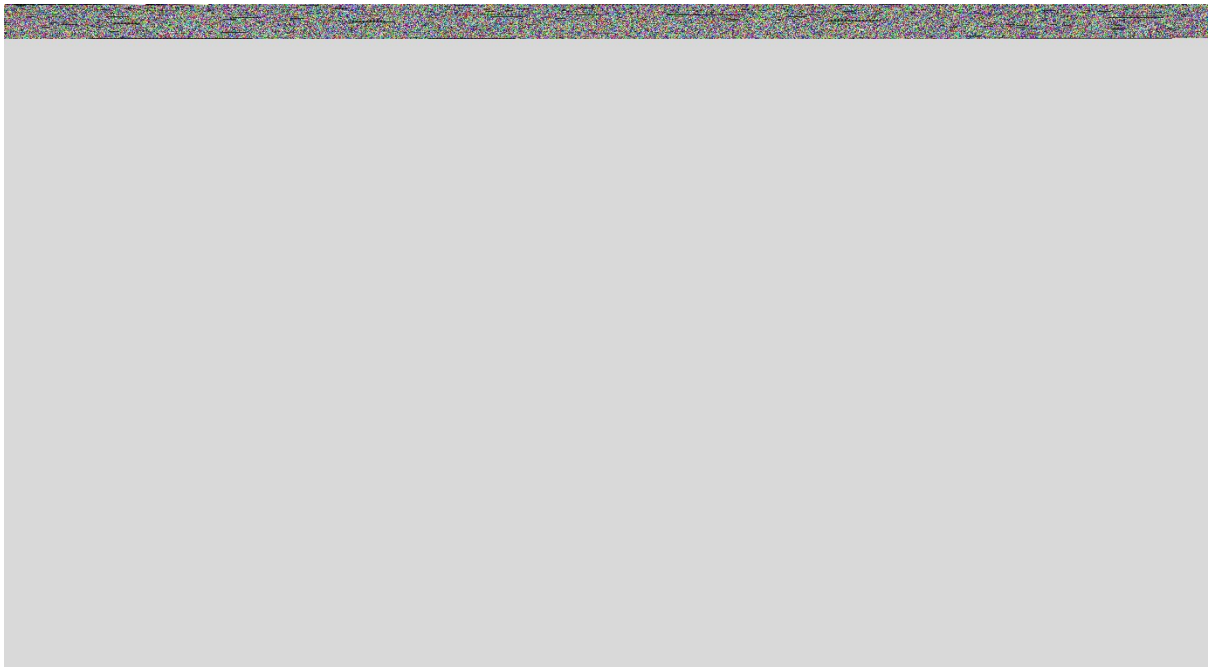

Fig. 6 Chemical diagrams for the nine most stable conformers calculated for **4**, *i.e.* **4-1** to **4-9**, their relative energies and Boltzmann distribution.

Additional structural information was revealed through this analysis. Crucially, the six most stable conformations, **4-1** to **4-6**, have an *anti*-disposition of the thione-S and amine-H atoms, with S1–C1–N1–H1n torsion angles in the range 140.1 to 156.9°, compared *syn*-dispositions in **4-7** to **4-9** (S1–C1–N1–H1n: 19.7 to 20.8°) with the difference in energy between **4-6** and **4-7** being 0.2-0.3 kcal mol^{-1}. The analysis also highlights the importance of the intramolecular amine-N–H···O(hydroxyl) hydrogen bonds compared with the hydroxyl-O–H···S(thione) and putative hydroxyl-O–H···O(hydroxyl) hydrogen bonds, with conformers **4-1** to **4-4** being lower in energy compared with conformers without amine-N–H···O(hydroxyl) hydrogen bonds.

Geometry optimisation calculations for **1-4** were conducted and an overlay diagram for these are shown in Fig. 2(h) from which it can be seen that the disparities in the conformations of the experimentally-determined structures no longer persist, with only minor differences noted in the relative orientations conformations of the aryl groups. Selected geometric parameters for the optimised structures are collated in Table 2. First and foremost, any differences apparent between the independent molecules of **1** and of **4** are no longer apparent. For example, the difference in the C1–N1–C2 angles of approximately 3° in **1** disappears. Concerning the relative dispositions of the aryl groups, Fig. 2(h), it was noted above the S1–C1–N1–C2 angles in experimental **2-4** were closer to planarity compared with **1** but in the optimised molecules, all approximate the conformation seen in experimental and theoretical **1**, yet a range of angles, *i.e.* 13.2° (**2**) to -19.0° (**4**) is still apparent. This along with a range of about 12° for the C1–N1–C2–C3 torsion angles are the exceptional differences with all of the other angles equal within a degree of each other. With respect to bond lengths, in the crystals of **1-3** the C1–N1, N2 bond lengths are equal within experimental error but are distinct for each independent molecule in **4**, Table 2. In the optimised structures, C1–N2 is marginally longer than C1–N1 in **1-3** but, for **4**, there are more significant differences apparent with the C1–N1 bond length being longer than C1–N2. This change is related to the influence of the electronegative nitro substituent in **4**. The above systematic variations in geometric parameters notwithstanding, it is emphasised the differences are small and are unlikely to have a significant influence upon the molecular packing.

Molecular electrostatic potential (MEP) and natural population analysis (NPA)

Compounds **1-4** were subjected to molecular electrostatic potential (MEP) mapping and a natural population analysis (NPA) in order to better comprehend the distribution of electron density over the molecules (the relative polarity) with the view to correlate any systematic

trends with the non-covalent interactions operating in the respective crystals. It is noted that the NPA approach was chosen for the charge calculations for its reliability and for being less sensitive to the choice of basis set functions.[73]

As shown in Fig. 7, the MEP maps were plotted onto the iso-density surfaces (0.0004 a.u., the low value being chosen for the generation of high-quality mapping) for **1**-**4**; a listing of the electrostatic charges is given in ESI† Table S1. The most noteworthy features of the MEP plots are the intense positive (blue) regions centred on the H1o atoms as well as the negative (orange to red) regions around the S1 and O2 atoms with the electrostatic potential charge (V_{ESP}) on the surfaces being in the range of +55.73 to +59.49 kcal mol^{-1} for H1o, -30.37 to -36.09 kcal mol^{-1} for S1, and -39.30 to -42.45 kcal mol^{-1} for the O2 atom. The electrostatic potential charges correspond well with the experimental findings in that electropositive-H1o interacts with electronegative-O2 through charge-complementary, electrostatic attractions that results in systematic hydroxy-O–H···O(hydroxy) hydrogen bond formation in **1**-**4**. While there are some inequivalent distributions of electrostatic potential charge on the H1o and O1 atoms in **1**-**4**, the net charge (ΔV_{ESP}) is approximately the same across the series with the values being 97.74, 98.44, 98.72 and 98.79 kcal mol^{-1}, respectively, indicating similar strengths for these interactions. These net charge values are relatively greater than the electrostatic attraction for putative methylene-C–H···S(thione) interactions in the molecular packing for **1** and **4**, with energies of 65.12 and 66.61 kcal mol^{-1}, respectively and aryl-C–H···S(thione) for **1** with an energy = 41.05 kcal mol^{-1}. However, in **1**, these occur at distances beyond the van der Waals radii so are not indicated in the analysis conducted using *PLATON*[37] but are noted in the Hirshfeld surface analysis (*vide infra*). The identified methylene-C–H···Cl1 and Cl···Cl interactions in **3**, Table 3, have net charge values of 32.40 and -1.88 kcal mol^{-1}, respectively, indicating the latter is diffusive in nature. As well, methylene-C–H···O(nitro) and aryl-C–

View Article Online
DOI: 10.1039/D0CE01810D

H···O(nitro) in **4** have energies equal to 49.43 and 44.72 kcal mol^{-1}, respectively; the latter occur at separations greater than the van der Waals radii.

Fig. 7 Electrostatic potentials mapped onto the iso-density surfaces (0.0004 a.u.) for **1**-**4**, in the range -60.00 to +60.00 kcal mol^{-1}.

The effect on the variation of the 4-Y substituent of the aryl rings is evidenced through MEP mapping. Thus, the electrostatic charge on the centroid of the aryl ring becomes more negative from **1** to **2** due to the electron donating nature of the Y = Me substituent in **2**, while the opposite is true for **3** and **4**, as the aryl rings become less negative owing to the electron-withdrawing effects of the Y = Cl and NO_2 substituents.

Similar to the MEP analysis, the NPA study was conducted to seek trends in the charge distribution on specific atoms especially those participating in intermolecular interactions for

correlation with molecular packing. A list of selected NPA values is given in Table 4 and a full listing is given in ESI† Table S2. The NPA charge analysis shows that the most basic sites are located on the hydroxyl-O1 and O2 atoms with the natural charge values in the ranges -0.736 to -0.737 and -0.743 to -0.749, respectively, indicating the O2 atom is marginally more negative. The corresponding H1o and H2o atoms are the most acidic sites with charge values of about 0.50 and 0.48, respectively, in accord with the trends with the hydroxyl-O atoms. Consistent with the MEP study, are the relatively large difference in the natural charges between the hydroxyl-oxygen and -hydrogen atoms and this is the main contributing factor for the formation of the common hydroxy-O–H···O(hydroxy) hydrogen bonded chain formation in **1**-**4**.

Table 4 The natural charges for selected atoms in the optimised molecules of **1**-**4**.

Atom	Natural Charge, |e|			
	1	**2**	**3**	**4**
S1	-0.393	-0.397	-0.387	-0.361
N1	-0.613	-0.611	-0.613	-0.614
N2	-0.396	-0.397	-0.393	-0.384
O1	-0.737	-0.737	-0.737	-0.736
O2	-0.748	-0.749	-0.747	-0.743
C1	0.345	0.346	0.344	0.338
C2	0.141	0.126	0.141	0.195
C3	-0.215	-0.205	-0.197	-0.222
C4	-0.208	-0.212	-0.224	-0.169
C5	-0.226	-0.024	-0.053	-0.010
C6	-0.205	-0.209	-0.222	-0.164
C7	-0.234	-0.224	-0.216	-0.235
H1o	0.496	0.496	0.496	0.498

View Article Online
DOI: 10.1039/D0CE01810D

H2o	0.480	0.480	0.480	0.480
H1n	0.444	0.444	0.445	0.448

It is noted that small but consistent trends in the charges residing on the S1 and N2 atoms are apparent, with respect to **1**, minor increases in **2** and decreases in **3** and **4** correlated with the electronegativity of Y. Variations in the natural charges are also noted in the aryl rings, in particular for the C5 atoms with respect to **1**, observations again related to the Y-substituents. For **2**, the inductive effect of the σ-electron donating methyl group disperses charge around the π-system through the resonance effect.[74] A similar observation is found for the Cl substituent in **3** as it able to donate the lone-pair of electrons to the aryl ring leading to a similar inductive effect as for the methyl substituent despite the chloride atom being known as a weak electron-withdrawing group.[75] The significant differences for all atoms comprising the aryl ring in **4** relates specifically to the electronegative nitro substituent. Overall, the net charge shift[76] for the 4-substituted phenylthiourea fragments compared to the parent molecule, *i.e.* $[\Sigma q(SCNHC_6H_4Y) - \Sigma q(SCNHC_6H_5)]$, computes to 0.004, -0.007 and -0.033 e for **2**-**4**, respectively, which correlates to the electron-donating nature of Me and electron-withdrawing characteristics of Cl and NO_2.

Hirshfeld surface analysis

Compounds **1**-**4** were subjected to Hirshfeld surface analysis in order to gain further insight on the nature of interactions present in each crystal, especially those not identified in the conventional analysis of the molecular packing, as well as important surface contacts; the analysis includes the contributions made by the individual components comprising the asymmetric unit of each of **1** and **4**, labelled henceforth **1a** & **1b** and **4a** & **4b**, respectively The mapping of the normalised contact distances (d_{norm}) reveals several red spots on the iso-

density surfaces of the molecules ranging from strong to weak intensity due to the presence of several close contacts with separations shorter than the sum of van der Waals radii.[62] These are categorised into five main types as H···O/O···H (type I), H···C/C···H (type II), H···S/S···H (type III), C···O/O···C (type IV) and H···Cl/Cl···H or Cl···Cl (type V), Fig. 8. A summary of the contacts detected on the Hirshfeld surfaces is provided in ESI† Table S3 where all the X–H bond lengths have been adjusted to their neutron values.

The most intense red spots arise from H···O/O···H interactions due to the hydroxyl-O–H···O(hydroxyl) hydrogen bonds and these are a common feature of all crystals under investigation. The differences between the molecules are observed mainly in the diminutive red spots comprising type II, III, IV and V contacts. For instance, a type IV contact appears only for **1b** due to thiourea-C1···O(hydroxyl) interaction, while type III contacts are observed in **1** and **4** attributed to methylene-/aryl-C–H···S(thione) interactions but no such contact is noted either of **2** and **3**. The inclusion of Cl and NO_2 substituents in the 4-positions of **3** and **4** introduces additional contacts compared with the parent molecule of **1** as evidenced from the presence of red spots, albeit of weak intensity. For **3**, these arise from methylene-C–H···Cl and Cl···Cl interactions in **3**; while the NO_2 substituent in **4** gives rise to methylene-/aryl-C–H···O(nitro) interactions. Almost all of these interactions identified through the Hirshfeld surface analysis can be considered weak contacts which complement those interactions detected *via PLATON*.[37]

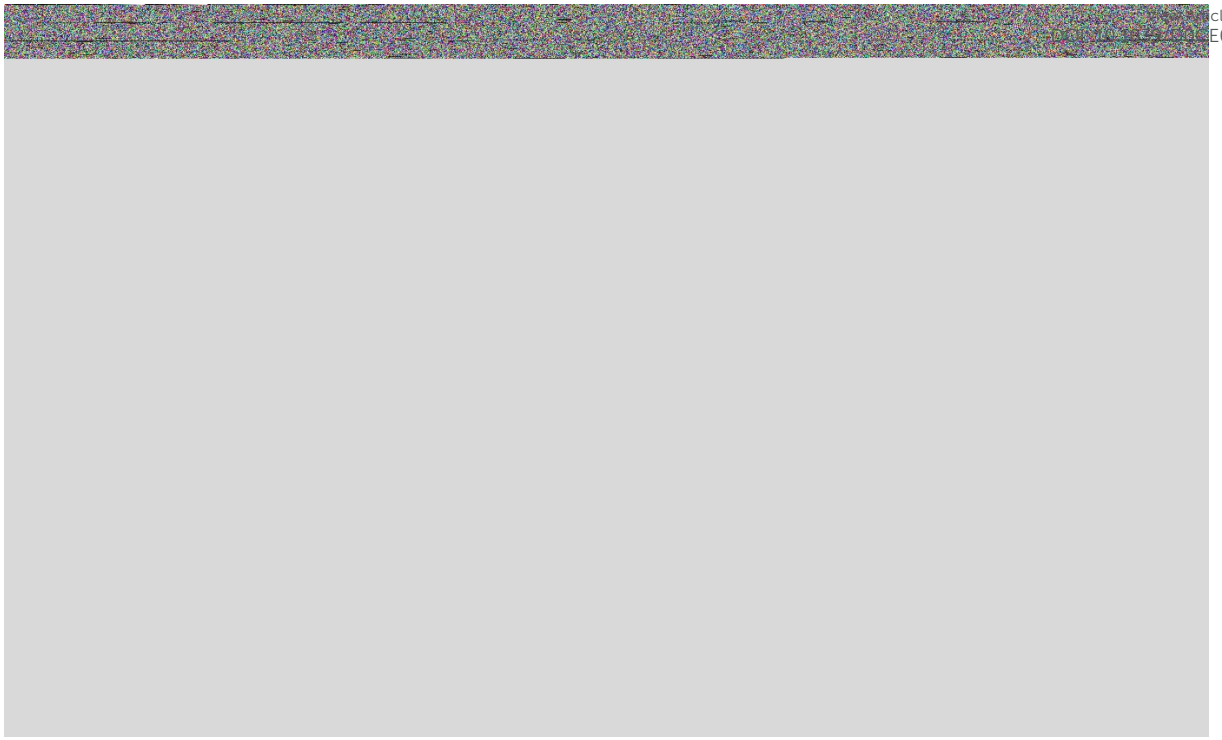

Fig. 8 Complementary views of the Hirshfeld surface mapped over d_{norm} within the range of -0.0788 to 1.0548 arbitrary units, revealing close contacts shorter than the sum of van der Waals radii through red spots on the surfaces which are categorised into H···O/O···H (type I), H···C/C···H (type II), H···S/ S···H (type III), C···O/O···C (type IV) and H···Cl/Cl···H or Cl···Cl (type V) for (a) **1a**, (b) **1b**, (c) **2**, (d) **3**, (e) **4a** and (f) **4b**.

The quantification of the close contacts to the Hirshfeld surface was achieved though the analysis of the two-dimensional fingerprint plots for the respective molecules in **1**-**4**. In general, the variation of intermolecular interactions owing to the differences in molecular packing is reflected in the fingerprint profiles for the individual molecules, despite these often being subtle, particularly in the diffuse regions of the overall profiles as illustrated in ESI† Fig. S4.

The most prominent features of the fingerprint plots are the pairs of forceps-like spikes tipped at $d_i + d_e$ distances within 1.70-1.76 Å which are much shorter than the sum of van der

Waals radii (vdW) for O···H [$\Sigma(vdW)_{O\cdots H}$ = 2.61 Å], *cf.* the d_{norm} contact distances listed in ESI† Table S3. These features arise due to the H···O/O···H hydrogen bonding contacts leading to the supramolecular chains. Also prominent are the pincers-like distributions in the decomposed fingerprint plots for the H···C/C···H contacts with $d_i + d_e$ distances in the range 2.65-2.76 Å which are slightly shorter than $\Sigma(vdW)_{C\cdots H}$ of 2.79 Å. The H···S/ S···H contacts are also reflected as pincers-like profile but with $d_i + d_e$ distances in range 2.83 to 2.94 Å for **1** & **4** and 2.90 to 3.03 Å for **2** & **3** compared with the $\Sigma(vdW)_{S\cdots H}$ = 2.89 Å. It is for this reason that diminutive red spots were observed in the relevant plots for **1** and **4** but not in those for **2** & **3**; as discussed below, the H…S contacts in **2**-**4** are intra-chain contacts. Distinctive characteristics are noted in **3** arising from H···Cl/Cl···H as well as Cl···Cl contacts with $d_i + d_e$ of about 2.78 and 3.42 Å which are shorter than $\Sigma(vdW)_{Cl\cdots H}$ and $\Sigma(vdW)_{Cl\cdots Cl}$ of 2.84 and 3.50 Å, respectively, Fig. 9. Other contacts co-exist on the Hirshfeld surface but are less significant owing to long contact separations.

Fig. 9 Decomposed fingerprint plots for **3** delineated into (a) H···Cl/Cl···H and (b) Cl···Cl contacts.

In terms of contact distributions, crystals **1** and **2** are dominated by several major contact contributions to the Hirshfeld surfaces in the order of H···H (*ca* 57.3-59.5%), H···C/C···H (*ca*

View Article Online
DOI: 10.1039/D0CE01810D

17.2-18.7%), H···S/S···H (*ca* 10.6-12.0%) and H···O/O···H (*ca* 8.4-10.8%) followed by other less significant contacts with each contributing less than 1% as shown in Fig. 10. The decomposition of the distribution shows that almost all contacts in **1** and **2** are evenly distributed between the internal (*i.e*. the donor or acceptor atoms internal to the surface) and external (*i.e*. the donor or acceptor atoms external to the surface) interactions except for H···C/C···H and H···S/S···H which are slightly inclined toward (internal)-X···H-(external) rather than (internal)-H···X-(external) (X = C and S) owing to their relatively large exposure surfaces that attract the contact from hydrogen atoms, *e.g*. for C···H, the contact is mainly concentrated within the aryl ring with a large exposure surface.

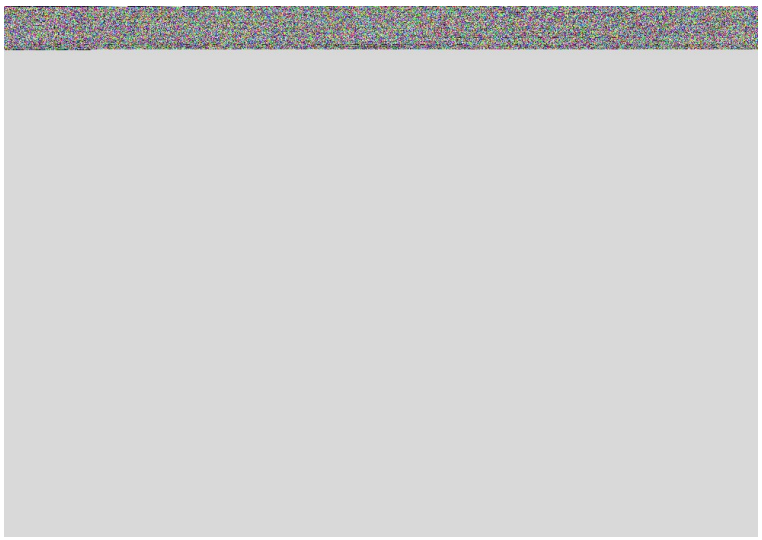

Fig. 10 Relative distribution of different contacts to the Hirshfeld surfaces for individual molecules in **1-4**. Other minor but significant contacts include C···Cl/Cl···C (2.8%), H···N/N···H (2.3%) and Cl···Cl (1.1%) for **3**. For **4a** and **4b**: H···N/N···H (2.5%), O···C/C···O (1.0-2.3%), O···S/ S···O (1.4-1.5%) and O···O (0.1-1.3%), and specifically for 4**b** C···C (3.0%).

View Article Online
DOI: 10.1039/D0CE01810D

Distinctive distributions are noted for each of **3** and **4** owing to the influence of the X = Cl an NO_2 substituents, respectively. Thus for **3**, the contributions are in the order H···H (41.3%), H···C/C···H (15.7%), H···Cl/Cl···H (14.7%), H···S/S···H (10.8%) and H···O/O···H (9.8%) and other minor contacts including the Cl···Cl contact which constitutes only 1.1%. For **4**, the order is H···O/O···H (*ca* 32.2-35.2%), H···H (*ca* 32.4-33.6%), H···C/C···H (*ca* 12.2-17.1%), H···S/ S···H (*ca* 8.5%) followed by other long contacts (*ca* 9.7-10.8%). Similar to **1** and **2**, decomposition of the corresponding contacts exhibits uneven distributions between the internal and external contacts for H···Cl/Cl···H in **3** as well as H···O/O···H in **4** in addition to the H···C/C···H and H···S/S···H contacts in both molecules, for which the interactions are inclined toward (internal)-X···H-(external) (X = Cl, O, C and S) indicating the electronegative nature of those acceptor atoms.

Interaction energies and energy frameworks

An analysis of the interaction energies associated with identified intermolecular contacts was quantitatively assessed in attempt to rank the stabilisation energies provided by specific contacts in **1-4**. The strength of each interaction as identified from the Hirshfeld surface analysis was assessed following the approach as detailed in the experimental section. As noted from Table 5, among all pairwise-interactions between molecules, the hydroxyl-O–H···O(hydroxyl) interactions provide the strongest interactions with the energy, E_{int}, for each pair lying in the range -17.81 to -12.09 kcal mol^{-1}. These strengths are comparable to that of *ca* -18 and -17 kcal mol^{-1} as calculated for the classical amide-N–H···O(amide)[77] and carboxylic-O–H···O(carboxylic acid) interactions,[78] respectively. A close inspection of the data shows that the E_{int}(O–H···O) is the greatest in crystal **2**, and this is followed by **3**, **4** and **1** respectively.

View Article Online
DOI: 10.1039/D0CE01810D

Apart from the O–H···O interactions, crystals **1-4** also feature C–H···O and C–H,π interactions with the E_{int} ranging from -2.27 to -10.56 kcal mol^{-1} and -4.09 to -8.58 kcal mol^{-1}, respectively. Additional C–H···S and C···O interactions found in **1** have relatively strong interaction energies with E_{int}(C–H···S) in the range -2.20 to -7.93 kcal mol^{-1} and E_{int}(C···O) in the range -4.11 to -11.76 kcal mol^{-1}. The C–H···Cl interaction in **3** exhibits a relatively weak E_{int} of -2.01 kcal mol^{-1} and the Cl···Cl interaction is very weak with E_{int} being close to 0 kcal mol^{-1}. The only π···π interactions among the series is only present in **4** and gives rise to a relatively strong E_{int} of -13.53 kcal mol^{-1}.

From the data in Table 5, it is evident the molecular packing of **1-4** is mainly stabilised by electrostatic forces owing to the strong O–H···O interactions which lead to the directional topology aligned along the *c*-axis for **1** and along *b*-axes for **2-4**, Fig. 11. The crystals also feature dispersive forces due to the other complementary contacts. The overall energy framework of **1** has a ladder-like topology in contrast to the zig-zag, sheet-like energy framework for **4**, while crystals **2** and **3** exhibit a similar, rack-shape topology consistent with their isostructural relationship. It is noteworthy some smaller repulsive forces are observed within the rack-shaped topology of **2** and **3** owing to the close proximity of the main electrostatic force resulting from the O–H···O interactions, the magnitude of which is inversely proportional to the distance of the point charges in accord with Coulomb's law.[79] Equivalent repulsive forces are not observed in **1** and **4**.

Table 5 Corrected interaction energies (kcal mol^{-1}) for all intermolecular close contacts present in **1** to **4**, with scale factors of 1.057, 0.740, 0.871 and 0.618 being applied for $E_{electrostatic}$, $E_{polarization}$, $E_{dispersion}$ and $E_{repulsion}$, respectively, as obtained from the CE-B3LYP/6-31G(*d*,*p*) model.[63]

Contact	$E_{electrostatic}$	$E_{polarization}$	$E_{dispersion}$	$E_{repulsion}$	E_{total}	Symmetry operation
1						
O1–H1o···O22	-16.27	-3.11	-2.04	9.34	-12.09	*x*, *y*, *z*
O21–H21o···O2	-17.36	-3.41	-3.73	9.85	-14.65	*x*, *y*, 1+*z*
C28–H28b···O1/ C9–H9a···π(C22–C27)/ C29–H29a···π(C2–C7)	-4.93	-1.15	-9.76	5.29	-10.56	1-*x*, 1-*y*, 1-*z*
C5–H5···O1	-1.59	-0.35	-3.56	1.40	-4.11	1½-*x*, ½+*y*, ½-*z*
C29–H29b··· π(C2–C7)	-4.85	-1.38	-6.08	4.56	-7.74	-½+*x*, ½-*y*, ½+*z*
C4–H4···S21	-1.67	-0.28	-1.73	1.46	-2.20	1½-*x*, ½+*y*, ½-*z*
C8–H8a···S21/ C10–H10a··· π(C22–C27)	-5.03	-0.94	-4.73	2.76	-7.93	-½+*x*, ½-*y*, -½+*z*

C21···O22	-5.48	-2.12	-8.97	4.80	-11.76	1-*x*, 1-*y*, 1-*z*
2						
O1–H1o···O2	-17.89	-3.71	-6.43	10.22	-17.81	-½-*x*, -½+*y*, 1½-*z*
C6–H6···O2/ C4–H4···C10	-2.75	-0.90	-7.85	4.02	-7.48	½-*x*, -½+*y*, 1½-*z*
C10–H10b···π(C2–C7)	-2.73	-0.64	-4.91	3.31	-4.95	-½+*x*, ½-*y*, -½+*z*
C9–H9a···π(C2–C7)/ C8–H8b···π(C2–C7)	-4.37	-1.49	-7.41	4.70	-8.58	-1+x, y, z
3						
O1–H1o···O2	-17.13	-3.91	-6.45	10.43	-17.09	-½-*x*, ½+*y*, ½-*z*

C6–H6···O2/						
C4–H4···C10	-4.95	-0.81	-7.97	4.67	-9.08	½-*x*, ½+*y*, ½-*z*
C10–H10a···π(C2–C7)	-1.52	-0.62	-4.98	3.03	-4.09	-½+*x*, 1½-*y*, -½+*z*
C9–H9b···π(C2–C7)/						
C8–H8a···π(C2–C7)	-2.85	-1.22	-6.85	3.97	-6.69	-1+*x*, *y*, *z*
C10–H10b···Cl1	-1.29	-0.16	-1.85	1.29	-2.01	-1½+*x*, 1½-*y*, -½+*z*
Cl1···Cl1	-0.13	-0.02	-0.73	0.83	-0.05	2-*x*, 1-*y*, 1-*z*
4						
O1–H1o···O22	-14.83	-4.00	-7.02	9.70	-16.13	*x*, 1+*y*, *z*
O21–H21o···O2	-14.45	-4.10	-7.22	9.59	-16.18	*x*, *y*, *z*
C29–H29b···O1	-0.43	-0.48	-3.98	2.60	-2.27	-*x*, 1-*y*, 1-*z*
C11–H11b···O3	-4.85	-0.78	-2.41	2.42	-5.62	*x*, *y*, 1+*z*

C7–H7···O23	-2.58	-0.46	-2.98	1.67	-4.35	*x*, 1+*y*, -1+*z*
C27–H27···O3	-2.78	-0.46	-3.02	1.67	-4.59	*x*, *y*, 1+*z*
C30–H30a··· π(C2–C7)/ C30–H30b···S1	-4.14	-0.88	-7.49	5.29	-7.24	1-*x*, 1-*y*, 1-*z*
C10–H10b··· π(C22–C27)/ C10–H10a···S21	-3.79	-0.83	-7.20	4.77	-7.07	1-*x*, 1-*y*, 2-*z*
C31–H31a···O23	-3.87	-0.62	-2.17	1.20	-5.47	*x*, *y*, -1+*z*
π(C22–C27)···π(C22–C27)	-6.24	-0.87	-10.89	4.46	-13.53	-*x*, -*y*, 2-*z*

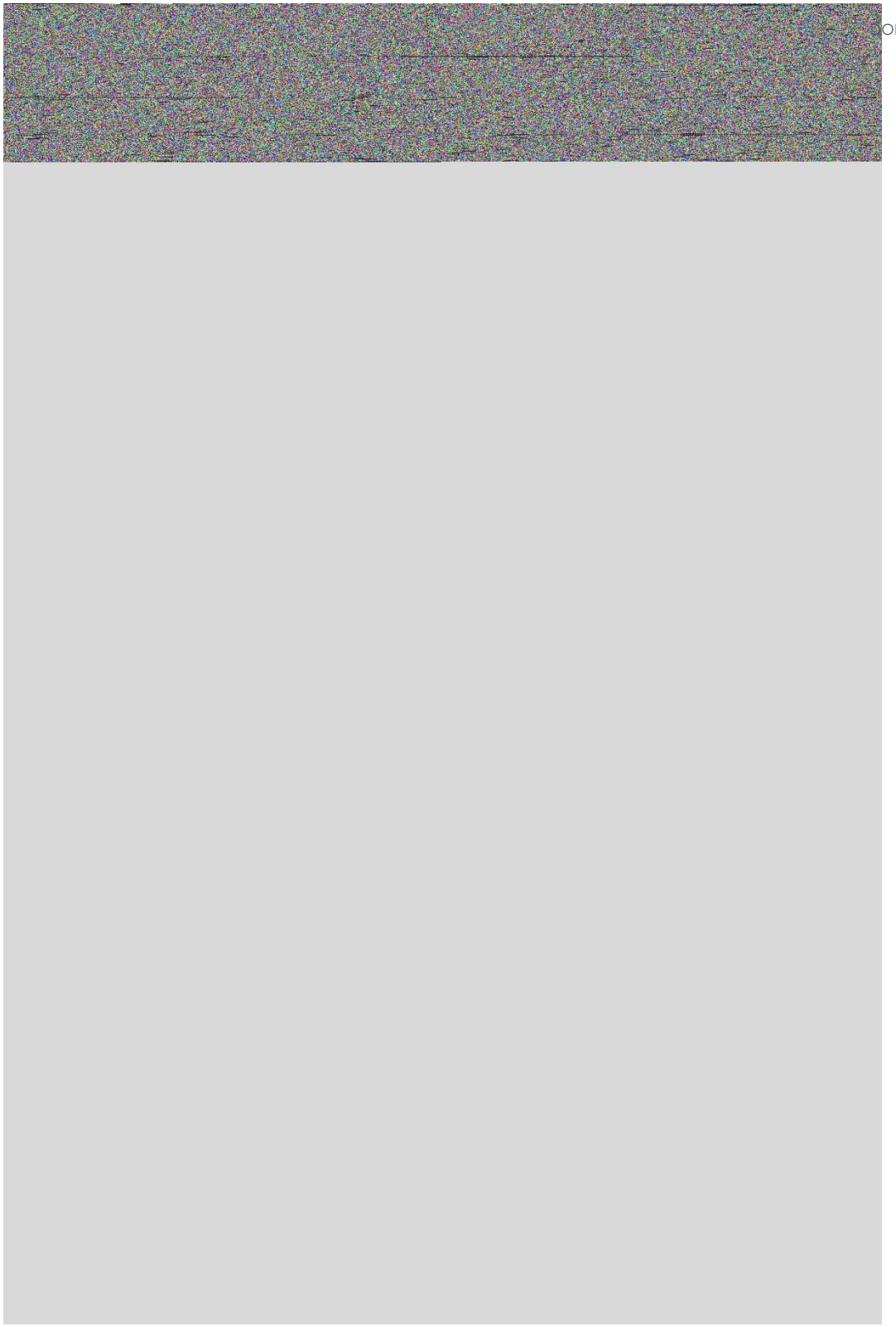

Fig. 11 Perspective views of the energy frameworks of **1**-**4** showing the (a) electrostatic force, (b) dispersion force and (c) total energy diagram. The cylindrical radius is proportional to the

View Article Online
DOI: 10.1039/D0CE01810D

relative strengths of the corresponding energies and were adjusted to the same scale factor of 100 with a cut-off value of 1.91 kcal mol^{-1} within 2 × 2 × 2 unit-cells.

Data in Table 6 indicate the calculated lattice energies follow the order of **2** (-25.70 kcal mol^{-1}) > **1** > **3** > **4** (-23.78 kcal mol^{-1}) with the range being about 2 kcal mol^{-1}. The order of the lattice energies correlates nicely with the relative greater contributions to the energies of stabilisation provided by the C–H···π(aryl) interactions through enhanced contributions which follow the same order. Further, the identified methylene-C–H···Cl(chloride) and aryl-C–H···O(nitro) interactions in **3** and **4**, respectively, exert little influence upon the lattice energies due to their weak nature. By contrast, the energy contribution from the π(aryl)···π(aryl) contact is **4** is significant.

Table 6 The lattice energy ($E_{lattice}$) in kcal mol^{-1} and the corresponding energy components ($E_{electrostatic}$, $E_{polarization}$, $E_{dispersion}$ and $E_{repulsion}$) calculated for a cluster of molecules within 25 Å from a reference molecule through the CE-B3LYP/6-31G(*d*,*p*) model.

Crystal	$E_{electrostatic}$	$E_{polarization}$	$E_{dispersion}$	$E_{repulsion}$	$E_{lattice}$
1	-16.19	-4.23	-16.70	12.29	-24.83
2	-14.72	-4.33	-19.30	12.65	-25.70
3	-14.77	-4.29	-18.62	13.06	-24.62
4	-15.01	-3.98	-16.82	12.03	-23.78

Non-covalent interaction (NCI) plots

Non-covalent interaction plots[58] were calculated for selected interactions identified in the crystals of **1**-**4** to verify the attractive nature of the interactions through visualisation a red-blue-green colour scheme on the iso-surface; red is indicative of a strong repulsive interaction, blue is indicative of a strong attractive interaction while green is indicative of a weak interaction.[80] The images of Fig. 12 reveal that the intermolecular hydroxyl-O–H···O(hydroxyl) interaction, common in all crystals, along with the intramolecular amide-N–H···O(hydroxyl) and hydroxyl-O–H···S(thione) contacts, are strong and attractive in nature with the low density, low reduced gradient trough for those interactions lying at the negative region at about -0.20 to -0.35 a.u. in the respective two-dimensional NCI plots.

Fig. 12 NCI plots along with the two-dimensional plots of reduced density gradient (RDG) versus sign(λ^2)ρ(r) for the molecular dimers of **1**-**4** connected by hydroxyl-O–H···O(hydroxyl) hydrogen bonds and highlighting the intramolecular amide-N–H···O(hydroxyl) and hydroxyl-O–H···S(thione) hydrogen bonds. The gradient cut-off is set at 0.4 and the colour scale is -0.04 < ρ < 0.04 a.u. Non-essential atoms are truncated for clarity.

Interestingly, for pairs of molecules connected by hydroxyl-O–H···O(hydroxyl) hydrogen bonds in **2**-**4**, there are relatively large, diffuse green domains between the hydroxyethyl-H-and thione-S atoms (see ESI† Fig. S5) that serve to complement the hydrogen bonds; this confirmed in the corresponding QTAIM analysis[80] (see ESI† Fig. S6). The attractive interactions further strengthen the interactions leading to the supramolecular chains and are likely contributors to the reduction in their pitch.

In line with the Hirshfeld surface analysis, additional contacts are detected in **3**, *i.e.* methylene-C–H···Cl(aryl) and Cl···Cl, and **4**, *i.e.* methylene-C–H···O(nitro) and aryl-C–H···O(nitro), necessarily absent in **1** and **2**. As indicated from the light-green domains in the respective NCI plots of Fig. 13, these correspond to weak interactions. Other common interactions involving the aryl rings and methylene chains are considered weak and are evidenced through the high-density localised domains in the NCI plots of ESI† Fig. S5.

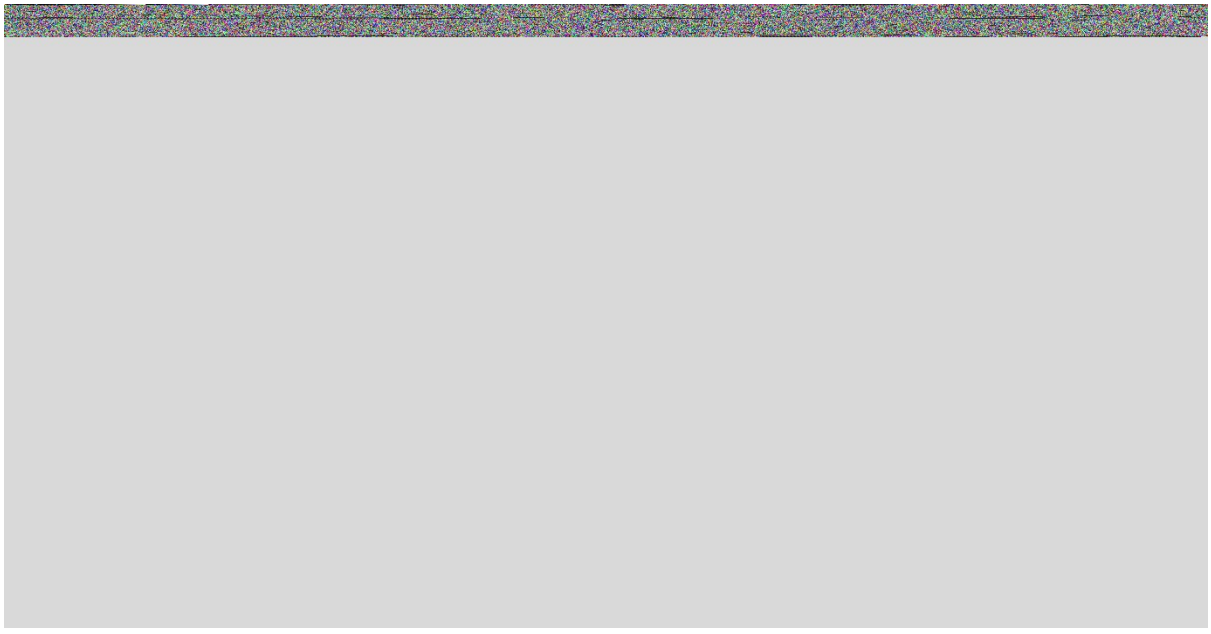

Fig. 13 NCI plots for the molecular dimers highlighting weak contacts in **3**: (a) methylene-C–H···Cl(aryl) and (b) Cl···Cl and **4**: (c) methylene-C–H···O(nitro) and (d) aryl-C–H···O(nitro).

Overview

Crystals of **1** comprise two independent molecules which associate to form a linear, supramolecular chain sustained, in part, by hydroxyl-O–H···O(hydroxyl) hydrogen bonds. In common with isostructural **2** and **3**, the space group of **1** is monoclinic, $P2_1/n$. There is a simple relationship between the crystals in that the unit-cell edge *a* in **2** and **3** is about half that of **1**, Table 1. Quite distinct crystal symmetry is noted for **4**, i.e. triclinic, $P\bar{1}$ with Z' = 2. Despite these differences, supramolecular chains featuring by hydroxyl-O–H···O(hydroxyl) hydrogen bonds are prominent in the crystals of **1**-**4**. However, unlike **1**, in the isostructural crystals of **2** and **3**, the chains have a helical topology. In **4**, zig-zag chains are apparent. In short, the topology of the supramolecular chains in **1**-**4** are syntactic with the crystalline environment in which they exist.[84]

Isostructural relationships are not uncommon for molecules differing in a chloro/methyl substituent, which have similar volumes, *i.e.* 19 Å^3 for chloride and 24 Å^3 for methyl.[82] Such cases of structural mimicry are commonly known as the chloro/methyl exchange,[83] but this concept can be expanded to include other substituents.[10] A chloro/methyl exchange in isostructural crystals implies similar influences upon the molecular packing by these substituents. This suggests the methylene-C–H···Cl(aryl) and Cl···Cl contacts noted in **3**, which occur in the inter-layer region, are not structure-directing even if weakly attractive. The methyl groups in **2**, which are also directed towards the inter-layer region, do not engage in directional interactions.

In terms of directional interactions, C–H···π(aryl) contacts feature in each crystal of **1**-**4**, and in **1**, lead to a three-dimensional architecture, in **2** and **3**, to a two-dimensional array and in **4**, to a double-layer. Further directional interactions are largely absent in **2** and **3**. By contrast, methylene-C–H···O(hydroxyl) and π(aryl)···π(aryl) interactions assemble the

double-layers in **4** (also stabilised by intra-layer methylene-C–H···O(nitro) contacts) into a three-dimensional arrangement.

At this stage it is salient to recall the results of the geometry optimisation calculations which indicate no significant influence is exerted by the methyl and chloro substituents in **2** and **3** but significant activation of the aryl ring owing to the electronegative nitro group in **4**. This latter observation correlates with the formation of the off-set π(aryl)···π(aryl) interactions observed in **4** but not in **1**-**3**.

An evaluation of the relative contributions of the different interaction energies to the overall energies of identified interactions reveals interesting trends. Thus, the energies (relative contributions) contributed by the hydroxyl-O–H···O(hydroxyl) hydrogen bonds are approximately -14.72 and -14.77 kcal mol^{-1} (46%) for **2** and **3**, -15.01 kcal mol^{-1} (40%) for **4** and -16.19 kcal mol^{-1} (38%) for **1**. This correlates with the repeat distances of the supramolecular chains with the greater energy contribution by hydroxyl-O–H···O(hydroxyl) hydrogen bonds to the overall energy of packing being associated with the chains with shortest repeat distances, *i.e*. **2** and **3** (10.77 Å) < **4** (11.21 Å) < **1** (16.47 Å).

While an exhaustive literature survey of this phenomenon is not feasible, as mentioned in the *Introduction*, a number of systematic studies have been described whereby the influence of small chemical changes upon supramolecular aggregation patterns investigated.[10-27] Except for an isostructural series[10] and universal adoption of the carboxylic dimer synthon in another series,[17] variations in the topology of the aggregate/chain/layer are the norm as small chemical changes are made to molecular formulae, even when comparable hydrogen bonds are evident. Such an observation confirms that in order to design a crystal let alone an aggregate within a crystal,[85] all supramolecular associations need to be taken in account.

Finally, it should be mentioned that during the course of these studies conducted over a period of well over five years in two different Institutions, involving repeated synthesis and crystallisations, no evidence for polymorphs or solvates was found. This is not to suggest that different crystalline forms are waiting to be discovered, in accord with the McCrone axiom.[86] However, it is stressed the experimental conformations in the crystals isolated in this study closely match the gas-phase optimised geometries suggesting the obtained crystals were the thermodynamic forms.

Conclusions

The crystal structure analyses along with detailed analyses of the supramolecular association in the crystals isolated for **1**-**4** show the formation of pervasive, hydrogen bonded chains that differ in topology: linear (**1**), helical (**2** and **3**) and zig-zag (**4**); no evidence for different crystalline forms was found in this study. In consideration of the (i) persistence of the hydroxyl-O–H···O(hydroxyl) hydrogen bonds leading to one-dimensional chains, (ii) the closeness of the calculated lattice energies, (iii) the relative importance of C–H···π(aryl) contacts operating normal to the chains and (iv) the, on average, more C–H···π(aryl) contacts formed per molecule in **1**, compared with **2**-**4**, it is concluded the different topologies of the supramolecular chains are related primarily to the influence of directional C–H···π(aryl) contacts. In **1**, where no other directional interactions are apparent, a more open, linear arrangement facilitates the formation of inter-chain C–H···π(aryl) interactions, by definition occupying a larger volume of space. In **2** and **3**, where C–H···π(aryl) interactions are less dominant, an observation traced to the Y = Me and Y = Cl substituents, helical chains are apparent. In **4**, where calculations indicate the aryl rings are activated, π(aryl)···π(aryl) interactions come to the fore and zig-zag chains are now apparent. Even if remote substituents

do not alter significantly the overall electronic structure of the molecules, their influence in participating in "second-tier" supramolecular association can direct the predominant mode of association between molecules leading to specific architectures.

In summary, the situation may be envisaged whereby the molecules precipitate from solution and align to form supramolecular chains *via* the predominant hydroxyl-O–H···O(hydroxyl) hydrogen bonds and the adopted topology is dictated by the need to optimise the supramolecular association between chains which, in turn, is moderated by the specific requirements of the remote substituents.

Author contributions

Sang Loon Tan: Data curation; Formal Analysis; Writing – original draft; Writing – review & editing

Edward R. T. Tiekink: Conceptualisation; Data curation; Formal Analysis; Funding acquisition; Writing – original draft; Writing – review & editing

Conflicts of interest

There are no conflicts to declare.

Acknowledgements

Nabihah Al Muna Mohd Nor is thanked for some preliminary experiments. The authors gratefully acknowledge Sunway University Sdn Bhd (Grant no. STR-RCTR-RCCM-001-2019) for support of crystallographic studies.

References

1. M. C. Etter, *Acc. Chem. Res*., 1990, **23**, 120–126.
2. G.A. Jeffrey, An Introduction to Hydrogen Bonding; Oxford University Press: New York, NY, USA, 1997.
3. T. Steiner, *Angew. Chem. Int. Ed.*, 2002, **41**, 48–76.
4. S. Scheiner, *Struct. Chem*., 2019, **30**, 1119–1128.
5. G. R. Desiraju, *Angew. Chem. Int. Ed. Engl.*, 1995, **34**, 2311–2317.
6. S. Scheiner, *J. Chem. Phys*., 2000, **153**, article no. 140901.
7. Q. Li and Z. Li, *Acc. Chem. Res*., 2020, **53**, 962–973.
8. A. P. Voronin, T. V. Volkova, A. B. Ilyukhin, A. N. Proshin and G. L. Perlovich, *CrystEngComm*, 2020, **22**, 349–360.
9. M. Kulułka, M. Srebo-Hooper and M. P. Mitoraj, *J. Phys. Chem. A*, 2020, **124**, 63–73.
10. A. Deya and G. R. Desiraju, *CrystEngComm*, 2004, **6**, 642–646.
11. D. Das and G. R. Desiraju, *CrystEngComm*, 2006, **8**, 674–679.
12. A. K. Jordaõ, V. F. Ferreira, A. C. Cunha, J. L. Wardell, S. M. S. V. Wardell and E. R. T. Tiekink, *CrystEngComm*, 2012, **14**, 6534–6539.
13. S. K. Seth, V. S. Lee, J. Yana, S. M. Zain, A. C. Cunha, V. F. Ferreira, A. K. Jordão, M. C. B. V. de Souza, S. M. S. V. Wardell, J. L. Wardell and E. R. T. Tiekink, *CrystEngComm*, 2015, **17**, 2255–2266.
14. L. Chęcińska, A. Jóźwiak, M. Ciechańska, C. Paulmann, J. J. Holstein, B. Dittrich and M. Małecka, *Z. Kristallogr. – Cryst. Mater.,* 2018, **233**, 675–687.
15. S. Y. Ho, R. P. A. Bettens, D. Dakternieks, A. Duthie and E. R. T. Tiekink, *CrystEngComm*, 2005, **7**, 682–689.
16. C. R. Kaiser, K. C. Pais, M. V. N. de Souza, J. L. Wardell, S. M. S. V. Wardell, and E. R. T. Tiekink, *CrystEngComm*, 2009, **11**, 1133–1140.

17. A. C. Cunha, V. F. Ferreira, A. K. Jordão, M. C. B. V. de Souza, S. M. S. V. Wardell, J. L. Wardell, P. A. Tan, R. P. A. Bettens, S. K. Seth and E. R. T. Tiekink, *CrystEngComm*, 2013, **15**, 4917–4929.

18. A. P. Voronin, T. V. Volkova, A. B. Ilyukhin, T. P. Trofimova and G. L. Perlovich, *CrystEngComm*, 2018, **20**, 3476–3489.

19. H. Andleeb, I. Khan, A. Franconetti, M. N. Tahir, J. Simpson, S. Hameed and A. Frontera, *CrystEngComm*, 2019, **21**, 1780–1793.

20. P. Mocilac and J. F. Gallagher, *CrystEngComm*, 2019, **21**, 4048–4062.

21. B. P. A. Gabriele, C. J. Williams, M. E. Lauer, B. Derby and A. J. Cruz-Cabeza, *Cryst. Growth Des*., 2020, **20**, 7516−7525.

22. C. Weck, E. Nauha and T. Gruber, *Cryst. Growth Des*., 2019, **19**, 2899–2911.

23. S. J. Pike, A. Heliot and C. C. Seaton, *CrystEngComm*, 2020, **22**, 5040–5048.

24. A. Dey, R. K. R. Jetti, R. Boese and G. R. Desiraju, *CrystEngComm*, 2003, **5**, 248–252.

25. M. D. L. Tonin, S. J. Garden, M. M. Jotani, J. L. Wardell and E. R. T. Tiekink, *Z. Kristallogr. – Cryst. Mater.,* 2019, **234**, 183–200.

26. F. Chen, Y. Wang, W. Zhang, T. Tian, B. Bai, H. Wang, F.-Q. Bai and M. Li, *Cryst. Growth Des*., 2019, **19**, 6100–6113.

27. H. Chung, S. Chen, B. Patel, G. Garbay, Y. H. Geerts and Y. Diao, *Cryst. Growth Des*., 2020, **20**, 1646–1654.

28. D. C. Schroeder, *Chem Rev*., 1955, **55**, 181–228.

29. J.-P. Griffiths, B. Maliha, M. G. Moloney, A. L. Thompson and I. Hussain, *Langmuir*, 2010, **26**, 14142–14153.

30. M. Banerjee, R. Karri, A. Chalana, R. Das, R. K. Rai, K. S. Rawat, B. Pathak and G. Roy, *Chem. – Eur. J*., 2017, **23**, 5696–5707.

31. S. M. Lee, A. H. S. Azizan and E. R. T. Tiekink, *Molbank*, 2018, **2018**, article no. M1035.

32. G. M. Viana, D. C. Soares, M. V. Santana, L. Henriques do Amaral, P. W. Meireles, R. P. Nunes, L. C. R. Pereira da Silva, L. C. de S. Aguiar, C. R. Rodrigues, V. Pereira de Sousa, H. C. Castro, P. A. Abreu, P. C. Sathler, E. M. Saraiva and L. M. Cabral, *Chem. Pharm. Bull*., 2017, **65**, 911–919.

33. Agilent Technologies, CrysAlisPro, Santa Clara, CA, USA, 2013.

34. G. M. Sheldrick, *Acta Crystallogr., Sect. A: Found. Crystallogr*., 2008, **64**, 112–122.

35. G. M. Sheldrick, *Acta Crystallogr*., *Sect. C: Struct. Chem*., 2015, **71**, 3–8.

36. L. J. Farrugia, *J. Appl. Crystallogr*., 2012, **45**, 849–854.

37. A. L. Spek, *Acta Crystallogr. Sect. E: Crystallogr. Commun*., 2020, **76**, 1–11.

38. K. Brandenburg, DIAMOND, Crystal Impact GbR, Bonn, Germany, 2006.

39. T. A. Halgren, *J. Comput. Chem*., 1996, **17**, 490–519.

40. Spartan'16, Wavefunction, Inc. Irvine, CA.

41. Y. Shao, L. F. Molnar, Y. Jung, J. Kussmann, C. Ochsenfeld, S. T. Brown, A. T. B. Gilbert, L. V. Slipchenko, S. V. Levchenko, D. P. O'Neill, R. A. DiStasio Jr., R. C. Lochan, T. Wang, G. J. O. Beran, N. A. Besley, J. M. Herbert, C. Y. Lin, T. Van Voorhis, S. H. Chien, A. Sodt, R. P. Steele, V. A. Rassolov, P. E. Maslen, P. P. Korambath, R. D. Adamson, B. Austin, J. Baker, E. F. C. Byrd, H. Dachsel, R. J. Doerksen, A. Dreuw, B. D. Dunietz, A. D. Dutoi, T. R. Furlani, S. R. Gwaltney, A. Heyden, S. Hirata, C.-P. Hsu, G. Kedziora, R. Z. Khalliulin, P. Klunzinger, A. M. Lee, M. S. Lee, W. Z. Liang, I. Lotan, N. Nair, B. Peters, E. I. Proynov, P. A. Pieniazek, Y. M. Rhee, J. Ritchie, E. Rosta, C. D. Sherrill, A. C. Simmonett, J. E. Subotnik, H. L. Woodcock III, W. Zhang, A. T. Bell, A. K. Chakraborty, D. M. Chipman, F. J. Keil, A.

Warshel, W. J. Hehre, H. F. Schaefer, J. Kong, A. I. Krylov, P. M. W. Gill and M. Head-Gordon, Phys. *Chem. Chem. Phys*., 2006, **8**, 3172–3191.

42. C. C. J. Roothaan, *Rev. Mod. Phys*., 1951, **23**, 69–89.
43. W. J. Pietro, M. M. Francl, W. J. Hehre, D. J. DeFrees, J. A. Pople and J. S. Binkley, *J. Am. Chem. Soc*., 1982, **104**, 5039–5048.
44. J. D. Chai and M. Head-Gordon, *Phys. Chem. Chem. Phys*., 2008, **10**, 6615–6620.
45. G. A. Petersson, A. Bennett, T. G. Tensfeldt, M. A. Al-Laham and W. A. Shirley, *J. Chem. Phys*., 1988, **89**, 2193–2218.
46. C. L. Andersen, C. S. Jensen, K. Mackeprang, L. Du, S. Jørgensen and H. G. Kjaergaard, *J. Phys. Chem. A*, 2014, **118**, 11074–11082.
47. A. D. McLean and G. S. Chandler, *J. Chem. Phys*., 1980, **72**, 5639–5648.
48. R. Krishnan, J. S. Binkley, R. Seeger and J. A. Pople, *J. Chem. Phys*., 1980, **72**, 650–654.
49. M. J. Frisch, G. W. Trucks, H. B. Schlegel, G. E. Scuseria, M. A. Robb, J. R. Cheeseman, G. Scalmani, V. Barone, B. Mennucci, G. A. Petersson, H. Nakatsuji, M. Caricato, X. Li, H. P. Hratchian, A. F. Izmaylov, J. Bloino, G. Zheng, J. L. Sonnenberg, M. Hada, M. Ehara, K. Toyota, R. Fukuda, J. Hasegawa, M. Ishida, T. Nakaji-ma, Y. Honda, O. Kitao, H. Nakai, T. Vreven, J. A. Montgomery, Jr., J. E. Peralta, F. Ogliaro, M. Bearpark, J. J. Heyd, E. Brothers, K. N. Kudin, V. N. Staroverov, R.Kobayashi, J. Normand, K. Raghavachari, A. Rendell, J. C. Burant, S. S. Iyengar, J. Tomasi, M. Cossi, N. Rega, J. M. Millam, M. Klene, J. E. Knox, J. B. Cross, V. Bakken, C. Adamo, J. Jaramillo, R. Gomperts, R. E. Stratmann, O. Yazyev, A. J. Austin, R. Cammi, C. Pomelli, J. W. Ochterski, R. L. Martin, K. Morokuma, V. G. Zakrzewski, G. A. Voth, P. Salvador, J. J. Dannenberg, S. Dapprich, A. D. Daniels, Ö. Farkas, J. B. Foresman, J.

V. Ortiz, J. Cioslowski and D. J. Fox, Gaussian 16, Gaussian, Inc., Wallingford CT, 2016.

50. F. Weigend and R. Ahlrichs, *Phys. Chem. Chem. Phys*., 2005, **7**, 3297–3305.
51. F. Weigend, *Phys. Chem. Chem. Phys*., 2006, **8**, 1057–1065.
52. J. L. Pascual-Ahuir, E. Silla and I. Tuñón, *J. Comp. Chem*., 1994, **15**, 1127-1138.
53. L. Li, T. Cai, Z. Wang, Z. Zhou, Y. Geng and T. Sun, *Spectrochim, Acta A Mol. Biomol. Spectrosc*., 2014, **120**, 106–118.
54. E. D. Glendening, A. E. Reed, J. E. Carpenter and F. Weinhold, NBO Version 3.1.
55. A. E. Reed, L. A. Curtiss and F. Weinhold, *Chem. Rev*., 1988, **88**, 899–926.
56. R. Dennington, T. A. Keith and J. M. Millam, GaussView, Version 6, Semichem Inc., Shawnee Mission, KS, 2016.
57. C. F. Macrae, I. Sovago, S. J. Cottrell, P. T. A. Galek, P. McCabe, E. Pidcock, M. Platings, G. P. Shields, J. S. Stevens, M. Towler and P. A. Wood, *J. Appl. Crystallogr.*, 2020, **53**, 226–235.
58. E. R. Johnson, S. Keinan, P. Mori-Sánchez, J. Contreras-García, A. J. Cohn and W. Yang, *J. Am. Chem. Soc*., 2010, **132**, 6498–6506.
59. W. Humphrey, A. Dalke and K. Schulten, *J. Mol. Graph*., 1996, **14**, 33–38.
60. S. K. Wolff, D. J. Grimwood, J. J. McKinnon, M. J. Turner, D. Jayatilaka and M. A. Spackman, *Crystal Explorer (Version 17)*, University of Western Australia, 2012.
61. S. L. Tan, M. M. Jotani and E. R. T. Tiekink, *Acta Crystallogr. Sect. E: Crystallogr. Commun*., 2019, **75**, 308–318.
62. M. A. Spackman and D. Jayatilaka, *CrystEngComm*, 2009, **11**, 19–32.
63. C. F. Mackenzie, P. R. Spackman, D. Jayatilaka and M. A. Spackman, *IUCrJ*, 2017, **4**, 575–587.

64. M. J. Turner, S. Grabowsky, D. Jayatilaka and M. A. Spackman, *J. Phys. Chem. Lett.*, 2014, **5**, 4249–4255.

65. S. P. Thomas, P. R. Spackman, D. Jayatilaka and M. A. Spackman, *J. Chem. Theory Comput*., 2018, **14**, 1614–1623.

66. L. Maschio, B. Civalleri, P. Ugliengo and A. Gavezzotti, *J. Phys. Chem. A*, 2011, **115**, 11179–11186.

67. I. J. Bruno, J. C. Cole, P. R. Edgington, M. Kessler, C. F. Macrae, P. McCabe, J. Pearson and R. Taylor, *Acta Crystallogr., Sect. B: Struct. Sci., Cryst. Eng. Mater*., 2002, **58**, 389–397.

68. K. R. Koch, C. Sacht and S. Bourne, *Inorg. Chim. Acta*, 1995, **232**, 109–115.

69. L. Hennig, K. Ayala-Leon, J. Angulo-Cornejo, R. Richter and L. Beyer, *J. Fluorine Chem*., 2009, **130**, 453–460.

70. S. L.Tan, A. H. S. Azizan, M. M. Jotani and E. R. T. Tiekink, *Acta Crystallogr., Sect. E: Cryst. Commun*., 2019, **75**, 1472–1478.

71. S. L.Tan, M. M. Jotani and E. R. T. Tiekink, *Acta Crystallogr., Sect. E: Cryst. Commun*., 2020, **76**, 155–161.

72. S. A. Bourne, O. Hallale and K. R. Koch, *Cryst. Growth Des*., 2005, **5**, 307–312.

73. P. Matczak, *Computation*, 2016, **4**, article no. 3.

74. L. Salvatella, *Educ. Quimica*, 2017, **28**, 232–237.

75. A. Torrisi, C. Mellot-Draznieks and R. G. Bell, *J. Chem. Phys*., 2009, **130**, article no. 194703.

76. V. Nikolova, D. Cheshmedzhieva, S. Ilieva and B. Galabov, *J. Org. Chem.*, 2019, **84**, 1908–1915.

77. S. L. Tan and E. R. T. Tiekink, *Acta Crystallogr., Sect. E: Cryst. Commun*., 2020, **76**, 102–110.

78. S. L. Tan and E. R. T. Tiekink, *Acta Crystallogr., Sect. E: Cryst. Commun.*, 2019, **75**, 1–7.

79. T. Heddle, in *Calculations in Fundamental Physics: Electricity and Magnetism*, eds R. Robinson and N. Hiller, Elsevier, Amsterdam, Vol. 2, 1971, 167–186.

80. J. Contreras-García, E. R. Johnson, S. Keinan, R. Chaudret, J-P. Piquemal, D. N. Beratan and W. Yang, *J. Chem. Theory Comput.,* 2011, **7**, 625–632.

80. T. Lu and F. Chen, *J. Comput. Chem*., 2011, **33**, 580–592.

82. G. R. Desiraju and J. A. R. P. Sarma, *Proc. Ind. Acad. Sci. (Chem. Sci.)*, 1986, **96**, 599–605.

83. M. R. Edwards, W. Jones, W. D. S. Motherwell and G. P. Shields, *Mol. Cryst. Liq. Cryst*. 2001, **356**, 337–353.

84. D. R. Smyth, B. R. Vincent and E. R. T. Tiekink, *Cryst. Growth Des*., 2001, **1**, 113–117.

85. E. R. T. Tiekink, *Chem. Commun*., 2014, **50**, 11079–11082.

86. J. Haleblian and W. McCrone, *J. Pharm. Sci*., 1969, **58**, 911–929.